

SEISMIC IMAGING OF THE CASCADIA SUBDUCTION ZONE AND JUAN DE
FUCA PLATE SYSTEM MANTLE STRUCTURE: A BOTTOM UP APPROACH TO
SUBDUCTION DYNAMICS

by

MILES BODMER

A DISSERTATION

Presented to the Department of Earth Sciences
and the Graduate School of the University of Oregon
in partial fulfillment of the requirements
for the degree of
Doctor of Philosophy

September 2019

DISSERTATION APPROVAL PAGE

Student: Miles Bodmer

Title: Seismic Imaging of The Cascadia Subduction Zone and Juan De Fuca Plate System
Mantle Structure: A Bottom Up Approach to Subduction Dynamics

This dissertation has been accepted and approved in partial fulfillment of the requirements for the Doctor of Philosophy degree in the Department of Earth Sciences by:

Douglas R. Toomey	Chairperson/Advisor
Emilie H. Hooft	Core Member
Joshua J. Roering	Core Member
Eugene Humphreys	Core Member
Allen Malony	Institutional Representative

and

Janet Woodruff-Borden	Vice Provost and Dean of the Graduate School
-----------------------	--

Original approval signatures are on file with the University of Oregon Graduate School.

Degree awarded September 2019

© 2019 Miles Bodmer
This work is licensed under a Creative
Commons Attribution License



DISSERTATION ABSTRACT

Miles Bodmer

Doctor of Philosophy

Department of Earth Sciences

September 2019

Title: Seismic Imaging of The Cascadia Subduction Zone and Juan De Fuca Plate System
Mantle Structure: A Bottom Up Approach to Subduction Dynamics

I use seismic analysis of teleseismic data to constrain the isotropic and anisotropic mantle structure of the Cascadia subduction zone (CSZ). This work begins by estimating seismic anisotropy parameters beneath the Juan de Fuca (JdF) plate system using teleseismic shear wave splitting. I infer that mantle flow patterns beneath the JdF are heterogeneous and reflect the overlaying tectonic environment. Beneath the JdF plate, shear between the JdF plate and Earth's deep interior entrains the mantle via viscous coupling with some evidence for secondary flow processes. In southern Cascadia, beneath the Gorda deformation zone, there is evidence for mantle reorganization due to plate fragmentation processes. Next, I investigate the isotropic structure of the JdF and CSZ through teleseismic tomographic imaging, utilizing an onshore-offshore P-wave dataset. I image two low-velocity anomalies beneath the subducting slab, interpreted to be localized upwellings and regions of increased buoyancy due to the presence of partial melt. I hypothesize that subslab buoyancy modulates the total shear force along the plate interface, influencing the distribution of megathrust segmentation, as evidenced by spatial correlations to plate locking and tremor density. I extend this model to investigate what influence subslab buoyancy has on forearc topography in Cascadia. We present a conceptual model in which

subslab buoyancy modulates the slab dip angle and/or the degree of plate coupling, which in turn modulates the shear force on the megathrust interface. I suggest this variable shear coupling influences where uplift and forearc topography are most likely to develop and provides dynamic support for forearc topographic highs. Finally, I look at our onshore-offshore tomographic method, using synthetic modeling to show the influence that changes in elevation, crustal thickness, and local geology have on teleseismic delay times. I explore how these perturbations influence inversions and ways to correct for them, identifying artifacts and recommending a preferred methodology.

This dissertation includes previously published and unpublished coauthored material.

CURRICULUM VITAE

NAME OF AUTHOR: Miles Bodmer

GRADUATE AND UNDERGRADUATE SCHOOLS ATTENDED:

University of Oregon, Eugene OR, USA
University of New Mexico, Albuquerque NM, USA

DEGREES AWARDED:

Doctor of Philosophy, Earth Sciences, 2019, University of Oregon
Bachelor of Science, Physics, 2013, University of New Mexico
Bachelor of Science, Applied Mathematics, 2013, University of New Mexico

AREAS OF SPECIAL INTEREST:

Seismic Imaging
Subduction Zone Dynamics
Mantle Deformation and Seismic Anisotropy

PROFESSIONAL EXPERIENCE:

Graduate Teaching Fellow, University of Oregon, 2013-2019
Research Assistant, University of New Mexico, 2010-2013

GRANTS, AWARDS, AND HONORS:

Finalist – 3 Minute Thesis Competition, University of Oregon, 2019
Clarence and Lucille Dunbar Scholarship, University of Oregon, 2018
Johnston Fund Scholarship, University of Oregon, 2015, 2016, 2017
Excellence in Research and Teaching, University of Oregon, 2016
Best Student Poster, GeoPRISMS Theoretical & Experimental Institute, 2015
Outstanding Student Paper Award, AGU Annual Meeting, 2014
1st Place Undergraduate Research Conference, University of New Mexico, 2013
2nd Place Undergraduate Research Conference, University of New Mexico, 2012

PUBLICATIONS:

- Bodmer, M.**, Toomey, D. R., Hooft, E. E., & Schmandt, B. (2018). Buoyant Asthenosphere Beneath Cascadia Influences Megathrust Segmentation. *Geophysical Research Letters*, 45 (14), 6954-6962.
- Lynner, C., & **Bodmer, M.** (2017). Mantle flow along the eastern North American margin inferred from shear wave splitting. *Geology*, 45(10), 867-870.
- Hooft, E.E., Nomikou, P., Toomey, D.R., Lampridou, D., Getz, C., Christopoulou, M.E., O'Hara, D., Arnoux, G.M., **Bodmer, M.**, Gray, M. and Heath, B.A., (2017). Backarc tectonism, volcanism, and mass wasting shape seafloor morphology in the Santorini-Christiana-Amorgos region of the Hellenic Volcanic Arc. *Tectonophysics*, 712, pp.396-414.
- Bodmer, M.**, Toomey, D. R., Hooft, E. E., Nábělek, J., & Braunmiller, J. (2015). Seismic anisotropy beneath the Juan de Fuca plate system: Evidence for heterogeneous mantle flow. *Geology*, 43(12), 1095-1098.
- Akashi-Ronquest, M., Amaudruz, P. A., Batygov, M., Beltran, B., **Bodmer, M.**, Boulay, M. G., ... & Caldwell, T. (2015). Improving photoelectron counting and particle identification in scintillation detectors with Bayesian techniques. *Astroparticle Physics*, 65, 40-54.
- Rielage, K., Akashi-Ronquest, M., **Bodmer, M.**, Bourque, R., Buck, B., Butcher, A., ... & Formaggio, J. A. (2015). Update on the MiniCLEAN dark matter experiment. *Physics Procedia*, 61, 144-152.
- Bodmer, M.**, Phan, N., Gold, M., Loomba, D., Matthews, J. A. J., Rielage, K. (2014). Measurement of Optical Attenuation in Acrylic Light Guides for a Dark Matter Detector, *Journal of Instrumentation*, 9(02), P02002.
- Bodmer, M.**, Giuliani, F., Gold, M., Christou, A., & Batygov, M. (2013). Design of an active magnetic field compensation system for MiniCLEAN. *Nuclear Instruments and Methods in Physics Research Section A: Accelerators, Spectrometers, Detectors and Associated Equipment*, 697, 99-106.

ACKNOWLEDGMENTS

The completion of this dissertation was possible because of the help and support of many people. First and foremost, I would like to thank my advisor Douglas Toomey whose guidance and encouragement helped me to navigate both this dissertation and, in general, my time as a graduate student. I would like to thank both Doug and Emilie Hooft for giving me opportunities to travel and for providing a work environment that was healthy, engaging, and rewarding. I would also like to thank my fellow graduate students whom I have developed personal and professional relationships with. Particularly, Joseph Byrnes, Brandon VanderBeek, Gillean Arnoux, Ben Heath, Daniel O'Hara, and Tyler Newton, who kept me sane with friendship, games, and music. I would like to thank the rest of my committee as well, Josh Roering, Gene Humphreys, and Allen Malony, for all of their guidance and feedback on this work. I am grateful to Amanda Thomas and Josh Roering for allowing me to deploy several seismic instruments on a landslide in Northern California on short notice and a tight budget. I also thank the UO office staff who have helped me immensely to keep everything on track and moving forward. Finally, I would like to thank my family and friends whose love and support kept me going and, of course, none of this would have been possible without my partner Caitlin Hankins who agreed to move across country on this crazy journey 6 years ago and who is still the most important person in my life today. Love you all.

This work was partially supported by the National Science Foundation under grants OCE-1333196 and EAR-1520694 to the University of Oregon.

To my Grandfather, whose love for math, engineering, and science I never appreciated while he was with us, but the impact of which was profound. I know he would have loved to have been here for this moment.

TABLE OF CONTENTS

Chapter	Page
I. INTRODUCTION	1
II. SEISMIC ANISOTROPY BENEATH THE JUAN DE FUCA PLATE SYSTEM: EVIDENCE FOR HETEROGENEOUS MANTLE FLOW	5
1.0 Introduction.....	5
2.0 Data and Methods	6
3.0 Results.....	9
4.0 Discussion.....	12
5.0 Conclusions.....	16
6.0 Bridge.....	16
III. BUOYANT ASTHENOSPHERE BENEATH CASCADIA INFLUENCES MEGATHRUST SEGMENTATION	18
1.0 Introduction.....	18
2.0 Data and Methods	19
2.1 Delay Time Measurements	19
2.2 Tomographic Method.....	21
3.0 Tomographic Results	22
4.0 Interpretation.....	25
4.1 Geodynamic Interpretation of Low-Velocity Anomalies	26
4.2 Estimation of Physical Parameters.....	28
4.2 Sub-slab Buoyancy and its Influence on the Megathrust Interface	29
5.0 Conclusions.....	32

Chapter	Page
6.0 Bridge.....	33
IV. ASTHENOSPHERIC BUOYANCY AND THE ORIGIN OF HIGH-RELIEF TOPOGRAPHY ALONG THE CASCADIA FOREARC.....	
	34
1.0 Introduction.....	34
2.0 Tectonic Setting	36
3.0 Results from Previous Studies	38
3.1 Landscape Evolution of the Forearc	38
3.2 Isostasy of the Subducting Plate and Overriding Crust	42
3.3 Subslab Buoyancy.....	44
3.4 Along-Strike Variations of the Slab Interface	45
3.5 Mechanics of the Forearc.....	47
4.0 Discussion.....	50
4.1 Influence of Subslab Buoyancy on the Megathrust Interface.....	52
4.2 Forearc Uplift.....	53
4.3 Support of High Forearc Topography.....	54
5.0 Conclusion	56
6.0 Bridge.....	57
V. ONSHORE-OFFSHORE BODY WAVE TOMOGRAPHY OF THE CASCADIA SUBDUCTION ZONE: IDENTIFYING CHALLENGES AND SOLUTIONS FOR SHORE CROSSING DATA.....	
	58
1.0 Introduction.....	58

Chapter	Page
2.0 Tectonic Setting	61
3.0 Body Wave Delay Time Data	64
3.1 Data and Methods	64
3.2. Observed Delay Times and Trends	68
4.0 Tomographic Method.....	69
5.0 Synthetic Studies of Amphibious Data.....	71
5.1 Forward Modeling of Shore-Crossing Refraction Profiles.....	72
5.2 Inverse Modeling of Synthetic Delay Times	73
5.2.1 Synthetic Delay Times.....	74
5.2.2 Tomographic Inversions	76
6.0 Cascadia Subduction Zone Tomography	79
6.1 Near Surface Structural Model	79
6.2 Tomographic Inversions	82
7.0 Discussion.....	84
7.1 Importance of a priori Starting Models.....	84
7.2 Improved Resolution Beneath the Forearc and Identification of Artifacts	85
7.3 Limitations	86
7.4 Future Directions	87
VI. CONCLUSIONS	88

Chapter	Page
APPENDICES	91
A. CHAPTER II SUPPORTING INFORMATION	91
B. CHAPTER III SUPPORTING INFORMATION	104
C. CHAPTER IV SUPPORTING INFORMATION	115
D. CHAPTER V SUPPORTING INFORMATION	121
REFERENCES CITED.....	124

LIST OF FIGURES

Figure	Page
CHAPTER II	
1. Bathymetric and topographic map showing location of seismometers	7
2. SKS splitting results overlaying magnetic anomalies.....	10
3. Plots of the fast polarization direction	11
4. Schematic of upper mantle anisotropy.....	15
CHAPTER III	
1. Tectonic features of the Cascadia subduction zone	20
2. Map view slice at 100 km depth	23
3. Average P-wave velocity anomalies between 100 and 250 km depth.....	25
4. Conceptual vertical cross-section representing the northern and southern segments of Cascadia.....	32
CHAPTER IV	
1. Topographic map of the Cascadia subduction zone	35
2. Along-strike variations in the landscape evolution of the Cascadia forearc.....	40
3. Plate age variations beneath the forearc swath	43
4. Along-strike variations in the subslab mantle, slab geometry, and along the megathrust interface.....	46
5. Schematic model.....	48
6. Conceptual model for the Cascadia subduction zone	51

Figure	Page
11. Predicted topography	55
 CHAPTER V	
1. Map of the Cascadia subduction zone	61
2. Example teleseismic waveforms for P- and S-waves	66
3. Event distribution for P and S events in the dataset.....	67
4. Average station delay times	68
5. Synthetic delays predicted from 2D profiles	72
6. Station averaged delay times through the generic model	75
7. Synthetic tests of P and S wave data.....	76
8. Predicted average station delays through the Cascadia subduction zone starting model.....	81
9. Tomographic inversions of the P-wave data.....	82

CHAPTER I

INTRODUCTION

Subduction zone systems are one of the largest global hazards, responsible for large megathrust earthquakes ($M9+$), tsunami generation, and explosive volcanism. Subduction zone dynamics are not homogenous, with along-strike variations in seismogenesis, geodetic motions, and magma production. The underlying mechanisms giving rise to this segmentation, however, are still poorly understood. Many studies focus on properties of the overriding crust, incoming oceanic crust, or properties along the plate interface to explain along-strike segmentation. Here, however, I focus on the incoming oceanic mantle, trying to understand what role it plays in subduction phenomenon. Recent dense deployments of seismic instruments both onshore and offshore allow me to address several open questions regarding subduction zone dynamics at the Cascadia margin, such as: What is the nature of mantle flow beneath the incoming plate and what implications does this have for material being brought into or taken out of the subduction zone? Does mantle heterogeneity have any relationship to the segmentation of megathrust behavior in Cascadia? Does mantle structure relate to forearc processes such as uplift and the development of differential topography? This dissertation addresses these questions through seismic imaging of the isotropic and anisotropic structure of the Cascadia subduction zone, synthesizing seismic models with previous multi-disciplinary results to gain a more complete understanding of subduction zone dynamics.

In Chapter II, I use teleseismic shear wave data to investigate patterns of mantle flow and deformation beneath the Juan de Fuca (JdF) plate system. To accomplish this, I use SKS shear wave splitting to measure anisotropic parameters and infer mantle deformation patterns. I investigate what role the overlying plate motions have in controlling asthenospheric flow, as well as processes specific to subduction zone edges such as slab rollback induced toroidal flow and offshore plate fragmentation. Shear wave splitting results suggest that to first order, beneath the JdF plate, absolute plate motions drive mantle flow via viscous drag, entraining mantle material into the subduction zone. However, a systematic clockwise rotation in anisotropic fast-axes suggests some secondary process is also influential in the region. In southern Cascadia, beneath the Gorda deformation zone, we observe splitting orientations inconsistent with those beneath the JdF plate. We attribute this to mantle reorganization in the Pacific-JdF relative plate motion direction associated with plate fragmentation and do not find evidence for large scale toroidal flow.

In Chapter III, I use onshore-offshore teleseismic delay time data to tomographically image the Cascadian subduction zone. Using relative P-wave arrivals, I investigate how mantle structure beneath the subducting slab impacts the segmentation of megathrust behavior observed in Cascadia. Tomographic results show along-strike segmentation in the oceanic asthenosphere beneath the subducting plate with pronounced low-velocity anomalies below regions of increased plate locking and greater occurrence of episodic tremor and slip. Anomalous asthenospheric velocities are attributed to independent mantle upwellings associated with regional hotspot-derived material in northern Cascadia and plate fragmentation processes at a diffuse plate-boundary, the

Gorda deformation zone, in southern Cascadia. We interpret these anomalies as regions of increased buoyancy due to the presence of partial melt (decompression melting) and possibly increased temperatures. Based on these relations, I hypothesize that subslab buoyancy modulates the plate coupling force at the thrust interface, thereby contributing to the localization of subduction zone segmentation.

I build upon the P-wave tomography results in Chapter IV, where I investigate the relationship between subslab low-velocity anomalies and the segmentation of forearc topography in the Cascadia subduction zone. In this chapter, I synthesize results from seismic imaging, short and long-term uplift rates, erosion rates, topographic analysis, and characteristics of the megathrust interface, with a mechanical model to infer that buoyancy in the subslab asthenosphere influences the development and longevity of Cascadia's forearc topography. The Cascadia margin can be divided into three segments, with the northern and southern segments characterized by rapid short- and long-term uplift rates, rapid erosion rates, high coseismic subsidence, shallower slab dip angles, and increased plate locking compared to the central segment. Modeling suggests that buoyant regions subslab can locally increase the total shear force at the megathrust by either shallowing the slab dip or increasing plate coupling along the megathrust. I propose that: 1) sub-slab buoyancy influences topographic development by modulating along-strike patterns of interseismic strain within the over-riding plate, 2) long-term surface topographic development occurs due to unrecovered strain over thousands of seismic cycles, and 3) variations in Cascadia's forearc topography are laterally supported by changes in the total shear force at the megathrust interface.

Finally, in Chapter V, I extend the results of Chapter III by including new data and exploring the methodology behind our onshore-offshore approach. I conduct several synthetic tests of both P- and S-waves to better understand the impact of elevation, crustal thickness, and local geology on teleseismic delay times and the resulting tomographic inversions. Synthetic forward modeling suggests that upwards of 1s of delay is introduced by elevation and crustal thickness variation (in roughly equal proportions) in shore-crossing P-wave data. Tomographic inversions of synthetic data suggest that ray-tracing through detailed starting models of near-surface structure (constrained by independent seismic studies) reduces tomographic artifacts and improves resolution of mantle targets. Using station static terms, on the other hand introduces artifacts and reduces amplitudes of mantle structures.

Chapter II of this dissertation was coauthored by Douglas R. Toomey, Emilie H. Hooft, John Nábělek, and Jochen Braunmiller and was published in *Geology* in December 2015. Chapter III of this dissertation was coauthored by Douglas R. Toomey, Emilie H. Hooft, and Brandon Schmandt and was published in *Geophysical Research Letters* in July 2018. Chapter IV of this dissertation was coauthored by Douglas R. Toomey, Josh J. Roering, and Leif Karlstrom and is in revision for *Earth and Planetary Science Letters*.

CHAPTER II

SEISMIC ANISOTROPY BENEATH THE JUAN DE FUCA PLATE SYSTEM: EVIDENCE FOR HETEROGENEOUS MANTLE FLOW

From Bodmer, M., Toomey, D. R., Hooft, E. E., Nábělek, J., and Braunmiller, J. (2015). Seismic anisotropy beneath the Juan de Fuca plate system: Evidence for heterogeneous mantle flow. *Geology* 43(12), 1095–1098.

1.0 Introduction

Mantle convection and the movement of tectonic plates drive flow in Earth's viscous upper mantle. The nature of mantle flow and its relation to plate boundary evolution are relevant to plate dynamics and thus remain topics of vigorous inquiry. Because mantle strain induces lattice preferred orientation of seismically anisotropic minerals, particularly olivine, seismic methods can be used to constrain patterns of mantle flow (Silver and Chan, 1991).

The Juan de Fuca (JdF) plate system is an excellent target for investigating the forces that drive oceanic mantle flow. In a compact region we find all three types of discrete plate boundaries, lithospheric plates that are both intact (JdF) and internally deforming (southern Gorda plate), and an evolving subduction zone system susceptible to edge effects, slab rollback, and plate fragmentation (Fig. 1). The Cascadia Initiative, a multiyear, onshore-offshore experiment (Toomey et al., 2014), and a complementary Blanco transform array (Ghorbani et al., 2015) specifically target these regions and for the first time provide dense coverage of an entire oceanic plate and its boundaries.

Here we use ocean bottom seismometer (OBS) data and the well-established shear wave splitting method to investigate mantle flow beneath the JdF plate system. Owing to the extensive coverage of our OBS array, and the spatial coherence of interstation shear wave splitting observations, we are able to detect significant heterogeneity in the oceanic mantle flow field. Our results have implications for the forces that drive asthenospheric flow and for the evolution of the complex plate interactions that define southern Cascadia.

2.0 Data and Methods

We analyze seismic data from five onshore Cascadia Initiative instruments, 117 OBS sites from years 1, 2, and 3 of the Cascadia Initiative, and 30 OBSs from the Blanco array (Fig. 1; Fig. DR1 in the GSA Data Repository¹). The orientations of the horizontal components of the Cascadia Initiative OBSs were determined by Sumy et al. (2015) with a median uncertainty in channel orientation of $\pm 9^\circ$ at the 1 σ confidence level. We analyze the SKS phase of teleseismic events, $M_w \geq 6$, at distances of 90° – 130° . All onshore instruments and 111 of the 147 OBSs recorded at least one usable event (Table DR1 in the Data Repository). The OBSs recorded an average of four usable events, and only 14 sites recorded just a single usable event (Table DR2). Back-azimuthal event coverage is limited and has a westward bias for the OBS data due to the short deployment time (Fig. DR2).

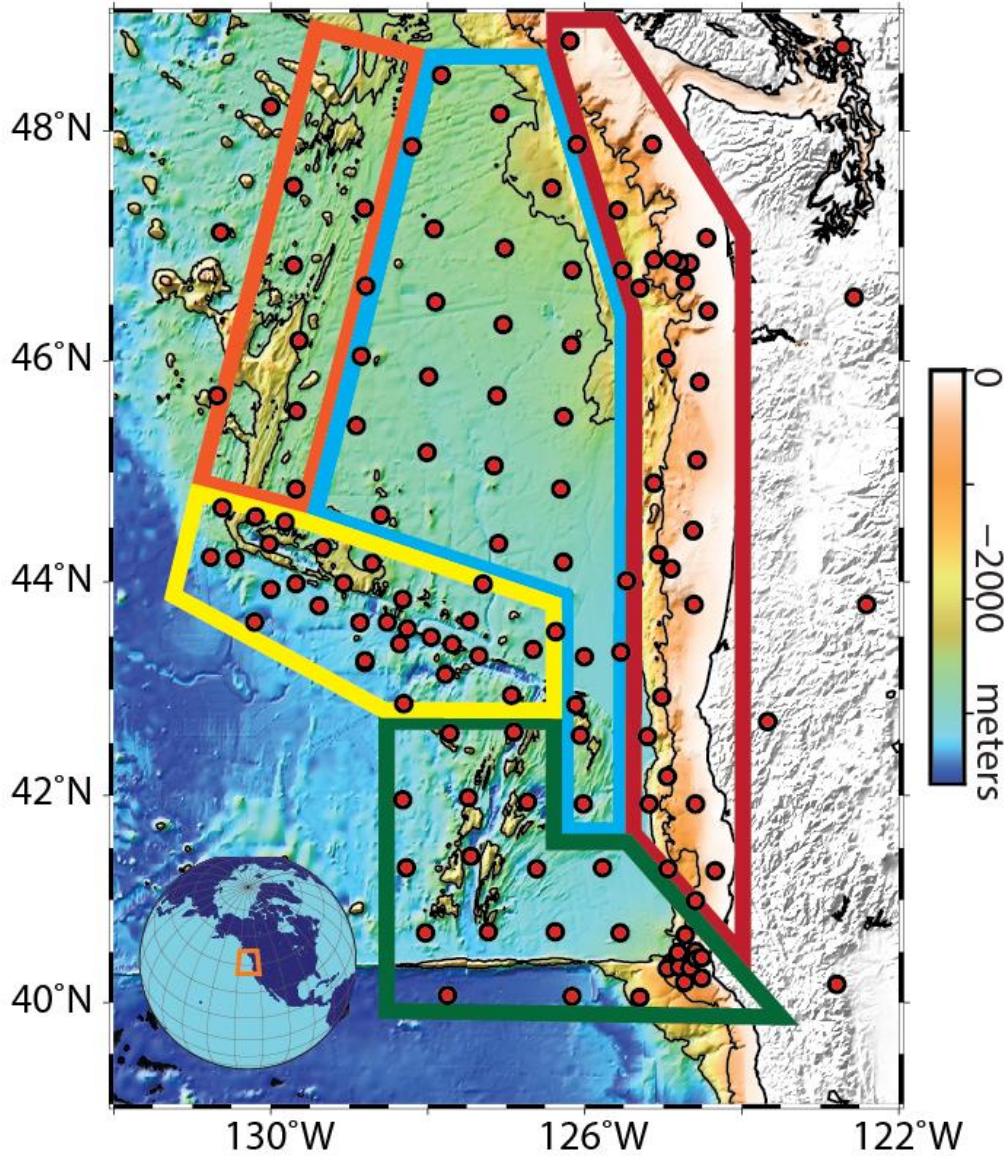


Figure 1: Bathymetric and topographic map showing location of seismometers (red circles) and geographic regions defined by tectonic setting and observed splitting patterns: (blue) Juan de Fuca plate interior, (red) Cascadia subduction zone, (orange) Juan de Fuca ridge, (yellow) Blanco transform, (green) Mendocino triple junction and southern Gorda region.

We implemented a workflow that uses strict quality control to account for high environmental noise levels typical of OBS data. Our SKS splitting analysis was conducted using the Splitlab software package (Wüstefeld et al., 2008), which performs three common splitting methods: rotation correlation (RC) (Bowman and Ando, 1987), Silver and Chan (SC), and eigenvalue (EV) (Silver and Chan, 1991). Each method

estimates the polarization direction of the fast shear wave Φ and the delay time δt between the fast and slow shear waves (Fig. DR3). Initial measurements are filtered with a third-order, zero-phase Butterworth bandpass filter (0.03–0.1 Hz). This isolates the SKS arrival within a relatively low noise band between the microseism peak (0.1–2 Hz) and the high-frequency limit of infragravity waves (<0.04 Hz). Measurements are repeated for several filter limits adjusted between 0.02 and 0.15 Hz and covering at least a full octave. Multiple measurements allow for a qualitative assessment of stability from which a final event measurement is chosen; reported measurements often include higher frequencies, even those that may obscure the previously identified SKS waveform, improving accuracy (Restivo and Helffrich, 1999). We report measurements using only the SC method due to the poor performance of the RC method on low signal-to-noise data (Vecsey et al., 2008). All three methods are used for quality control, verifying that results from the SC and EV methods are consistent and that the RC method is either consistent or yields results indicative of high noise contamination (Vecsey et al., 2008). Measurements with delay times >3.5 s or <0.5 s are discarded. Possible null measurements are not reported because they are indistinguishable from measurements with high noise levels on the transverse channel.

Maps of the transverse energy are generated by grid searching in the dt-F parameter space. A single set of splitting parameters is estimated for each station by stacking the normalized energy maps (Wolfe and Silver, 1998) and a statistical F-test is applied to obtain the 95% confidence intervals (Fig. DR3) (Silver and Chan, 1991), which are converted to 1s errors. Typical uncertainties in F and dt are 8° and 0.3 s (Table DR1), respectively, although in shallow water they tend to be larger. To verify that we

can recover known splitting parameters, we analyzed good quality data from onshore Cascadia Initiative stations and successfully reproduced the trench perpendicular pattern found by previous studies (e.g., Eakin et al., 2010).

3.0 Results

Our SKS splitting results (Figs. 2 and 3) reveal spatially coherent patterns in fast polarization directions that are correlated with five tectonic environments (Fig. 1): (1) the JdF plate interior and northern Gorda plate; (2) the southern, internally deforming Gorda plate and Mendocino Triple Junction (MTJ); (3) the Juan de Fuca Ridge; (4) the Cascadia subduction zone (CSZ); and (5) the Blanco transform fault.

The fast polarization directions within the JdF plate interior and the northern Gorda plate show an average trend of N63°E that extends from 50 km east of the ridge to the subduction zone (Figs. 2 and 3A). Delay times are 1 s, on average, and do not appear to vary with plate age (Fig. DR4). Orientations correlate poorly with the JdF plate–Pacific plate spreading direction (N107°E). To estimate the absolute plate motion (APM) of the JdF plate, we use the APM of the Pacific plate, which is well known, and the Pacific-JdF relative plate motion (RPM) calculated from the MORVEL model (DeMets et al., 2010). In this reference frame, fast polarization directions broadly correlate with APM (N30°E to N50°E, depending on location; see Fig. 3A). We note, however, that the observed fast polarization directions are systematically rotated clockwise from the APM direction (Fig. 3A).

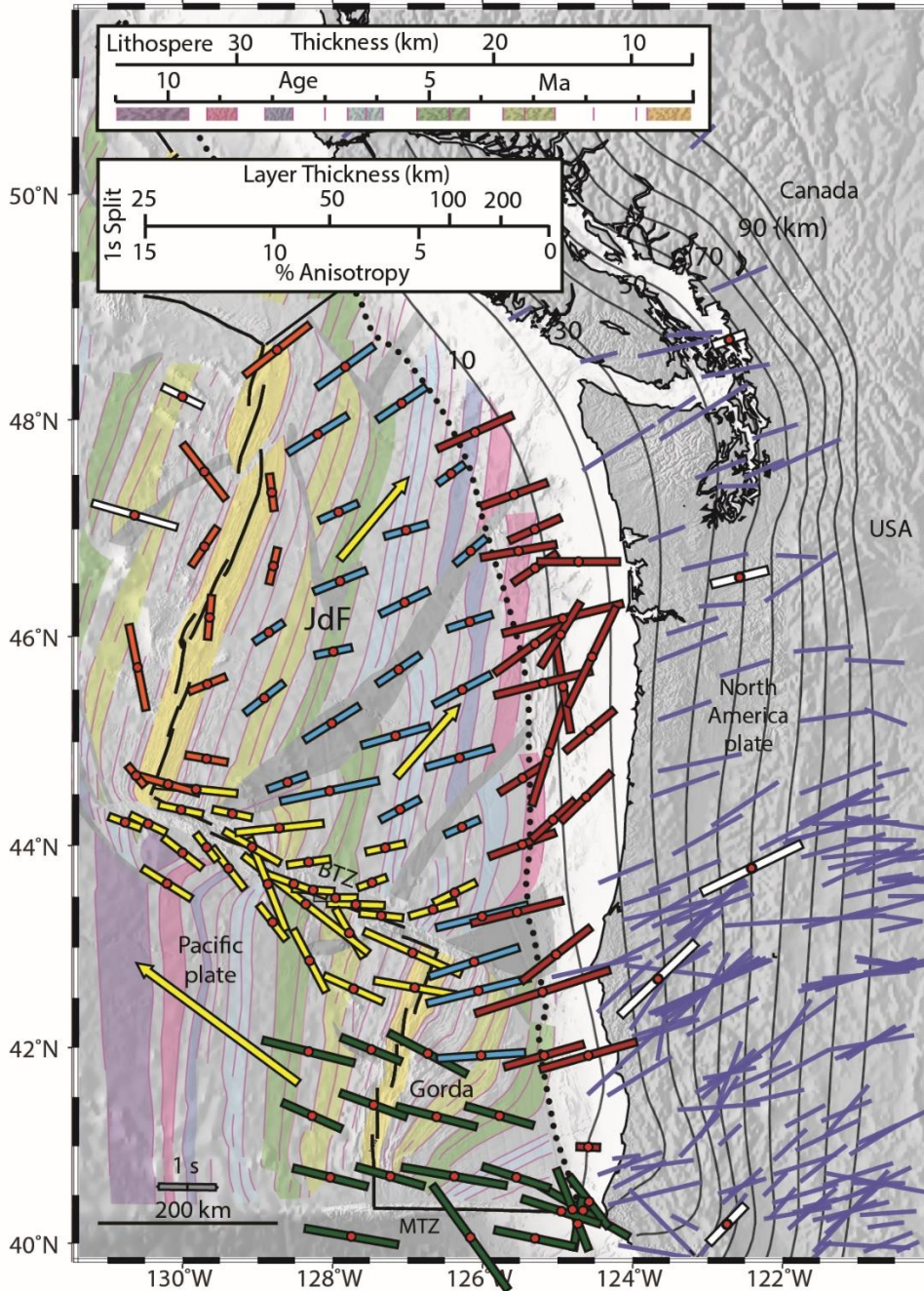


Figure 2: SKS splitting results overlaying magnetic anomalies (light colored bands) and propagator wakes (gray bands) (from Nedimović et al., 2009). Thick bars indicate our measurements color coded by zone (see Fig. 1). Orientation of a bar shows the fast polarization direction and its length is scaled by the delay time. Yellow arrows are the absolute plate motions (modified from MORVEL, DeMets et al., 2010). Blue bars are SKS splitting measurements from land studies (Currie et al., 2004; Eakin et al., 2010; Bonnin et al., 2010). Thin black lines are depth to slab contoured at 10 km intervals (McCrory et al., 2012). (Upper left) top scale shows the seafloor age and corresponding lithospheric thickness for a half-space cooling model and the bottom scale shows layer thicknesses and percent anisotropy for a 1 s delay time.

In the southern Gorda plate, we observe a region of coherent fast polarization measurements oriented N109°E (Figs. 2 and 3B). This trend extends beyond the Gorda plate into the Pacific plate, and is not disrupted by the Gorda spreading center or the Mendocino transform fault. The northern boundary of this region correlates well with the onset of intense lithospheric deformation of the southern Gorda plate (Chaytor et al., 2004). Measurements within 25 km of the MTJ show large variance but become consistent at greater distances (Fig. 3B). In contrast to the JdF plate interior, the observed fast polarization directions are inconsistent with the JdF APM. Although similar to the APM of the Pacific plate (N122°E) and the relative spreading direction of the southern Gorda Ridge (N98°E), fast polarization directions agree best with the relative motion between the nondeforming JdF and Pacific plates (N107°E). Delay times are 1.4 s on average with low variability and do not appear to have any spatial dependence.

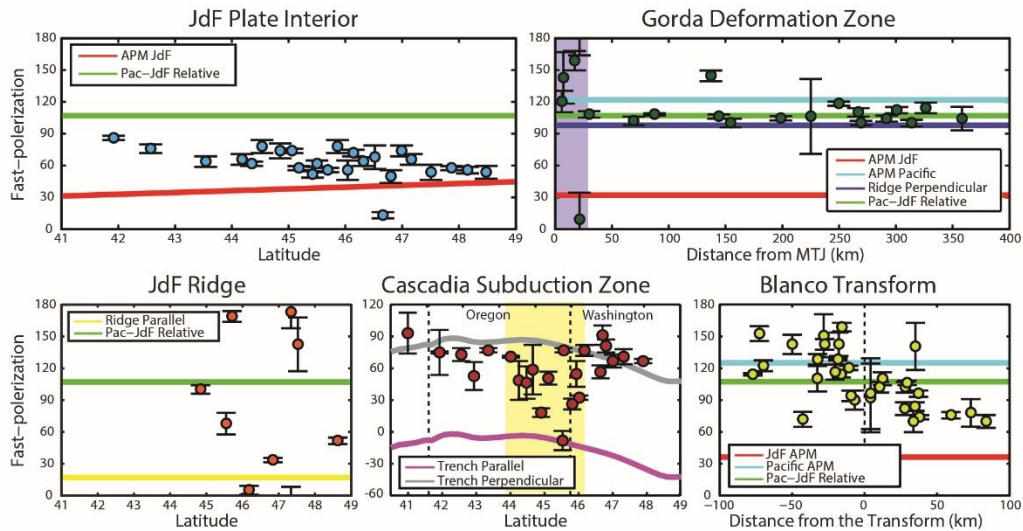


Figure 3: Plots of the fast polarization direction (degrees clockwise from N) as a function of distance or latitude for each of the zones shown in Figure 1; measurements (circles) are color coded by zone (see Fig. 1). Colored lines show orientations predicted by various scenarios. Purple band (b) represents the region within 25 km of the MTJ and the yellow band (d) is the region of anomalous observations in central Cascadia.

Measurements within 50 km of the Juan de Fuca Ridge are sparse and suggest a variable pattern (Figs. 2 and 3C). Near the intersection of the Juan de Fuca Ridge and Blanco transform fast polarization directions correlate with JdF-Pacific RPM. Throughout most of the central ridge segments there appears to be a broad ridge-parallel trend, most notably near the Axial Seamount, that diminishes northward. Average delay times are 1 s.

Near the CSZ, most fast polarization directions closely resemble those within the JdF plate interior and the western United States (Figs. 2 and 3D) and delay times are 1.4 s on average. The relative convergence of the JdF plate and North America is at $N56^{\circ}E$ and the trench orientation changes from $\sim N2^{\circ}W$ to $N48^{\circ}W$, from south to north. Relative to the trench trend, measurements in the southern and northern CSZ are roughly trench perpendicular but rotate counterclockwise toward trench parallel between $44^{\circ}N$ and $46^{\circ}N$. The region of trench-parallel orientations coincides with several geologic features that make central Cascadia anomalous, e.g., where subduction changes orientation and flattens (McCroory et al., 2012).

In the Blanco transform region fast polarization directions rapidly change from northwest-southeast to northeast-southwest when crossing the transform from the Pacific to JdF plates and correlate well with respective APMs (Figs. 2 and 3E). Within 25 km of the transform, orientations parallel the relative motion of the JdF and Pacific plates. Delay times are 1 s on average.

4.0 Discussion

We use our splitting results to infer regional-scale patterns of mantle flow by assuming that the observed fast polarization directions are subparallel to the direction of

maximum shear (e.g., Silver and Chan, 1991). Our data are insufficient to explicitly test for multiple anisotropic layers (see Figs. DR5 and DR6); however, we consider the possibility of depth-dependent anisotropy in our interpretations. Sites with only one or two measurements are less certain, but the observations are supported by their consistency with neighboring sites. Given 4% mantle anisotropy, a splitting time of ~ 1 s would require an ~ 100 -km-thick anisotropic layer. Because our split times are typically 1 s or more, and predicted lithospheric thickness in this region is 5–30 km (Fig. 2), we infer that the bulk of observed anisotropy originates in the asthenosphere.

We attribute anisotropy beneath the JdF and northern Gorda plates to an entrained layer of asthenosphere influenced by APM and altered by a secondary process. Subslab entrainment has been interpreted for several Cascadia data sets (Currie et al., 2004; Eakin et al., 2010; Bonnin et al., 2010), young subduction zones (Lynner and Long, 2014), and geodynamic models (Faccenda and Capitanio, 2012). Correlation with APM in the JdF plate interior and the CSZ (Figs. 3A and 3D) is consistent with the plate dragging asthenosphere into the subduction zone via viscous coupling. The systematic clockwise rotation of fast polarization directions from APM suggests that some secondary process is important. One possibility is that a shallow layer of anisotropy aligned with RPM due to corner flow at the ridge results in an apparent fast axis altered by multiple layering. However, this requires an ~ 0.5 s delay time contribution, implying either a very thick (50 km at 4% anisotropy) or highly anisotropic (12% at 20 km thickness) layer (Fig. DR6). While anisotropy related to plate spreading is very likely, it is unclear whether it exists in the necessary magnitudes. Furthermore, most observations near the ridge are inconsistent with the RPM direction. An alternative interpretation is that asthenospheric flow is also

driven by internal convection unrelated to APM. Indeed, seismic studies of the Endeavor segment of the Juan de Fuca Ridge show that subridge mantle divergence is skewed clockwise with respect to the plate spreading direction and related to a recent change in JdF-Pacific plate motion (VanderBeek et al., 2014).

At the Blanco transform, a discrete plate boundary between the JdF and Pacific plates, we infer a narrow shear zone with deformation aligned with RPM. Rapid changes in fast polarization orientations across the transform indicate highly localized deformation within a 50-km-wide zone centered on the transform. The distribution of strain with depth is unknown; however, relatively low viscosities in the asthenosphere beneath the transform and/or very shallow anisotropic structure may be necessary to produce the rapid changes in orientation observed, particularly when considering the overlap of SKS Fresnel zones.

Beneath the southern Gorda plate region, a diffuse plate boundary, we attribute anisotropy to a broad shear zone accommodating Pacific-JdF RPM (Figs. 3B and 4). In response to northward movement of the Pacific plate, the southern Gorda lithosphere is undergoing internal deformation, which is evident in bathymetry (Fig. 1), magnetic anomalies (Fig. 2), anomalous orientations of the Gorda Ridge and Mendocino transform, bookshelf faulting (Chaytor et al., 2004), and geodynamic models of regional stress (Wang et al., 1997). Correlation of our observations with both the region of crustal deformation and the Pacific-JdF RPM suggests a common causal factor for both lithospheric and asthenospheric deformation. In our proposed model (Fig. 4) the southern Gorda region is a weak zone separating two rigid plates and thus accommodates the relative motion between them with both asthenosphere and lithosphere undergoing

deformation and upper mantle strain aligned with RPM. Our results, in conjunction with those near the Explorer plate (Mosher et al., 2014), suggest that reorientation of upper mantle flow plays a critical role in plate fragmentation, with RPM alignment beneath the Gorda plate representing an intermediate state before full detachment.

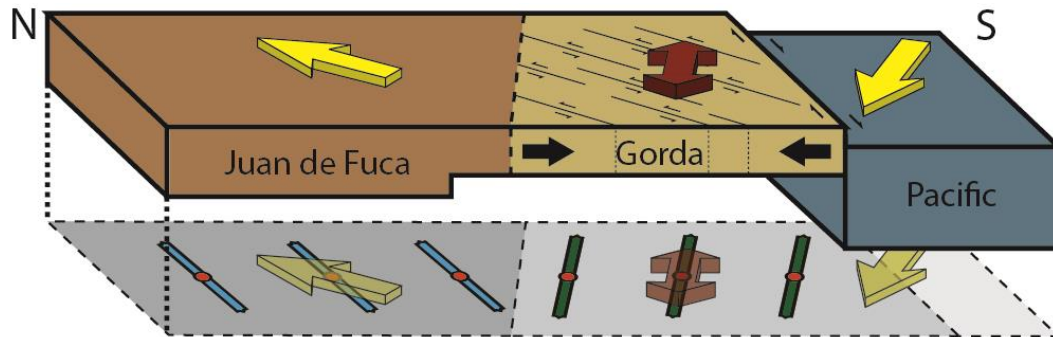


Figure 4: Schematic of upper mantle anisotropy beneath the JdF plate interior and the southern Gorda region. Top layer: Yellow arrows indicate absolute plate motions. The red double arrow represents the relative motion of Pacific-JdF. Black arrows represent N-S compression of southern Gorda. Small black arrows depict the Mendocino transform fault and strike-slip faulting within the Gorda plate. Bottom layer: Typical splitting orientations color coded by zone (see Fig. 1); fast polarization directions beneath the JdF are rotated CW from APM and within the Gorda region parallel Pacific-JdF relative motion.

Our results are inconsistent with the rollback-induced toroidal flow model commonly invoked for onshore anisotropy near the MTJ (e.g., Zandt and Humphreys, 2008). Geodynamic models suggest that beneath a downgoing plate toroidal flow results in strong trench-parallel deformation (Faccenda and Capitanio, 2012), which is inconsistent with our results by $\sim 65^\circ$ (Figs. 2 and 3B). Furthermore, observed orientations and delay times do not vary with distance from the slab edge and abruptly change orientation at the northern limits of the Gorda deformation zone. We conclude that there is no large-scale toroidal flow due to slab rollback or that the deformation is weak resulting in minimal influence on measurements. Diversion of ambient flow around the southern slab edge is another possible source of deformation (Eakin et al., 2010).

However, due to the lack of variation with distance from the slab edge, large delay times, and correlations with Gorda plate deformation we assert that its contribution to the anisotropic structure is, if present, secondary.

5.0 Conclusions

Seismic anisotropy of the upper mantle beneath the JdF plate system is remarkably heterogeneous, indicating that a variety of forces drive flow in the oceanic asthenosphere. Beneath rigid plates, APM is a significant driver of flow that entrains asthenosphere and drags it into subduction zones. There is also evidence of a secondary source of anisotropy possibly related to non-APM convective processes. Near plate boundaries anisotropy records relative plate motion (e.g., Blanco), but in some cases is complex (e.g., Juan de Fuca Ridge and Mendocino transform). Plate fragmentation occurring within the diffuse plate boundary in the southern Gorda plate region is accompanied by reorganization of upper mantle flow.

6.0 Bridge

Chapter II presented evidence for heterogeneous mantle flow beneath the Juan de Fuca plate and Cascadia subduction zone. Broadly beneath the Juan de Fuca plate, asthenosphere is viscously dragged in the absolute plate motion direction where it is eventually entrained into the subduction zone, though there is evidence for a secondary flow process. In southern Cascadia plate fragmentation processes cause a reorganization of mantle flow, driven by the NW motion of the Pacific plate and its interaction with the Gorda deformation zone. It remains unclear though how, if at all, heterogeneity in mantle flow patterns influence the physical state of the mantle beneath the subduction zone. In Chapter III I use teleseismic tomography to investigate the physical state of the mantle,

interpreting velocity structure with respect to the mantle flow dynamics discussed in Chapter II. With this more integrated view of the subduction zone structure and dynamics I explore how the subslab mantle may be influencing megathrust behavior and contributing to segmentation of the subduction zone.

CHAPTER III

BUOYANT ASTHENOSPHERE BENEATH CASCADIA INFLUENCES

MEGATHRUST SEGMENTATION

From Bodmer, M., Toomey, D. R., Hooft, E. E., Schmandt, B. (2018). Buoyant asthenosphere beneath Cascadia influences megathrust segmentation. *Geophysical Research Letters* 45(14), 6954–6962.

1.0 Introduction

Segmentation of large earthquakes at subduction zones has been observed globally for several decades (Ando, 1975; Kelleher, 1972; Thatcher, 1990), however, the mechanisms governing the spatial extent of segments are unknown. Seismic and geodetic evidence for segmentation of megathrust interfaces include variations in inter-seismic and co-seismic surface motions (Ando, 1975; Schmalzle et al., 2014), the along-strike nucleation and extent of large megathrust ruptures (Goldfinger et al., 2012), and the density of episodic tremor and slip (ETS) (Brudzinski & Allen, 2007; Wells et al., 2017). These observations suggest along-strike heterogeneity in the mechanics of the megathrust interface that influence coupling at convergent margins. Current hypotheses for the cause of segmentation include the composition of large overlying crustal blocks (Brudzinski & Allen, 2007), the presence and mobility of fluids delivered to the thrust interface (Audet et al., 2009), the abundance of offshore sediments (Ruff, 1989), and lateral differences in the crustal and topmost mantle structure of the incoming plate (Cloos, 1992).

The Cascadia subduction zone (CSZ), where the oceanic Juan de Fuca (JdF) plate subducts beneath North America (Figure 1a), is an ideal site to study megathrust

segmentation due to the abundance of high-quality seismic (Toomey et al., 2014) and geodetic data, well-defined segments (Brudzinski & Allen, 2007; Goldfinger et al., 2012), and a wealth of previous research. The CSZ includes two diffuse plate boundary regions — the southern Gorda deformation zone and the northern Explorer microplate — where plate fragmentation processes have significantly altered the incoming plate (Chaytor et al., 2004; Riddihough, 1984). The age of the JdF plate entering the subduction zone is young (~10 My) and varies little beneath the forearc south of 49°N (Wilson, 2002). Multiple studies suggest along-strike segmentation of the megathrust, identifying three primary segments (northern, central, and southern; Figure 1a) (Brudzinski & Allen, 2007; Burgette et al., 2009; Schmalzle et al., 2014; Wells et al., 2017). The northern and southern segments, relative to the central segment, are typified by larger slip deficits (Schmalzle et al., 2014) and a greater density of ETS (Brudzinski & Allen, 2007). Here we use the results of teleseismic P-wave tomography and estimates of physical properties to infer that mantle buoyancy beneath the slab influences megathrust segmentation by modulating the plate coupling force at the thrust interface.

2.0 Data and Methods

2.1 Delay Time Measurements

Our study combines new teleseismic P-wave delay time measurements from recent onshore-offshore experiments with previously reported teleseismic delay time data from onshore studies of the western US (Schmandt & Humphreys, 2010a; Schmandt & Lin, 2014). We measure delay times via cross-correlation (VanDecar & Crosson, 1990) of seismic waveform data from the 4-year-long Cascadia Initiative (CI) community experiment (Toomey et al., 2014), and separate year-long studies of the Blanco transform

and Gorda region (Green circles Figure 1b). The CI amphibious array — comprised of 60 ocean bottom seismometers (OBS) deployed in ~10-month-long intervals and 27 onshore sites recording continuously — encompassed the entirety of the JdF plate system, including the JdF Ridge, Gorda Ridge, Blanco transform, Gorda deformation zone, and the CSZ (Figure 1). The Blanco and Gorda experiments occurred during the CI and provide an additional 30 and 24 OBSs, respectively. Reoccupation of offshore and onshore sites, as well as several permanent stations, tie the data sets together.

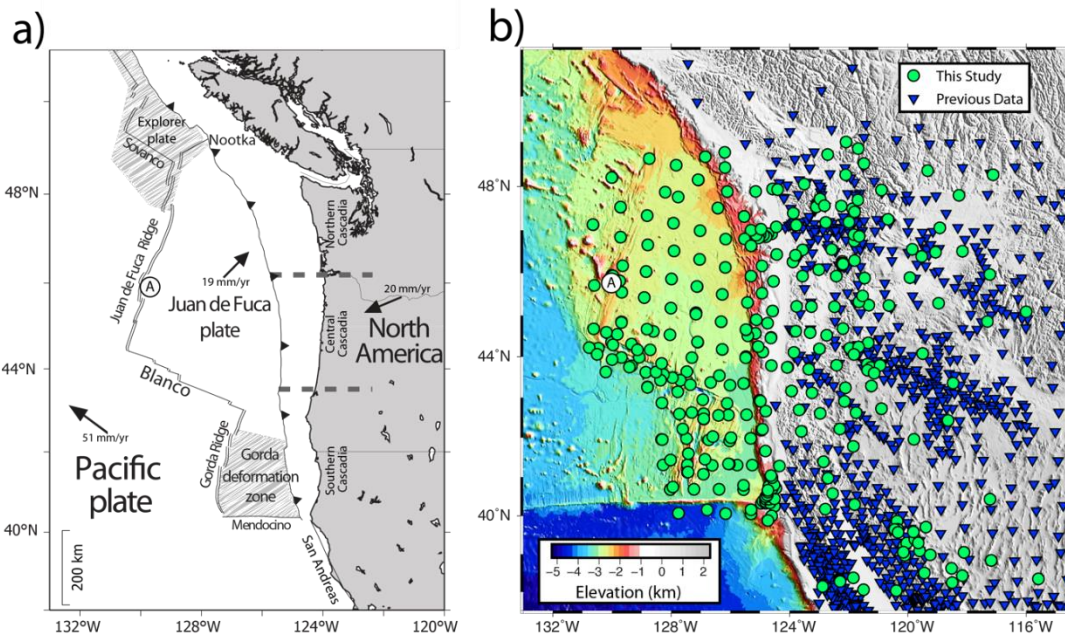


Figure 1: a, Tectonic features of the Cascadia subduction zone and the Juan de Fuca plate system [modified from Byrnes et al. (2017)]. Arrows represent absolute plate motions of the Pacific, Juan de Fuca, and North American plates (DeMets et al., 2010). Shaded regions represent the Gorda and Explorer diffuse plate boundaries. White circle (A) represents the location of Axial Seamount the current expression of the Cobb hotspot. Dashed lines show the boundaries of megathrust segments discussed in the text. *b*, Map of regional elevation and distribution of seismic stations. Green circles are Cascadia Initiative and coincidentally operating stations newly processed for this study. Blue triangles denote stations and data from previous study (Schmandt & Humphreys, 2010a).

Altogether, our analysis uses 108,922 teleseismic delay times (P, pP, and PKP phases) from 2,320 events (Figure S3) recorded at 1,115 stations; 36,277 of the arrivals are newly processed for this study (Figure S2). The addition of shore-crossing CI data improves the resolution of the CSZ's mantle structure due to the increase in crossing rays, particularly beneath the forearc region.

2.2 Tomographic Method

We use a tomographic method that is well-suited to amphibious data since it treats the forward problem accurately and explicitly includes prior states of information, including uncertainties (Jackson, 1979; Tarantola & Valette, 1982). Aspects of our workflow that distinguish it from algorithms commonly used for teleseismic delay-time tomography are: (1) the ability to define complex, three-dimensional starting models that include elevation, (2) iterative, three-dimensional seismic ray tracing, (3) approximate finite frequency sensitivity kernels, and (4) a flexible scheme for regularizing inversions. Details of our methods are presented elsewhere (Bezada et al., 2013; Byrnes et al., 2017; Hammond & Toomey, 2003; Schmandt & Humphreys, 2010b; Toomey et al., 1994).

An important aspect of our tomographic method is the starting model, which influences the predicted travel times and ray paths. By using starting models that include known variations in elevation and near surface structure we eliminate the need for using undamped station corrections. Our starting model explicitly includes elevation and uses results of regional Rayleigh wave studies to constrain absolute velocities in the upper 50 km (Bell et al., 2016; Brocher, 2005; Schmandt & Lin, 2014); see Supporting Information. To reduce the effects of local structure beneath a station and to account for

minor timing errors in the offshore data, we solve for heavily damped station statics, with a RMS of 0.1 s. Our station static terms are small (5-10 times less) compared to the contributions of our shallow starting model and relative to similar studies that do not directly account for either elevation or variations in near surface structure (e.g., Hawley et al., 2016). For the results shown below, the initial RMS misfit for the delay-time data, relative to the AK135 1D velocity model (Kennett et al., 1995) that does not include elevation is 0.51 s. Relative to our 3D starting model that includes elevation, the RMS misfit is 0.42 s; a variance reduction of 31%. After 5 tomographic iterations, the final RMS misfit, relative to the 3D starting model, is 0.28 s, a variance reduction of 70%.

3.0 Tomographic Results

Figure 2 shows our preferred tomographic model. A prominent east-dipping, high-velocity anomaly is imaged throughout the region, consistent with the location of the subducting JdF slab (Schmandt & Humphreys, 2010a). The high-velocity anomaly is continuous along-strike in the upper 150 km, but exhibits significant variability below 150 km, with decreased amplitudes throughout the central section, referred to as the “slab hole” (Roth et al., 2008). The high-velocity anomaly extends to a depth of 350 km in the north and south. We clearly image the southern extent of the inferred slab; however, its northern limit is less certain due to limited station coverage. The magnitude of the slab anomaly is about 2% but is up to 4% in some areas.

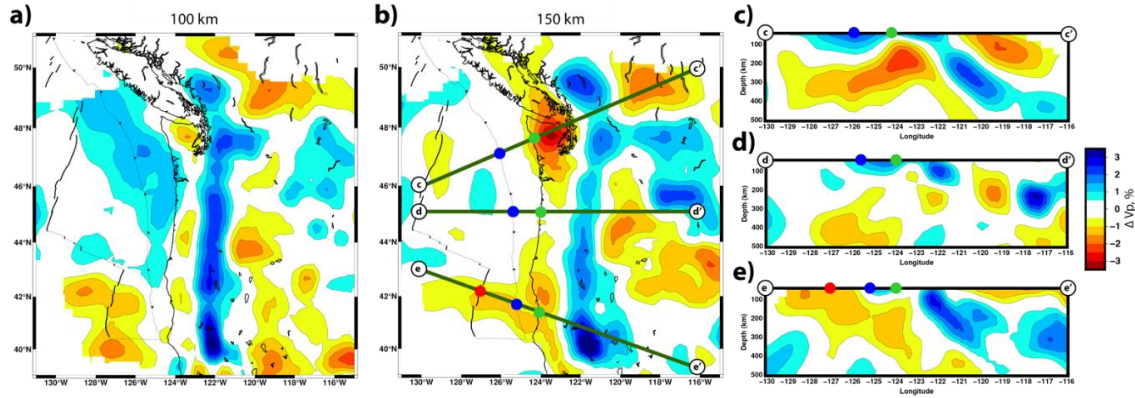


Figure 2: **a**, Map view slice at 100 km depth. North-south trending high-velocity anomalies (122°W) are inferred to be the subducting slab. Offshore, there are significant differences in structure beneath the Juan de Fuca and Gorda regions (Byrnes et al., 2017). **b**, Map view slice at 150 km depth. Green lines show locations of vertical sections shown in c-e. Two low-velocity anomalies are imaged beneath the subducting slab in northern and southern Cascadia. **c**, Vertical section along a line connecting Axial Seamount and the northern low-velocity anomaly. Orientation is sub-parallel to absolute motion of the Juan de Fuca plate and parallel to SKS splitting direction (Bodmer et al., 2015). **d**, Vertical section through central Cascadia. **e**, Vertical section through the southern low-velocity anomaly and the Gorda deformation zone. Orientation is parallel to absolute motion of the Pacific plate (DeMets et al., 2010).

We image two distinct low-velocity anomalies beneath the forearc of the subducting slab in northern and southern Cascadia (Figure 2b). Low-velocity anomalies are absent beneath the slab in the forearc of central Cascadia (Figure 2d), indicating that sub-slab heterogeneities are local rather than margin-wide features, in contrast to previous work (Hawley et al., 2016). In southern Cascadia, deep low-velocity anomalies (100-250 km, $\Delta V_p \sim -1.5\%$) are present beneath the slab and at the southern slab edge boundary; these low-velocity anomalies extend northward to $\sim 43^{\circ}\text{N}$ and connect to shallower (<100 km) low-velocity anomalies below the Gorda deformation zone (Byrnes et al., 2017) (Figure 2e). The lateral extent of the shallow anomalies correlates well with the boundaries of the Gorda deformation zone (Chaytor et al., 2004). In northern Cascadia, a larger ($\Delta V_p \sim -3\%$) low-velocity anomaly lies sub-slab beneath northwestern Washington and Vancouver Island, with peak amplitudes beneath the Olympic Peninsula. A cross-section sub-parallel to JdF absolute plate motion (Figure 2c), shows a low-

velocity anomaly that extends continuously from the JdF Ridge; this anomaly increases in amplitude as it shallows from approximately 300 to 150 km depth toward the CSZ.

Previous studies have imaged low-velocities in parts of the sub-slab region (Chen et al., 2015; Hawley et al., 2016; Roth et al., 2008; Schmandt & Humphreys, 2010a; Schmandt & Lin, 2014; Xue & Allen, 2010), however most lack offshore data necessary to constrain structure beneath the JdF plate and none have investigated their relationship to megathrust segmentation. Hawley et al. (2016) do incorporate offshore CI data and image a laterally continuous, margin-wide low-velocity anomaly sub-slab, interpreted as accumulation of buoyant asthenosphere. Due to the margin-wide nature of the anomaly, correlations to megathrust segmentation cannot be made. We attribute differences in our results to key differences in our methodology, specifically our use of a detailed 3D starting model (including elevation) rather than station statics to account for shallow structure and our iterative 3D raytracing approach to solving the forward problem. Chen et al., (2015) image localized low-velocity anomalies consistent with our results, postulating they may be regions of mantle upwelling, but lack the offshore constraints to explore their potential origins as we do here (See 4.1).

Figure 3a-c shows a strong correlation between our tomographic results and previous indicators of megathrust segmentation in Cascadia. In particular, the depth-averaged (100-250 km) low-velocity anomalies beneath the subducted JdF slab in northern and southern Cascadia compare well with increases in geodetically-inferred plate locking (Schmalzle et al., 2014) and tremor density (Wells et al., 2017). Conversely, the central segment of Cascadia, which lacks a sub-slab, low-velocity anomaly in the forearc, is characterized by decreased locking and lower tremor density.

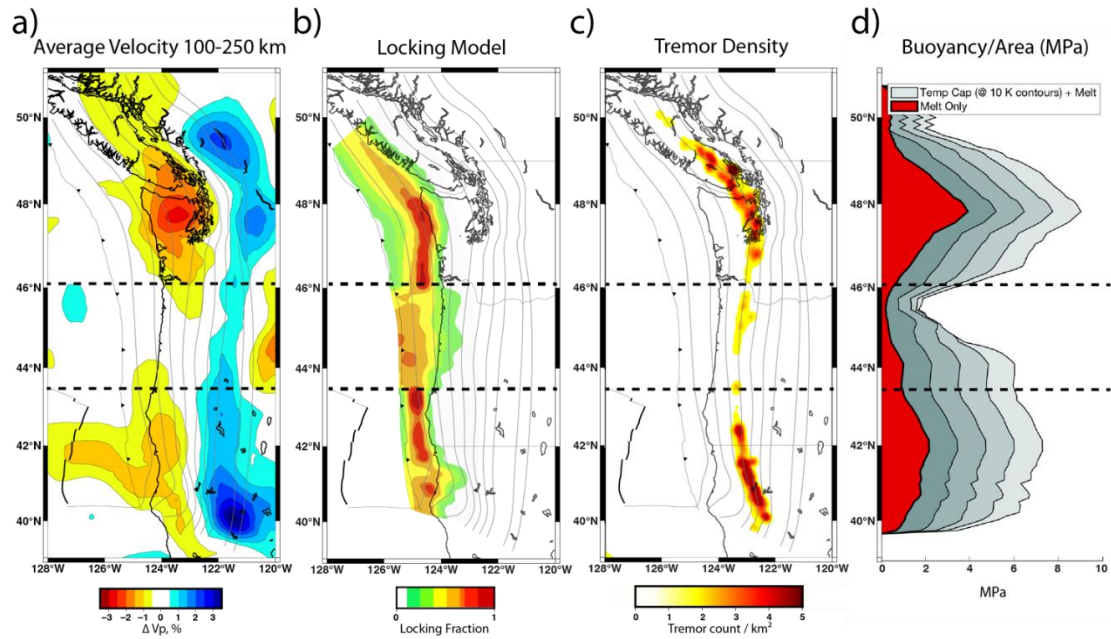


Figure 3: a, Average P -wave velocity anomalies between 100 and 250 km depth. Horizontal and dashed lines in each panel indicate approximate boundaries of megathrust segmentation. Gray contours (10 km intervals) indicate depth to top of subducting plate (McCrory et al., 2012). b, Fraction of plate locking modeled from geodetic data (Schmalzle et al., 2014). c, Density of tremor events from 2009–2015 detected at Pacific Northwest Seismic Network stations (<http://www.pnsn.org/tremor/>). d, Buoyancy variations beneath the subducted slab inferred from our depth-averaged velocity model. Buoyancy variations are shown due entirely to partial melt (red) or a combination of temperature and melt (grey shading; contours represent 10 K increases in the maximum allowed temperature). See text for further discussion.

4.0 Interpretation

The remarkable spatial consistency between segmentation of sub-slab low-velocity anomalies, plate locking, and tremor density (Figure 3a-c) suggests that deep mantle structure beneath subducting slabs may influence megathrust behavior over a range of down-dip intervals. We postulate that the most likely cause for this correlation is that sub-slab buoyancy modulates the plate coupling force at the thrust interface. While we consider the low-velocity anomalies in northern and southern Cascadia to be independent features, we present evidence that both represent regions of upwelling, decompression melting, and possibly temperature anomalies due to local mantle dynamics, and thus give rise to excess buoyancy.

4.1 Geodynamic Interpretation of Low-Velocity Anomalies

We attribute the low-velocity anomaly in southern Cascadia to northwest-directed mantle upwelling and consequential decompression melting that extends from the underside of the subducted slab upward and toward the Gorda deformation zone (Figure 2e). We infer that Pacific plate motion to the northwest draws material from beneath a slowly moving Gorda deformation zone, making the sub-slab mantle a significant source region for mantle upwelling. Our reasoning is as follows: The Gorda deformation zone is a diffuse plate boundary (Wilson, 1986) that is pinned kinematically between the Pacific and JdF plates, which imposes north-south compression (Wang et al., 1997). This causes internal deformation resulting in reduced and asymmetric spreading along the southern Gorda Ridge (Chaytor et al., 2004) and stagnation of the Gorda deformation zone in an absolute reference frame (Riddihough, 1984). As a result of this stagnation and nearby plate motions, asthenospheric deformation beneath the diffuse plate boundary records Pacific-JdF relative plate motion (Bodmer et al., 2015; Martin-Short et al., 2015), a pattern significantly different than that observed beneath the JdF plate. As the Pacific plate draws Gorda asthenosphere northwest, the dipping slab to the east impedes westward lateral flow into the Gorda region, promoting sub-slab upwelling. This scenario also explains the southeast-to-northwest trending low-velocity anomalies that do not correlate with the trend of the Gorda Ridge but correlate well with the extent of the diffuse plate boundary (Figure 2b).

In northern Cascadia, we attribute the sub-slab low-velocity anomaly (Figure 2c) to thermally buoyant mantle derived from nearby oceanic hotspots. Figure 2c and S8c-d show that the sub-slab velocity anomaly extends back toward the northern JdF Ridge and

intersects the ridge north of Axial Seamount, in a region where ridge mantle structure is most asymmetric and geochemical anomalies are observed (see Fig. 15 of Byrnes et al., 2017). Several oceanic hotspots have been identified in a northwest-southeast trend in the northeastern Pacific, including the Cobb, Bowie, and Anahim hotspots (Mercier et al., 2009; Zhao, 2007). The Cobb hotspot, for example, is currently located near the JdF Ridge, its most recent surface expression being Axial Seamount (Figure 1a), and has an estimated thermal anomaly of 30-40 K (Hooft & Detrick, 1995). This hotspot arrived at the ridge 0.5 My ago and has been within 150 km of the ridge for 10 My (Chadwick et al., 2014). Since typical hotspot widths are 100-200 km diameter (Zhao, 2007), 10 My is sufficient time for hotspot material to be entrained northeast toward the CSZ along a trend sub-parallel to both absolute plate motion and the observed SKS splitting directions (Bodmer et al., 2015; Martin-Short et al., 2015). We thus infer that as hotspot-influenced material approaches the migrating JdF Ridge it interacts with its mantle flow field. Due to ridge migration, asymmetric flow develops (Bell et al., 2016; Byrnes et al., 2017; Conder et al., 2002; Toomey et al., 2002), and some sub-ridge mantle is transported to the east of the ridge at depth. Because the buoyancy flux of hotspots in the NE Pacific are small (Courtilot et al., 2003; Sleep, 1990) ascent rates are slow, and the anomalous mantle gradually shoals toward the CSZ (Figure 2c) resulting in decompression melting. Our results and interpretation are inconsistent with Gao (2018), who suggests a correlation between their imaged low-velocity slab in central Cascadia and reduced seismicity, postulating that eastward migration of Cobb hotspot material could explain their results. Given the northeastward JdF plate motion, SKS splitting observations consistent with plate motion, and our observed low-velocity anomaly extending northeastward from the

JdF Ridge to northern Cascadia, we find it more likely that hotspot material would be transported northeastward and accumulate beneath northern Cascadia, as opposed to central Oregon.

4.2 Estimation of Physical Parameters

Variations in the physical properties (temperature, melt fraction, and density) and buoyancy of the sub-slab, forearc region are estimated from the vertically-averaged low-velocity perturbations between 100-250 km depth. Because the tomographic method constrains only relative variations in velocity, we cannot estimate the absolute values of temperature and melt fraction. However, we can estimate the variations in these properties that are consistent with the tomographically imaged perturbations. To do so, we assume that temperature and melt anomalies are zero at a reference $\Delta V_p = 0\%$ and only consider low-velocity anomalies in the sub-slab, forearc region.

First, melt fraction variations are calculated assuming the entire velocity anomaly is due to melt (Figure S6a). We assume that 1% partial melt results in a 3.6% P-wave velocity reduction (Hammond & Humphreys, 2000). Next, temperature variations are computed using:

$$\frac{\partial \ln V_p}{\partial T} (\times 10^{-4} K^{-1}) = -0.88$$

from Karato et al. (2008), assuming a Q_p value of 300. Relatively high Q is observed beneath the JdF in regions far from the ridge (Eilon & Abers, 2017).

For melt and temperature variations, we calculate density using:

$$\rho = \rho_0(1 - \alpha\Delta T - \beta\xi) - \Delta\rho\phi$$

from Jha et al. (1994) (Figure S6c), where ρ_0 is the mantle reference density of 3300 kg/m³, $\alpha = 3 \times 10^{-5} \frac{kg}{m^3K}$ is the thermal expansion coefficient, and ΔT is the temperature

anomaly. The $\beta\xi$ term represents a change due to mantle depletion, where $\beta = 0.024$ and ξ is the degree of mantle depletion which we set equal to the fraction of partial melt. The $\Delta\rho\phi$ term is the density contrast between melt and solid mantle, where $\Delta\rho = 500 \frac{kg}{m^3}$ and ϕ is the melt fraction. We note that density reductions are greatest for temperature anomalies and effectively negligible for depletion. From these density variations, we calculate lateral buoyancy variations per unit area ($\Delta\rho gh$) in a 2° wide swath limited eastward by the 40 km slab interface contour using $h=150$ km (Figure S6d).

4.3 Sub-slab Buoyancy and its Influence on the Megathrust Interface

Figure 3d shows along-strike changes in vertical stress due to sub-slab buoyancy calculated from average velocities between 100-250 km depth. Excess vertical stresses of 4 MPa and 2 MPa (northern and southern Cascadia, respectively; red area Figure 3d) are predicted due to sub-slab buoyancy forces, assuming variations are due entirely to partial melt (0.6% and 0.3%, respectively). Assuming variations due entirely to temperature, increases of 250 K and 125 K are estimated for the northern and southern velocity anomalies, respectively (Figure S6b). We consider variations in temperature of this magnitude unlikely in the asthenosphere without crossing the solidus and generating partial melt. Thus, we choose to cap the maximum allowed temperature variation and attribute the remaining anomaly to melt. The maximum temperature explored is 40 K which is equivalent to the maximum temperature anomaly inferred for the Cobb hotspot (Hooft & Detrick, 1995). This increases the buoyancy-induced stresses by a factor of two (grey lines Figure 3d).

In northern Cascadia, we attribute excess buoyancy to a combination of a hotspot-related thermal anomaly and decompression melting, whereas excess buoyancy in

southern Cascadia may be predominantly due to decompression melting. Buoyancy forces of this size are comparable in magnitude to median subduction zone stress drops (3 MPa) (Allmann & Shearer, 2009) and estimates of the shear stress on the CSZ fault (<10 MPa) (Wang et al., 1995).

Figure 3 shows that along the entire margin of the CSZ there is a positive correlation between sub-slab buoyancy, the locking fraction of the megathrust, and the occurrence of episodic tremor. These relations support our main conclusion that sub-slab buoyancy modulates the plate coupling force at the thrust interface in both the locked and transitional regimes. Figure 4 shows a schematic cross section depicting the down dip relationships between sub-slab buoyancy, plate locking and the ETS zone. We suggest that buoyancy forces in the oceanic asthenosphere play a previously unrecognized role in localizing megathrust segmentation. Processes such as fluids and heterogeneous crustal structures, while still critical controls on megathrust behavior, could work in tandem with buoyancy forces.

We suggest two possible mechanisms for how sub-slab buoyancy could increase the plate coupling force in the seismogenic zone: a local increase in effective stress or a local change in slab dip. Slab buoyancy variations due to lithospheric age have been linked to earthquake size distributions (Nishikawa & Ide, 2014; Scholz, 2015), with the subduction of younger, more buoyant lithosphere resulting in a greater frequency of large earthquakes. Similarly, earthquake distributions are linked to stresses at the fault (Scholz, 2015; Spada et al., 2013), with larger differential stresses corresponding to a greater frequency of large earthquakes. We suggest that sub-slab buoyancy variations may locally increase effective stress at the interface, increasing the shear strength.

Alternatively, buoyancy forces sub-slab should oppose the typical loading forces associated with plate flexure, eliciting a morphologic response from the subducting slab. Some evidence of such a response may be manifest in the more concave upward slab interface contours and shallower slab dip angles in the northern and southern Cascadia interface (McCrorry et al., 2012). Shallower dip angles cause an increase the downdip length of the coupled interface which results in larger resistive shear force (Wang & He, 1999; Wang & Suyehiro, 1999).

We speculate that the spatial correlation between sub-slab buoyancy and ETS may be due to the potential of buoyancy to influence stress on large spatial scales, though the exact mechanism relating them is unknown. The co-location of ETS and plate locking along-strike define megathrust segments, however, given the relationship between ETS and decreased effective stress (Kodaira et al., 2004; Obara, 2002), it is unclear why they should occur together and suggests that down dip variations in stress are complex. One possibility is that effective stress is modulated down-dip due to eastward reduction in sub-slab buoyancy. In support of this possibility, increased tremor density is observed above the eastern edge of the buoyant sub-slab regions (Figure 4). The transition from sub-slab buoyancy to slab-pull forces could lead to rapid stress changes down dip causing a decrease in effective stress.

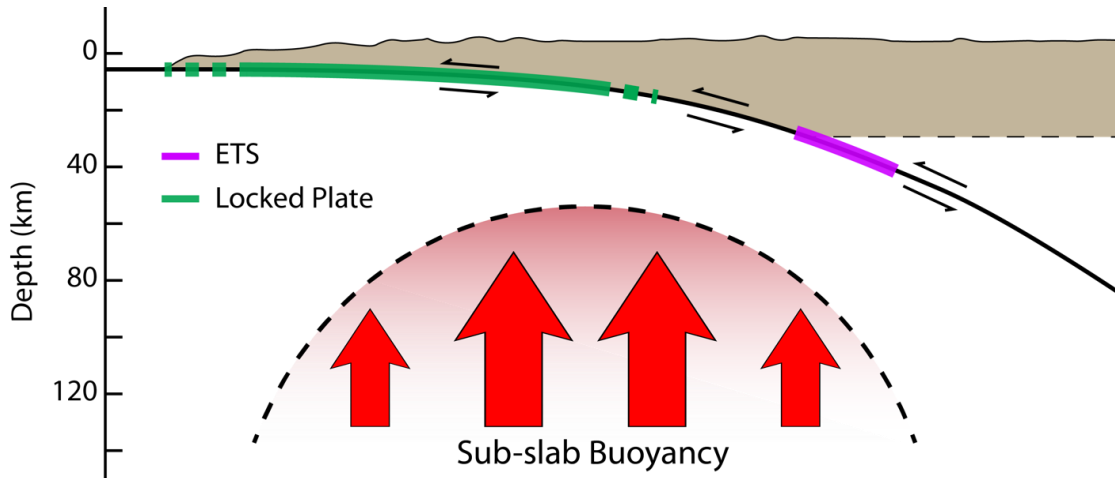


Figure 4: Conceptual vertical cross-section representing the northern and southern segments of Cascadia where sub-slab velocity anomalies, increased plate locking, and increased tremor density coincide. Red region represents excess sub-slab buoyancy forces associated with imaged low-velocity anomalies. Green shading represents the locked portion of the subduction zone and purple shading represents the ETS zone.

5.0 Conclusions

We present onshore-offshore P-wave tomography of the Cascadia subduction zone which highlights localized low-velocity anomalies beneath the subducting slab in northern and southern Cascadia. We interpret these anomalies as regions of local mantle upwelling associated with melt and/or temperature anomalies. Physical parameter estimates derived from our model reveal excess buoyancy in northern and southern Cascadia which correlate well with increased plate locking and tremor density along-strike. We suggest that sub-slab buoyancy influences the localization of megathrust segmentation by modulating the plate coupling force at the interface.

The degree to which sub-slab buoyancy affects segmentation at subduction zones globally is unknown. The CSZ may be an endmember as it is young, hot, narrow, and seismically quiet (Heaton & Hartzell, 1987). Sub-slab low-velocity anomalies have been observed in other subduction zones (Honda et al., 2007; Huang et al., 2013; Portner et al., 2017), though their relationship to megathrust segmentation remains to be explored.

6.0 Bridge

Chapter III investigated how heterogeneity in the Cascadia subduction zone subslab region, specifically local buoyancy anomalies, can influence megathrust behavior. Two low-velocity anomalies beneath the subducting slab in northern and southern Cascadia are imaged and are spatially collocated with regions of increased plate locking and increased tremor density. I hypothesize that these subslab anomalies can modulate the resistive shear forces on the plate interface, contributing to the segmentation of megathrust behavior. However, this does not address several other spatial correlations with subslab anomalies such as forearc topography, uplift rates, slab morphology, and erosion rates. In Chapter IV, I expand upon this hypothesis and investigate how subslab buoyancy may influence the processes responsible for uplifting and supporting the segmented forearc topography present in the Cascadia subduction zone. The proposed model links mantle dynamics and structure to surface process.

CHAPTER IV

ASTHENOSPHERIC BUOYANCY AND THE ORIGIN OF HIGH-RELIEF TOPOGRAPHY ALONG THE CASCADIA FOREARC

From Bodmer, M., Toomey, D. R., Roering, J., and Karlstrom, L. (Submitted).
Asthenospheric buoyancy and the origin of high-relief topography along the Cascadia
forearc. *Earth and Planetary Science Letters*.

1.0 Introduction

The mechanics of convergent margins influences the forces that generate and support forearc topography (Cattin et al., 1997). Forearc morphology varies both globally and within subduction zones (Bassett & Watts, 2015) and many convergent margins exhibit along-strike variations in plate locking and seismicity (Ando, 1975; Kopp, 2013). Most studies investigating subduction zone segmentation focus on properties of the thrust interface or adjacent crust (Brudzinski & Allen, 2007; Cloos, 1992; Delph et al., 2018; Littel et al., 2018). Recent findings, however, suggest that dynamics of oceanic asthenosphere beneath the down-going plate contribute to segmentation (Bodmer et al., 2018). Here, we explore the relationship between upper mantle processes, megathrust dynamics, and the evolution of the forearc landscapes.

We focus on the Cascadia subduction zone, exploiting the wealth of observations spanning large spatial (upper mantle to surface) and temporal (decades to millions of years) scales. Two regions of high-relief topography are present in the forearc (the Olympic and the Klamath ranges; Figure 1), separated by the relatively low-relief Oregon Coast Range. Similarly, there is evidence from multiple observations for segmentation of

megathrust behavior, specifically from historic large earthquakes, episodic tremor and slip, inferred plate locking, and seismicity (Brudzinski & Allen, 2007; Goldfinger et al., 2012; Li et al., 2018; McCrory et al., 2012; Schmalzle et al., 2014; Wells et al., 2017). Previous work suggested that differences in incoming plate age drive topographic variation (Kelsey et al., 1994), however we show that more recent observations are inconsistent with this interpretation.

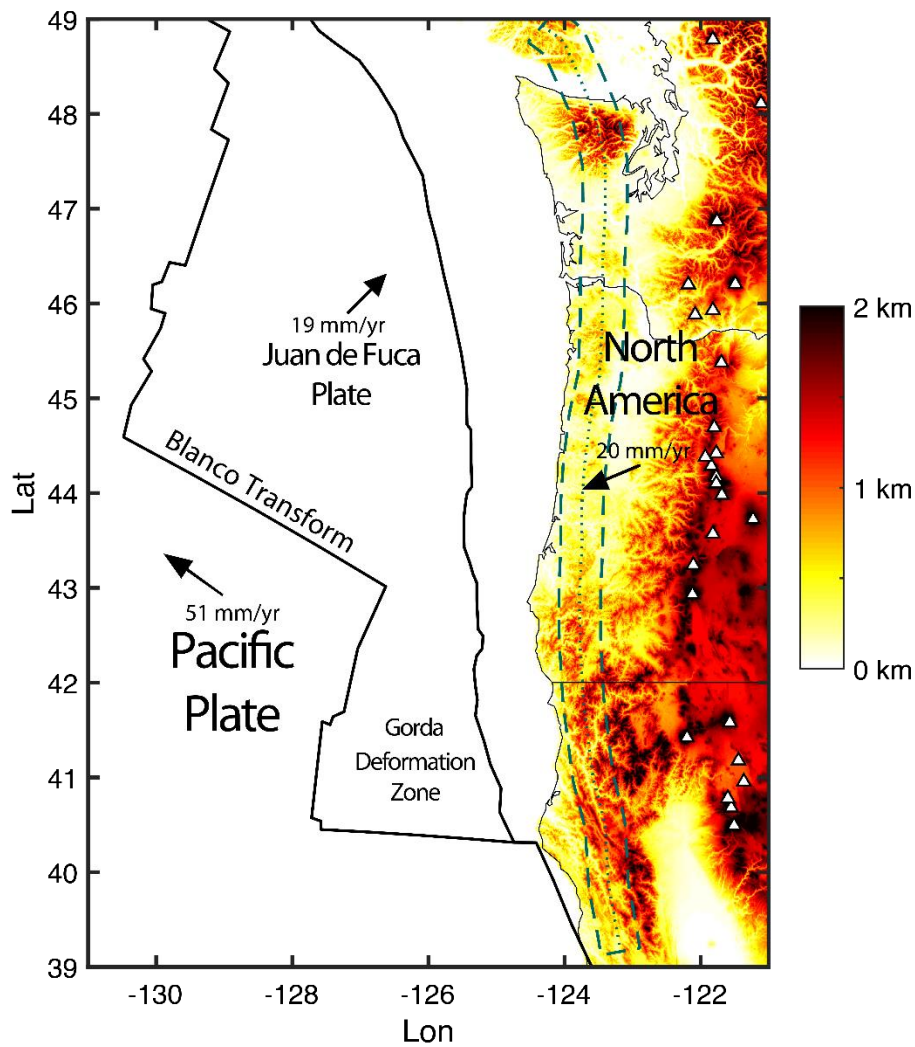


Figure 1: Topographic map of the Cascadia subduction zone. Regions of high forearc topography are observed in northern and southern Cascadia, the Olympic and Kalamath ranges, respectively. Arrows represent absolute plate motions. White triangles represent current and historic volcanism. Green lines denote the swath used to plot several of the datasets in subsequent figures.

In this paper, we synthesize along-strike characteristics of the Cascadia margin in order to address two questions: 1) What conditions give rise to long-term uplift and development of differential topography in the forearc? 2) What are the mechanisms that support current forearc topography? We infer that buoyant asthenosphere beneath the subducting slab (Bodmer et al., 2018) influences both of these processes by modulating megathrust properties (slab morphology and/or coupling of the plates) and thus driving the first-order response of the overlying landscape.

2.0 Tectonic Setting

The Cascadia subduction zone (CSZ) is where the Juan de Fuca (JdF) plate converges with North America at a rate of ~40 mm/yr (Figure 1). The CSZ rupture cycle is estimated to be 300-500 years, with the last great earthquake (M9.0) occurring in 1700 AD (Goldfinger et al., 2012). The offshore plate system includes the JdF and two smaller fragmenting regions, the Explorer plate and Gorda deformation zone (GDZ), to the north and south respectively. The age of JdF crust entering the subduction zone is young (<10 Ma). Beneath the forearc, ages vary gradually along-strike, despite the presence of the Blanco Fracture Zone (BFZ) offshore. This is because the BFZ is a recent feature (~4Ma) resulting from plate reorganization in the last ~8 Ma (Riddihough, 1984; Wilson, 2002; Figure S1). The convergent margin is short, ~1000 km in length, yet multiple studies indicate that structure and behavior vary along-strike. We define 3 main segments (northern, central, southern; Figure 1) from observations of megathrust behavior (see Sec. 3) in order to locate and compare key features.

The Olympic mountain range is a forearc high (peaks >2 km above sea level) located in northwest Washington, in the northern segment of Cascadia (Figure 1).

Glaciation in the Olympics is present currently at altitudes of 1.7 km (Fountain et al., 2017) and average relief (within a 2.5 km radius) reaches ~1.2 km (Figure S2). This region is comprised of Miocene marine sedimentary rocks and is a sub-areal subset of a larger regional subduction complex (Tabor & Cady, 1978). The mountainous core is surrounded by a horseshoe shaped belt of Eocene oceanic basalt (Tabor & Cady, 1978). These basalts are a part of the large igneous province Siletzia, which extends south into central Oregon and was accreted ~50 Ma (Wells et al., 2014). The Olympics are located inboard of a change in margin strike and have a small lateral wavelength (~100 km). High elevations are also observed just north in the Vancouver portion of the Wrangellia terrain. Uplift of the Olympics started ~18 Ma and topography is thought to be steady state, implying average rates of uplift and erosion that are nearly equivalent over the region (Brandon et al., 1998; Brandon & Calderwood, 1990; Pazzaglia & Brandon, 2001).

The Klamath range is a forearc high (peaks >2 km above sea level) located in northern California and southern Oregon, in the southern segment of Cascadia (Figure 1). Glaciation in the Klamaths is currently present in a small area (<2 km²) located in the Trinity Alps (Fountain et al., 2017) and average relief (within a 2.5 km radius) reaches ~1 km (Figure S2). The formation is comprised of various oceanic terrains accreted during the Paleozoic through to Jurassic time (Snook & Barnes, 2006). The Klamaths are located east of the GDZ and north of the Mendocino triple junction, the transition from transform motion along the San Andreas to convergence at the CSZ. Uplift of the Klamath range is thought to have initiated most recently in the last ~3 Ma, as inferred from the presence of a well-developed erosional surface in the western range, the Klamath peneplane, at ~5

Ma (Aalto, 2006; Diller, 1902; Mortimer & Coleman, 1985). Evidence of earlier (Oligocene-Eocene) topographic development associated with the accretion of Siletzia has been inferred for the southeasternmost Klamaths (Piotraschke et al., 2015).

Separating the Olympics and Klamath ranges are the relatively low-relief Coast Ranges, located in the central segment (Figure 1). The Coast Ranges exhibit average topography less than 0.5 km above sea level (peaks reaching 1 km) and are unglaciated. The Coast Ranges are comprised of Eocene sedimentary deposits overlaying the accreted Siletzia terrain (Heller & Ryberg, 1983). Uplift of the Coast ranges is thought to have occurred 15-16 Ma (McNeill et al., 2000) with consistent erosion rates that appear to balance uplift (Roering et al., 2007).

3.0 Results from Previous Studies

To address the development and mechanical support of forearc topography in Cascadia, we first synthesize observations and inferences from previous work. These studies span several spatial and temporal scales, addressing: erosion and vertical uplift of the forearc (Sec. 3.1); role of isostasy in supporting forearc topography (Sec. 3.2); structure and dynamics of the upper mantle beneath the subducting slab (Sec. 3.3); properties of the subducting plate interface (Sec. 3.4); and mechanical modeling of the forearc relating plate interface forces to forearc characteristics (Sec. 3.5).

3.1 Landscape Evolution of the Cascadia Forearc

Vertical motion of the Cascadia forearc varies along-strike, with the spatial patterns from multiple observations reflecting the segmentation boundaries defined by megathrust behavior (Figure 2). These observations broadly fall into two categories: short-term processes on the scale of an individual seismic cycle and long-term processes

occurring over many seismic cycles, up to millions of years. Observations across scales suggest increased vertical motion in the northern and southern segments.

Topographic highs are observed in the northern and southern segments of the Cascadia forearc corresponding to the Olympic and Klamath ranges respectively. The topographic profile, Figure 2a, is derived from 30 m resolution DEM's within a ~100 km wide swath (see Figure 1). Local maximum elevations in the northern and southern segments are 2.2 km and 1.9 km with mean elevations of roughly 1.4 km and 1.0 km, respectively. Comparatively, central Cascadia's coast range only reaches a maximum elevation of 1.0 km with a mean elevation of 0.4 km. The forearc highs differ in wavelength, with the Olympics being a narrow feature (~100 km width) and the Klamath's more laterally expansive (~300 km width). These topographic patterns reflect the net result of the competition between vertical uplift and denudation processes and it is unlikely that they are the result of rock type variation (Kelsey et al., 1994). Although our analysis doesn't require it, long-term uplift and erosion data support an approximate balance between uplift and erosion and steady topographic form.

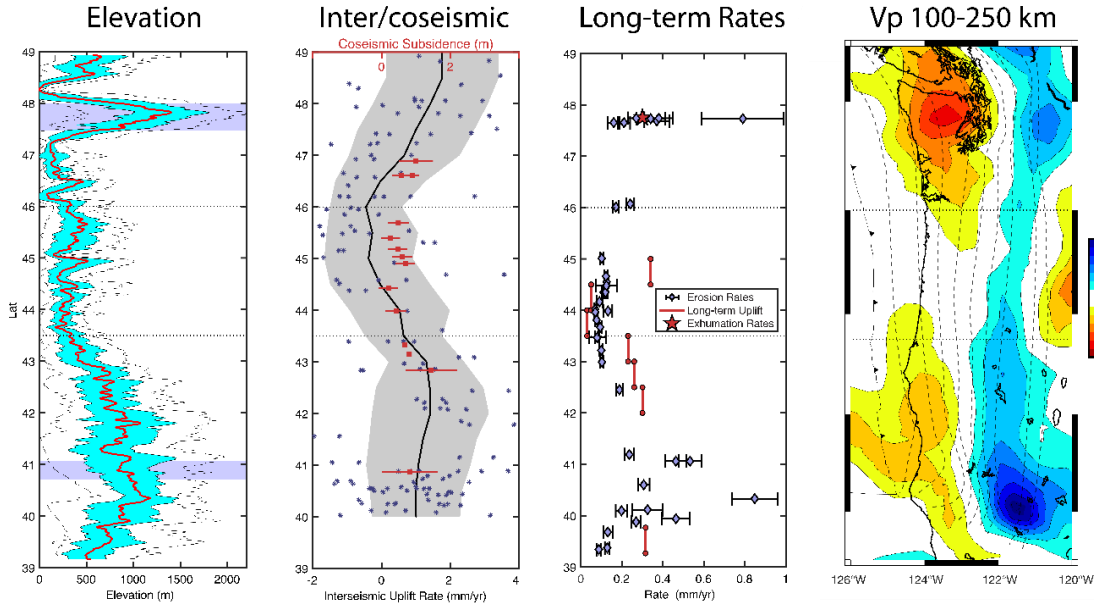


Figure 2: Along-strike variations in the landscape evolution of the Cascadia forearc. Horizontal dashes at 46N and 43.5N represent inferred segment boundaries separating northern, central, and southern segments. Left) Forearc topographic within the swath (Figure 1). Red line represents mean elevation, dashed lines represent minimum and maximum elevations, and blue area represents the standard deviation. Purple bars represent latitudes where Pleistocene glaciation is observed in the forearc. Center-Left) Interseismic uplift rates and coseismic subsidence. Blue dots represent individual GPS vertical velocities (within and to the west of the swath), black line represents the average vertical velocity, and the shaded region is the standard deviation. Red symbols represent coseismic subsidence during the 1700 event. Note the two datasets are plotted on different scales. Center-Right) Long term uplift rates and erosion rates. Red lines represent averaged long-term uplift rates from shorecut platforms. The red star represents exhumation rate estimate from the Olympics. Purple diamonds represent erosion rates from cosmogenic radionuclide concentrations. Right) Tomographic image of relative P-wave velocities averaged between 100-250 km depth. This depth represents the slab region. Dashed lines represent slab depth contours (10 km increments).

Measurements of short-term vertical motion are larger in the northern and southern segments, co-located with regions of high topography (Figure 2b). Observations come from GPS measurements and coseismic subsidence estimates, both of which capture deformation during a single seismic cycle. GPS measurements from Plate Boundary Observatory (PBO) stations display average vertical motions of 1-2 mm/yr in northern and southern Cascadia, with maximums reaching 5 mm/yr (Figure 2b; Schmalzle et al., 2014). Conversely, average vertical motions in central Cascadia are indistinguishable from zero. The variance of GPS derived velocities is large; however, the pattern of observations is corroborated by tide and leveling gauge studies (Burgette et

al., 2009). Estimates of coseismic subsidence during the 1700 Cascadia megathrust rupture, derived from tidal microfossil studies (Wang et al., 2013), show a decrease in subsidence within the central segment (0.5-1 m compared to the north/south segments; Figure 2b). Wang et al., (2013) infer a heterogeneous rupture pattern with four high slip patches, but in general coseismic subsidence is lower in central Cascadia, observed over multiple events (Leonard et al., 2010).

Estimates of long-term vertical motion, averaging over many seismic cycles, display similar patterns with increased uplift and erosion rates in the northern and southern segments (Figure 2c). Long-term uplift rates, averaged from shoreline platform analysis estimates (Balco et al., 2013; Kelsey et al., 1994, 1996), and exhumation rates, from apatite fission track analysis (Brandon et al., 1998), show increased rates north and south compared to the central segment (Figure 2c). Compiled erosion rate estimates, derived from cosmogenic radionuclide data, suggest rates approaching 1 mm/yr in northern and southern Cascadia, whereas central Cascadia rates are lower, ~0.2 mm/yr (Figure 2c; Balco et al., 2013; Bierman et al., 2001; Ferrier et al., et al., 2005; Fuller et al., 2009; Livermore, 2001; Marshall et al., 2017; Penserini et al., 2017; Roering 2015). We choose to report cosmogenic radionuclide erosion rates because they are robust against anthropogenic change. Consistent with the notion of steady state topography, the magnitudes of long-term uplift rates and erosion rates are broadly in agreement. However, long-term uplift and erosion rates are approximately an order of magnitude lower than the short-term, interseismic uplift rates (Figure 2b-c; Penserini et al., 2017), which reflect the earthquake deformation cycle similar to other subduction zones (Ramírez-Herrera et al., 2018).

3.2 Isostasy of the Subducting Plate and Overriding Crust

Here we estimate the isostatic contributions of the subducting slab and the overriding crust to forearc elevation; subslab contributions are addressed in Sec. 3.3. We show that contributions due to oceanic plate age are negligible and our results imply insufficient accommodation space above the subducting slab for the crustal thickness variations required to support topography.

Kelsey et al. (1994) suggested that isostatic adjustments due to along-strike changes in plate age support forearc topography, with high-standing relief underlain by younger oceanic crust. Their study assumed that the BFZ corresponds with a >10 My age offset in oceanic lithosphere beneath the forearc that migrates northward. Reorganization of the JdF plate system and subsequent development of the BFZ, however, did not begin until ~8 Ma and ~4 Ma, respectively (Riddihough, 1984; Figure S1). A more recent plate reconstruction by Wilson (2002) shows that plate age beneath the forearc differs by at most 4 My and that age does not correlate with the forearc relief pattern (Figure 3a). Further, using a half-space cooling model and plate ages from Wilson (2002), we calculate ~200 m of isostatic elevation variation, an order of magnitude lower than the observed topography (Figure 3c), which is less than half the previous estimate (Kelsey et al., 1994).

Using the depth to the slab interface as an absolute bound on crustal thickness, we find that there is insufficient space for the thickness of continental crust needed to isostatically support topography. Figure 3b shows an estimate of the maximum possible thickness of the crust beneath the forearc, assuming that continental crust extends down to the slab interface of McCrory et al. (2012). Notably, despite the high standing

topography in southern Cascadia, the forearc crust is relatively thin in this region. Global studies indicate an average elevation of 800 m and crustal thickness of 38 km (Amante & Eakins, 2009; Christensen & Mooney, 1995), which we use as an isostatic reference.

Assuming average crustal and mantle densities of $2.8 \frac{g}{m^3}$ and $3.3 \frac{g}{m^3}$, respectively, crustal thicknesses of 43 km and 40 km are required to isostatically support the mean topography in northern and southern Cascadia. This is 5-15 km thicker than the local depth to the slab interface (Figure 3b; McCrory et al., 2012) and crustal thickness estimates for the region (Gilbert, 2012; Shen et al., 2013). In contrast, crustal thickness in central Cascadia are consistent with isostatic support (Figure 3b), though other forces likely contribute to topographic development and support.

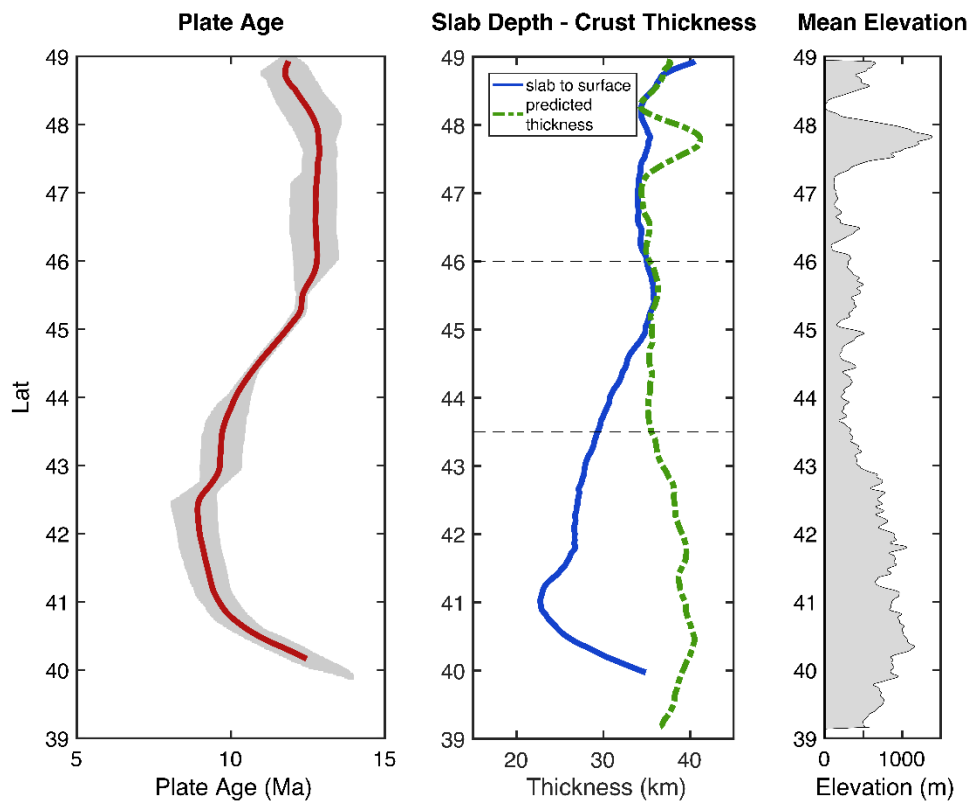


Figure 3: Left) Plate age variations beneath the forearc swath (see Figure S1). Red line represents the average and the gray area the total range of the data. Center) Comparison of slab depth to predicted crustal thickness. Blue line is the average depth to slab beneath the swath. Green line is the predicted crustal thickness from the observed topography assuming full isostatic compensation. Right) Mean elevation within the forearc swath.

We can also estimate along-strike changes in elevation due to crustal thickness variations and find that predicted patterns do not correlate with the observed topography (Figure S3). Crustal thickness variations are derived from seismic data (10-15 km difference) and the inferred surface-to-slab maximum (Gilbert, 2012; McCrory et al., 2012; Shen et al., 2013; Figure S4). This results in up to 2 km of topographic variation, however the along strike patterns are inconsistent with the observed topography. Lastly, we can estimate the along-strike changes in crustal density required to support the observed topography (Figure S3). We find average crustal densities of $2.2\text{-}2.6 \frac{g}{m^3}$ in the north and $2.3\text{-}2.5 \frac{g}{m^3}$ in the south are required. Using the Nafe-Drake curve (Brocher, 2005), this corresponds to average crustal V_p values (max 5.4 km/s) that lie more than 2σ below the global average (6.45 ± 0.23 km/s; Christensen & Mooney, 1995). We conclude from these comparisons that forearc topography in Cascadia is not supported isostatically by either the crust or the age of the subducting plate.

3.3 Subslab Buoyancy

A recent seismic study of the CSZ identifies two localized low-velocity anomalies beneath the subducting slab in northern and southern Cascadia (Figure 2d; Bodmer et al., 2018) that are co-located with regions of high topography, increased uplift rates, increased erosion rates, and larger coseismic subsidence (Sec. 2.1; Figure 2a-c). In northern Cascadia, the seismic anomaly ($\Delta V_p \approx -3\%$) is attributed to upwelling and decompression melting of relatively warm mantle entrained (Bodmer et al., 2015) from the nearby Cobb hotspot. In southern Cascadia the seismic anomaly ($\Delta V_p \approx -1.5\%$) is attributed to upwelling and decompression melting of asthenosphere from beneath the

subducting slab, driven by rapid northwest motion of the Pacific plate with respect to a relatively stagnant GDZ.

Due to presence of partial melt — and possibly a thermal anomaly in northern Cascadia — Bodmer et al. (2018) infer that these mantle upwellings generate positive buoyancy beneath the slab. If the subslab low-density anomalies present between 100 and 250 km depth are isostatically compensated by surface uplift, they would generate an along-strike pattern comparable to observed forearc relief, however, the magnitude of uplift (~200 m) would be an order of magnitude less than observed (Figure S3). A positive buoyancy force, however, would push upward on the base of the subducting plate with a force per unit area of 2-8 MPa (Bodmer et al., 2018; Figure 4a). These forces could deflect the subducting slab upward, resulting in regional scale variations in slab morphology and dip. Because density contrasts between the upwardly buoyant subslab asthenosphere and the overlying slab are small, the vertical deflection of the slab will be greater than the magnitude of surface uplift. Additionally, this buoyancy force could increase stress on the megathrust interface. In the next section (Sec. 3.4) we summarize observations at the slab interface consistent with these ideas.

3.4 Along Strike Variations of the Slab Interface

Geometry of the slab, as well as the coupling between plates, can influence both the stress accumulated and released during the seismic cycle (Bletery et al., 2016; Schmalzle et al., 2014) and the stresses that support the forearc wedge (Dahlen, 1990; K. Wang & He, 1999). Slab geometry and plate coupling are also properties that may be influenced by subslab buoyancy forces (Betts et al., 2012; Bodmer et al., 2018).

The morphology of the JdF slab interface varies both along-strike and down-dip (Bostock et al., 2019; McCrory et al., 2012; Figure 2d, 4c). Depth to interface estimates have been made for Cascadia down to 100 km depth, using earthquake locations and regional seismic studies (McCrory et al., 2012). First order features include a broad flattening of the subducting slab in the northern segment, where the strike of subduction rotates, and evidence of a slab buckle in the southern segment, near the Mendocino triple junction. There is also evidence for along-strike changes in the average dip angle within the shallow (<30 km depth) and potentially locked portion of the interface (Figure 4b). Average interface dip angles are shallower in the northern and southern segments, compared to the central segment, varying by 2.5° and 1.5° , respectively.

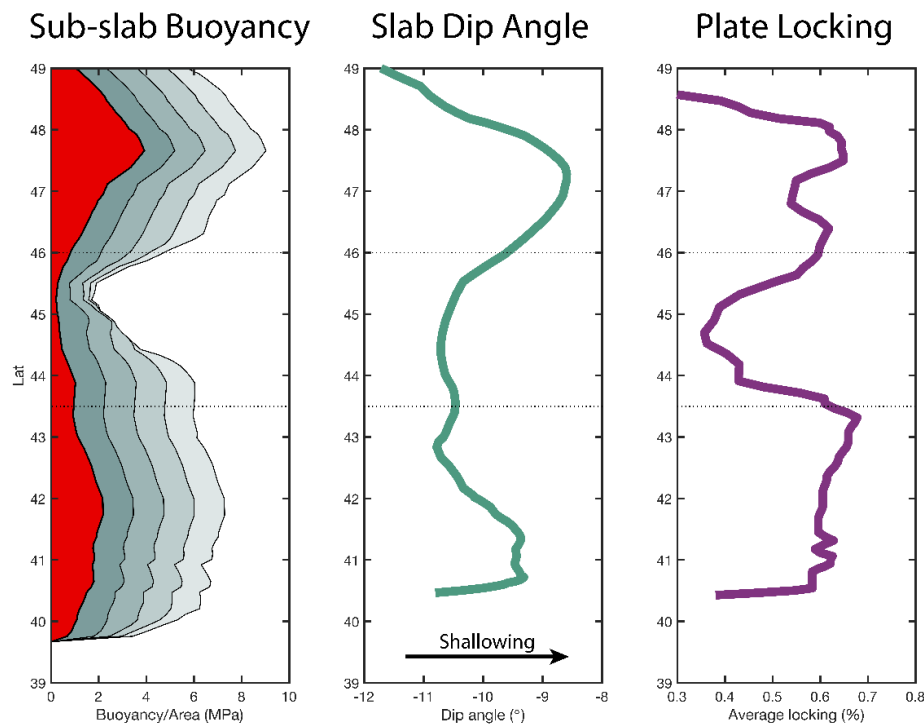


Figure 4: Along-strike variations in the subslab mantle, slab geometry, and along the megathrust interface. Horizontal dashes represent inferred segment boundaries. Left) Subslab buoyancy estimate inferred from the seismic tomography (Figure 3d). Red area represents buoyancy/area estimate if low-velocities are due solely to partial melt. Grey regions represent buoyancy/area estimates if temperature is allowed to contribute (temperature capped in increments of 10 K). Center) Average slab dip angle in the shallow portion of the megathrust interface. The maximum slab depth considered is 30 km. Right) Average plate locking. Average is taken in a 200 km wide swath around the maximum value for a given latitude using the Gaussian locking model.

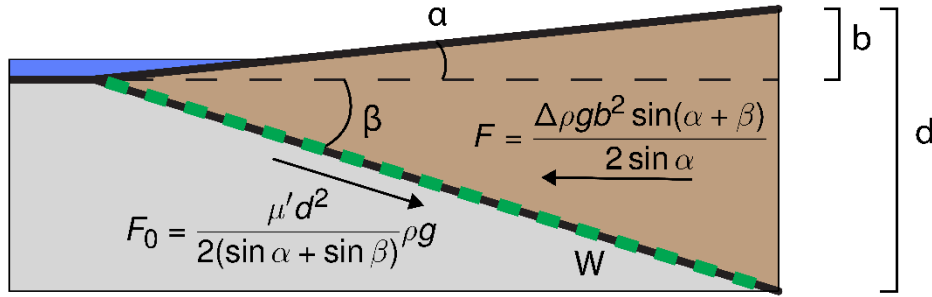
The degree of interface plate locking (coupling at a given moment in the seismic cycle), inferred from onshore geodetic observations (Li et al., 2018; Schmalzle et al., 2014), also display along-strike variation. Figure 4c estimates the average plate locking along-strike (for a 50 km wide E-W band centered on the local locking maximum) using the Gaussian model from Schmalzle et al. (2014). The northern and southern segments have a ~25% increase in locking compared to central Cascadia. These geodetic models are non-unique, in part because of poor constraints offshore, but decreased locking in central Cascadia appears to be a robust feature. Current plate locking does not have to reflect the long-term state of plate coupling, however, the pattern of locking is consistent with patterns of long-term uplift rates and forearc topography.

Both shallower interface dip angles and increased plate locking correlate with regions of increased subslab buoyancy (Figure 4a) and increased uplift in the forearc (Figure 2a-c). In Sec. 3.5 we explore how these variations can influence forces along the megathrust interface and in the forearc.

3.5 Mechanics of the Forearc

The long-term mechanics of the subduction zone forearc can be expressed in terms of the total shear force along the megathrust interface and opposing gravitational forces at the interface, which promote stretching and collapse of the forearc (Figure 5; Dahlen, 1990; Wang & He, 1999). Here, we present a quasi-static 2D along-dip model of the forearc which we will use to relate subslab buoyancy to topography (Figure 5), assuming steady state topography so that erosion does not influence the force balance as

has been proposed for connections between glaciations and deep melt generation in volcanic regions (e.g., Huybers and Langmuir, 2009).



- | | |
|--|--|
| F: Gravitational stretching force | α: Topographic relief angle |
| F_0: Total shear force | β: Slab dip angle |
| $\Delta\rho$: density difference between crust and structure left of the wedge | b: Forearc topography |
| g: acceleration due to gravity | W: Width of plate coupling |
| μ': Effective coefficient of friction | d: Depth limit of coupling |

Figure 5: Schematic model illustrating the force balance between gravitational forces promoting the stretching/collapse of the forearc wedge and the resistive shear forces along the megathrust interface. For Cascadia $F \approx F_0$.

Following Wang & He, (1999), we define the trenchward stretching force, F , and the total shear force along the megathrust interface, F_0 . The stretching force (F) arises due to topographic relief in the forearc being laterally unconstrained, resulting in deviatoric horizontal tension in the lower part of the plate. It is defined as:

$$F = \frac{\Delta\rho g b^2 \sin(\alpha + \beta)}{2 \sin(\alpha)} \quad (1)$$

where $\Delta\rho$ is the density contrast between the forearc and either water or air, g is acceleration due to gravity, b is the height above the incoming or undeformed oceanic plate, α is the angle of the topographic relief with respect to the incoming oceanic plate, and β is the interface dip angle (Figure 5).

The total shear force along the megathrust interface is due to frictional coupling of the plates. It is defined as:

$$F_0 = \frac{1}{2} \mu' W d \rho g \quad (2)$$

Where μ' is the effective coefficient of friction, ρ is the density of forearc wedge, W is the downdip width of the coupled region, and we assume the plates become uncoupled at critical depth, d , perhaps dependent on the thermal structure (Hyndman & Wang, 1995). Plate coupling is defined using a static friction law $\tau = \mu' \sigma_n$, where τ is the shear stress and σ_n is the normal stress. The effective coefficient of friction μ' contains contributions from the static coefficient of friction, pore pressure effects from fluids, and any other conditions that may influence the observed shear stress. This describes a long-term interaction along the interface as opposed to the short-term plate locking condition, the latter of which may change between or during seismic cycles. The width of the coupled region can be defined as a function of the coupling depth limit d and interface dip β , such that $W = \frac{d}{\sin(\alpha) + \sin(\beta)}$. Thus, a decrease in interface dip increases the coupled width and the total shear force can be rewritten as,

$$F_0 = \frac{\mu' d^2}{2(\sin(\alpha) + \sin(\beta))} \rho g \quad (3)$$

Here, the magnitude of F_0 depends on both the interface dip angle (modulating the coupled width, W) and plate coupling (via the effective coefficient of friction, μ'). The

total shear force at the megathrust interface increases due to shallowing the interface dip angle or increasing plate coupling (Figure S5).

We can link forearc topography to the total shear force by relating equations (1) and (3).

For Cascadia $F \approx F_0$ (Wang & He, 1999). Thus:

$$\frac{\Delta\rho g b^2 \sin(\alpha + \beta)}{2 \sin(\alpha)} \approx F_0 = \frac{\mu' d^2}{2(\sin(\alpha) + \sin(\beta))} \rho g \quad (4)$$

This describes a forearc dynamically supported by the long-term shear forces at the interface. Using reference values of $\alpha = 1.5^\circ$, $\beta = 11.5^\circ$ (average dip angle in central Cascadia), and $b = 4 \text{ km}$ (measured from the top of the oceanic crust; accounts for ~1km thick sediment layer), we estimate a 25% increase in the resistive shear force is needed to support a 1 km increase in forearc topography (Figure S5). Using reference value $\mu' = 0.03$ (Wang & He, 1999), we estimate that a 1 km increase in forearc topography requires a 2° shallowing of the slab dip or a 33% increase in the effective coefficient of friction, and thus plate coupling (Figure S5).

4.0 Discussion

We propose that buoyant anomalies in the subslab region locally increase the total shear force along the megathrust through a combination of decreased average dip angle of the shallow subduction interface and/or increased plate coupling (Figure 6). These factors influence short-term processes such as where interseismic uplift and plate locking occur. In the long-term, because interseismic uplift is related to long-term uplift patterns, total shear force variations affect where excess topography is most likely to develop. Thus, subslab properties influence along-strike variations in forearc vertical motion

through time. Further, we suggest that along-strike changes in the total shear force acting on the thrust interface support the variable topography in the forearc.

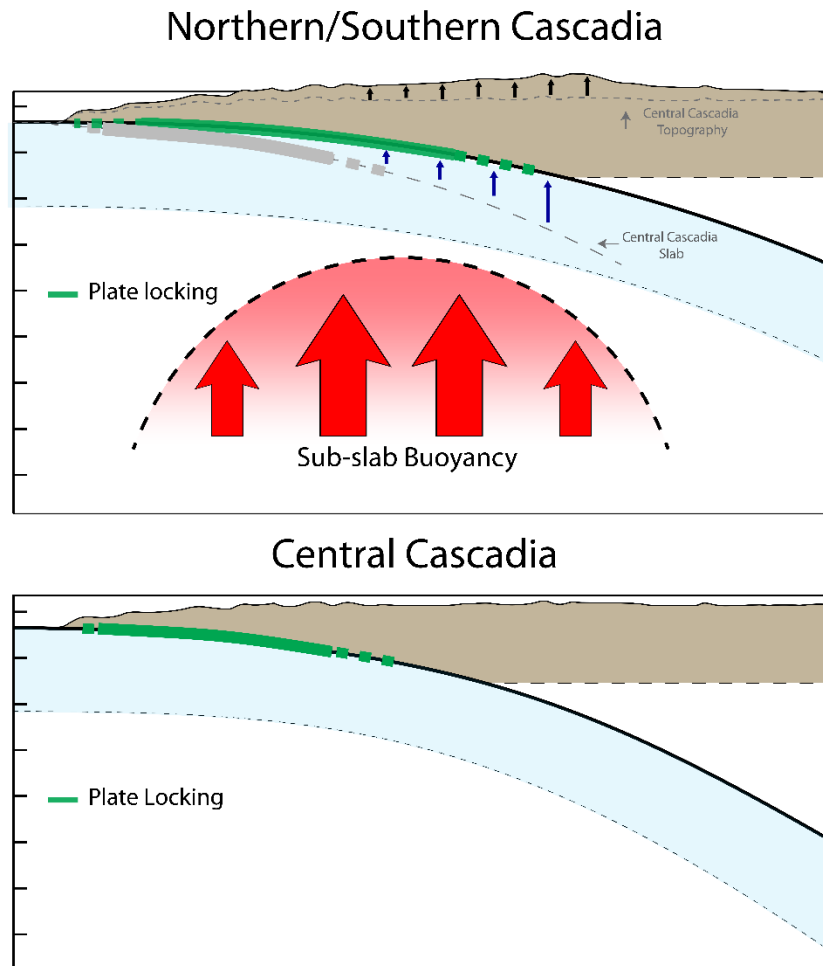


Figure 6: Conceptual model for the Cascadia subduction zone. In northern and southern Cascadia subslab buoyancy influences the overlying megathrust by changing the slab morphology (shallowing the dip) and increasing the degree of plate coupling. This leads to preferential growth of topography in these regions and provides support for the high standing topography that is present. In central Cascadia, where subslab buoyancy is absent, slab dips are steeper and coupling is reduced leading to reduced topographic development and supported topography.

4.1 Influence of Subslab Buoyancy on the Megathrust Interface

Along-strike variations in subslab buoyancy could impact slab morphology, locally shallowing the slab in regions overlaying buoyant anomalies. This notion is similar to the morphology of subducting slabs being dependent on their density structure, with more buoyant (younger) slabs tending towards flat subduction (Royden & Husson, 2009). The age of the JdF slab varies by <4Ma beneath the forearc (Wilson, 2002; Figure 3), thus the expected density variation of the slab is low. However, the young age of the slab (~10 Ma), and corresponding low elastic thickness ($T_e \approx 8.5$ km with a flexural wavelength ≈ 1 km), make it more susceptible to morphologic changes due to insignificant flexural response. Geodynamic models have shown that introducing buoyant material into a subduction zone impacts the dynamics, locally shallowing slab dip angles, advancing the subducting trench, and modifying the strike of the subduction zone (Betts et al., 2012). Observations of decreased slab dip in northern and southern Cascadia (Figure 4) are consistent with an upward directed force acting on the slab from below, working in opposition to forces associated with crustal loading and slab pull.

We postulate that excess subslab buoyancy may also change the state of stress at the megathrust interface, locally increasing plate coupling above buoyant regions. Plate coupling can be increased in two ways, either by increasing the normal stress or increasing the effective coefficient of static friction μ' . Increases in normal stress could arise if the flexural rigidity of the overlaying crust is large enough to oppose buoyancy forces from below, raising the normal stress above lithostatic conditions. Increases in the coefficient of friction could arise from several factors, as μ' contains parameters that model cohesion, pore fluid pressure, and the true coefficient of friction, all of which are poorly constrained. While, the exact mechanism by which plate coupling could increase

is unclear, there is evidence that buoyancy variations influence stress on the interface. Slab buoyancy variations due to thermal age have been linked to earthquake size distributions, with more buoyant (younger) slabs linked to larger earthquakes (Nishikawa & Ide, 2014; Scholz, 2015), which in turn have been linked to fault stress, with larger events corresponding to increased stress (Scholz, 2015; Spada et al., 2013). Assuming that the pattern of current plate locking reflects the long-term trends (see Sec. 4.2), observations of increased plate locking above regions of subslab buoyancy (Figure 4) are consistent with buoyancy-modulated plate coupling.

4.2 Forearc Uplift

We hypothesize that heterogeneity beneath the subducting slab influences where topographic development is most likely to occur within the forearc (Figure 6). This occurs because subslab buoyancy laterally modulates the long-term total shear force on the interface by shallowing slab dip and/or increasing plate coupling (see Sec. 4.1). The current state of plate locking need not reflect the long-term trends; in Cascadia, however, they appear to be consistent over many seismic cycles (Figure 2, 4; Sec. 3.1), indicating a stable relationship. We observe increased plate locking in the northern and southern segments where we infer an increase in total shear force due to subslab buoyancy. Thus, we suggest that subslab buoyancy influences the pattern of interseismic plate locking for any given seismic cycle.

The distribution and strength of plate locking is a first order control on interseismic deformation (Li et al., 2018; Schmalzle et al., 2014). For Cascadia, the pattern of long-term vertical uplift in the forearc appears to be related to this pattern of interseismic vertical deformation (Figure 2), however, the values are an order of

magnitude lower. This suggests that some fraction of interseismic strain is unrecovered during the seismic cycle and is instead converted into permanent deformation (Kelsey et al., 1994). If consistent over many seismic cycles, this leads to topographic development. This mechanism has been proposed to explain forearc highs globally (Bassett & Watts, 2015). In this scenario then, subslab buoyancy influences where topography develops by locally increasing the degree of plate locking over many seismic cycles, thus progressively and selectively building up unrecovered interseismic strain in those regions.

4.3 Support of High Forearc Topography

Topographic highs in the forearc, once emplaced, must be supported or else gravitational forces in the crustal column will promote relaxation. We have shown that for Cascadia, isostatic forces alone cannot adequately explain the topographic variation (see Sec. 3.2). Instead, we infer that subslab buoyancy alters the slab dip angle and/or plate coupling along the interface, which locally increases the total shear force that opposes stretching and collapse of the forearc, thus allowing for higher forearc topography (see Sec. 3.5).

To investigate this, we use plate coupling and slab dip angle as variable inputs in Eq. 4 in order to estimate along-strike variations in forearc topography (Figure 7). We start by examining the effect of slab dip angle and plate coupling individually, although we suspect that the two may be coupled. First, plate coupling is held constant (by setting $\mu' = 0.03$) and slab dip is allowed to vary along strike with values according to Figure 4b (green line Figure 7). Next slab dip is held constant ($\beta = 11.5^\circ$) and the plate coupling is varied. Because we do not know the distribution and magnitude of long-term plate

coupling we use the inferred plate locking as a proxy. To do this we multiply the averaged plate locking fraction (Figure 4c) by a factor of 0.058 and equate it to the effective coefficient of friction μ' (purple line Figure 7). This is done so that the average plate locking value (54%) yields $\mu' = 0.03$.

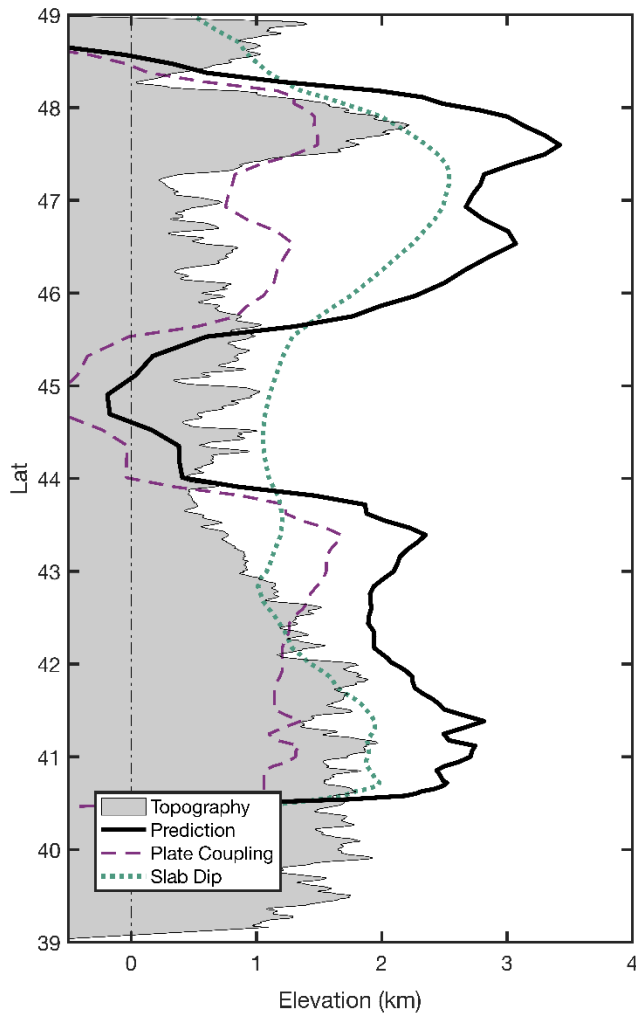


Figure 7: Predicted topography assuming support comes from the resistive shear force at the megathrust interface. Black line represents the predicted topography using along-strike slab dip angle and plate locking variations as variable inputs. Grey region is the observed maximum topography in the defined swath (Figure 1). Green line represents the predicted topography only due to variations in slab dip angle. Purple line represents the predicted topography only due to variations in plate locking.

Allowing both slab dip angle and plate coupling to vary we predict higher topography in the northern and southern segments, with local maximums collocated with

observed local maximums in forearc topography (black line Figure 7). This calculation is presented as a proof of concept rather than a precise estimate as several important details are not considered such as the geology of the forearc, the relationship between plate coupling and plate locking, and isostatic contributions. This may explain discrepancies such as the overestimation of topography in the north and south, underestimation of topography in central Cascadia, and differences in the wavelength of topographic features. However, the ability of this model to predict first-order variations along-strike suggests that it is a viable mechanism.

5.0 Conclusion

The topography of the Cascadia forearc is spatially correlated with several independent observations. Regions of high topography in the north and south correspond with increased interseismic uplift rates, increased coseismic subsidence, increased long-term uplift rates, increased erosion rates, low-velocity anomalies in the subslab region, increased inferred subslab buoyancy, shallower slab dip angles, and increased plate locking. We suggest that buoyancy forces arising from subslab heterogeneity modulate the total shear force on the megathrust interface by shallowing the slab dip and/or increasing plate coupling. In this way, subslab buoyancy influences where topographic development is most likely to occur and provides dynamic lateral support for current topographic variations.

6.0 Bridge

Chapters III & IV focused on my P-wave tomography model for the Cascadia subduction zone, using it to investigate how the subslab mantle influences megathrust behavior and forearc development. These chapters focus on big picture, process-oriented questions regarding subduction dynamics. In Chapter V, I focus on the onshore-offshore methodology, using synthetic modeling to investigate how changes in elevation and crustal structure across the margin influence delay times. Several methodologies to account for this structure are evaluated, identifying potential artifacts and pitfalls. I apply these methods to the real data set for further comparison. Finally, I present a new S-wave delay timed dataset for the Cascadia subduction zone.

CHAPTER V

ONSHORE-OFFSHORE BODY WAVE TOMOGRAPHY OF THE CASCADIA SUBDUCTION ZONE AND JUAN DE FUCA PLATE SYSTEM: IDENTIFYING CHALLENGES AND SOLUTIONS FOR SHORE-CROSSING DATA

1.0 Introduction

Subduction zones are critical to the plate tectonic system as regions where oceanic lithosphere is recycled into the mantle, the largest earthquakes and tsunamis are generated, continental crust is built through accretion and arc magmatism, and volatiles are circulated (Stern, 2002). For these reasons, subduction zones worldwide have been studied extensively with seismic methods producing images of convergent margin structure, characterizing and cataloging regional seismicity, and developing hazard assessments. Fundamentally, subduction processes are dependent upon properties of both the incoming oceanic lithosphere and the overriding plate. Most seismic datasets are inherently limited, however, comprised of only land-based instruments and lacking comparable data from the offshore oceanic plate. Those studies capable of obtaining coincident, shore crossing data are often limited in their spatial scope (e.g. Parsons et al., 2005; Trehu et al., 1994). Only recently, through experiments such as the community driven Cascadia Initiative (CI), are we able to collect dense, amphibious seismic data spanning large portions of a subduction margin (Toomey et al., 2014).

Amphibious arrays (onshore-offshore) offer significant advances to our understanding of subduction zone mantle structure but also introduce complications due to the compositional and structural differences between oceanic and continental

lithosphere. This is especially problematic for teleseismic body wave tomography targeting the mantle, which is poorly equipped to resolve heterogeneity in near-surface structure (<50 km from the surface). Variations in crustal thickness, elevation, and sedimentation result in contributions to seismic travel times, which can obfuscate the underlying mantle structure. Further, the innate large changes in structure of subduction zones challenges some of the assumptions commonly made in body wave tomography such as the validity 1D seismic rays. The geometry of teleseismic raypaths can be altered by velocity variations in the structures they traverse, especially if features are sub-vertical, such as a subducting slab. Addressing these complexities is imperative to the accurate interpretation of seismic images.

We focus our efforts on the Cascadia subduction zone (CSZ) where seismic deployments span the entirety of the relatively short margin (~1200 km) and span the entire offshore oceanic plate system (the Juan de Fuca). Onshore instrumentation is largely provided by the IRIS Transportable Array (2003; TA), which deployed seismometers across the US at a ~50 km spacing, starting in 2007 and progressing eastward. Several mantle imaging studies were produced using these datasets (e.g. [Becker, 2012](#); [Lin & Schmandt, 2014](#); [Schmandt & Humphreys, 2010](#)), resolving the subducting slab structure, slab fragmentation processes, and continental mantle structure. From 2011-15, ocean bottom seismometers were deployed on the Juan de Fuca plate system offshore, with permanent stations and TA redeployments tying it to the existing data. Several studies have imaged the offshore structures in the mantle ([Bell et al., 2016](#); [Bodmer et al., 2015](#); [Byrnes et al., 2017](#)), noting significant heterogeneity in the isotropic and anisotropic oceanic mantle structure.

A key takeaway from early CI studies is that characterizing the oceanic structure is critical to understanding subduction dynamics, yet, few studies have inverted for joint onshore-offshore structure (Bodmer et al., 2018; Gao, 2018; Hawley et al., 2016). Studies of teleseismic P-wave velocity structure vary significantly in both methodology and interpretation. Hawley et al. (2016) image a margin-wide low-velocity anomaly beneath the subducting slab and primarily use static station corrections to account for changes in near-surface structure. Conversely, Bodmer et al. (2018) image localized low-velocities beneath the slab in the north and south and use a priori starting models which include elevation, to account for near-surface structure. Understanding how these methodology choices influence the tomographic results is important because there is pronounced variability in along-strike subduction behavior (e.g. plate locking, tremor density, long-term uplift rates) and it is still unclear exactly what influence the oceanic mantle may have on these processes (e.g. Bodmer et al., in review).

Here, we investigate P and S mantle velocity structure of the Cascadia subduction zone (CSZ) using amphibious broadband data. Through a series of synthetic tests, we explore the impact of near-surface structure on observed delay times and the resulting tomographic inversions. We develop a strategy to account for near-surface structure and apply it to the CSZ dataset. We present a new S-wave delay time data for the subduction zone and define a path for future study.

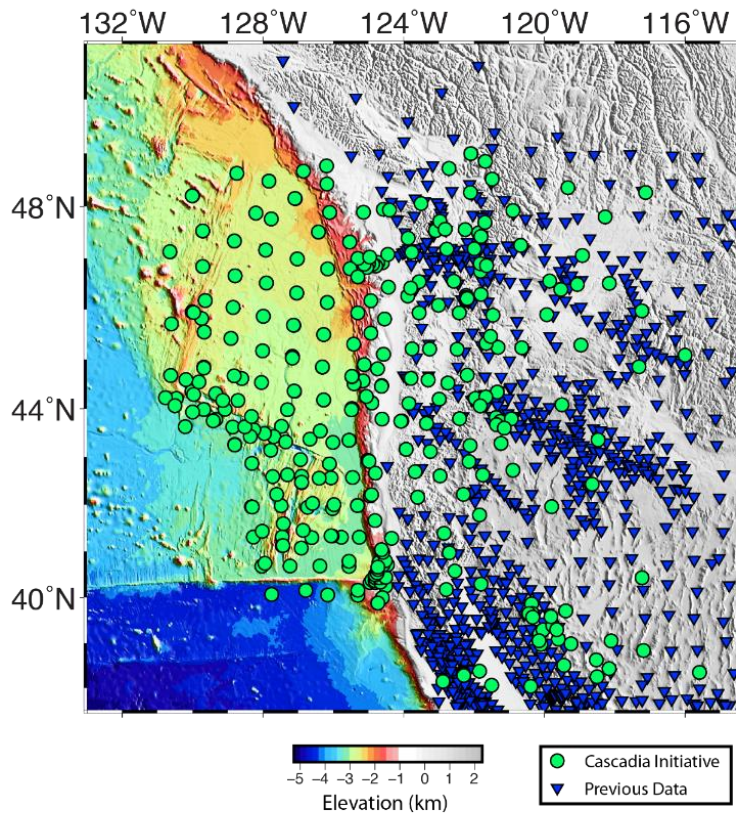


Figure 1: Map of the Cascadia subduction zone colored by elevation. Green dots represent Cascadia Initiative and coincident stations. Blue triangles represent legacy data from Schmandt & Humphreys (2010).

2.0 Tectonic Setting

Our study focuses on the Cascadia subduction zone (CSZ), the convergent margin off the western United States, including the entirety of the incoming Juan de Fuca (JdF) oceanic plate system (Figure 1). Western North America has been assembled over the last several hundred million years through the accretion of oceanic terrains (DeCelles, 2004), continuous arc volcanism, and large flood basalt events (Hooper et al., 2002). During late Cretaceous it is widely believed that the Farallon slab was undergoing flat slab subduction. Coinciding with the accretion of the large oceanic terrain Siletzia at ~50 Ma subduction jumped westward and initiated at the present Cascadia margin (Schmandt &

Humphreys, 2011; Wells et al., 1984) leaving behind the Idaho slab curtain. At ~17 Ma the Columbia River and Steens flood basalts were deposited, which many researchers attribute to the arrival of the Yellowstone plume (Camp, 2015; Obrebski et al., 2010; Pierce & Morgan, 1992; Schmandt et al., 2012). It is still debated what impact such a plume would have during an interaction with the subducting slab structure.

Though the margin is relatively short (~1200 km), significant variations exist along-strike in megathrust behavior (Brudzinski & Allen, 2007; McCrory et al., 2012; Schmalzle et al., 2014; Wells et al., 2017), forearc kinematics and structure (Burgette et al., 2009; Kelsey et al., 1994; Leonard et al., 2010; Schmalzle et al., 2014; Bodmer, In Review), and mantle structure (Bodmer et al., 2018; Chen et al., 2015). The underlying mechanisms giving rise to this segmentation, however, are still debated. Many studies focus on properties of the overriding crust, incoming oceanic crust, or properties along the plate interface to explain along-strike segmentation (Audet et al., 2009; Brudzinski & Allen, 2007; Cloos, 1992; Delph et al., 2018; Littel et al., 2018; Ruff, 1989). However, there is evidence that heterogeneity within the oceanic mantle plays an important role in subduction phenomenon (Bodmer et al., 2018). Nearby hotspots and/or local flow dynamics may emplace anomalously buoyant mantle beneath the subducting slab (Bodmer et al., 2018; Portner et al., 2017). This provides an upward directed buoyancy force which can modulate slab morphology and plate coupling, influencing the forces along the interface (Bodmer et al., in review).

The present day JdF plate is a young, hot, and relatively small, a consequence of millions of years of continuous ancient Farallon plate subduction. The current rate of convergence at the margin is ~40 mm/yr. As the Farallon plate was consumed it

fragmented into successively smaller plates (Stock & Lee, 1994) and new triple junctions were created. At the southern edge of the CSZ lies the Mendocino triple junction (MTJ), currently migrating northward at a rate of 40 mm/yr (Atwater, 1970; Furlong & Schwartz, 2004), marking the northern extent of the San Andreas fault. Two 1st order ridge segments define the western boundary of the Jdf plate, the JdF ridge to the north and the Gorda ridge to the south. The ridge system is currently migrating to the NW at a rate of 25 mm/yr (Small & Danyushevsky, 2003) and has recently undergone a clockwise rotation and reorganization in the last 7 My (Riddihough, 1984). During this time the relatively young Blanco transform formed (Atwater & Stock, 1998) and the Explorer microplate detached (~4 Ma).

The southernmost section of the JdF plate is the Gorda deformation zone (Wilson, 1989). This region is typified by diffuse plate deformation, which can be seen in the bending of magnetic anomalies, pervasive left-lateral strike-slip faulting, and abundant shallow seismicity (Chaytor et al., 2004; Wilson, 1986). Spreading rates at the Gorda ridge decrease southward from 55 mm/yr in northern Gorda to 23 mm/yr near the Mendocino transform (Riddihough, 1980). Orientation the Mendocino transform is rotated CCW from Pacific/JdF relative plate motion by ~20°. The cause of this deformation has been linked to the Pacific plate's evolving influence on the local stress field, with the Gorda undergoing N-S compression, facilitating internal deformation (Chaytor et al., 2004; Wada et al., 2010).

Previous mantle tomography studies of the western US consistently image a dipping high-velocity feature, interpreted as the JdF slab subducting into a relatively low-velocity upper mantle (Becker, 2012). Schmandt & Humphreys (2010a) trace the slab to

a depth of 350 km, in the southern section, accounting for 15 Ma of subduction. A robust feature in these studies are large amplitude variations in the slab along strike at depths below ~150 km referred to as the “slab hole” (Roth et al., 2008) where high-velocity anomalies decrease significantly beneath Oregon. Some have attributed this to a slab plume interaction (Obrebski et al., 2010) while others have suggested that it is an imaging artifact (Roth et al., 2008). If the slab is nonexistent in this region, that has implications for models relying on slab rollback to drive advection as it will affect patterns of toroidal flow (Long, 2016). Near the mantle transition zone many researchers image independent high velocities interpreted as older fragmented sections of the Farallon plate (e.g. Obrebski et al., 2010; Schmandt & Humphreys, 2010b; Sigloch et al., 2008).

3.0 Body Wave Delay Time Data

3.1. Data and Methods

Our study combines P- and S-wave delay time measurements from recent onshore-offshore experiments with previously reported teleseismic delay time data from onshore studies. Legacy onshore delay-time data comes from Schmandt & Humphreys (2010a), which has been used in several follow-up studies (Schmandt et al., 2012; Schmandt & Humphreys, 2011; Schmandt & Lin, 2014). We use a subset of their data that covers the geographic area of interest (see Figure 1). The relative delay-time dataset contains multiple phases (P, PKP, S, and SKS) and frequency bands. The Schmandt & Humphreys data provides 69,907 P-wave delay times (48%, 29%, 22%, and 1% at 1, 0.5, 0.3, and 0.1 Hz center frequency, respectively) and 22,357 S-wave delay times (43%,

55%, and 2% at 0.05, 0.1, and 0.4 Hz center frequency, respectively); for additional details see Sec. 2 of [Schmandt & Humphreys \(2010a\)](#).

Shore-crossing delay times used for this study come from the 4-year-long CI community experiment ([Toomey et al., 2014](#)), and separate year-long studies of the Blanco transform and the Gorda region. The CI amphibious array comprised 27 onshore and 258 ocean bottom seismometers (OBS) that were deployed in ~10-month-long intervals (~40 OBS/yr), allowing them to span the entirety of the JdF plate system, including the JdF Ridge, Gorda Ridge, Blanco transform, Gorda deformation zone, and the Cascadia subduction zone ([Figure 1](#)). The Blanco and Gorda experiments occurred coincident with the CI and provide an additional 30 and 24 OBSs, respectively.

Reoccupation of onshore and offshore sites, as well as several permanent stations, tie the data sets together. The shore-crossing P-wave dataset was presented in [Bodmer et al. \(2018\)](#). In this study we present a newly measured S-wave delay time dataset.

We processed CI waveform data as follows. Instrument response was deconvolved following the method of [Haney et al. \(2012\)](#) and a third-order Butterworth filter (corner frequencies of 0.0303 and 0.0833 Hz) was applied prior to measurement of delay times using cross-correlation ([VanDecar & Crosson, 1990](#)). Because the errors reported by the cross-correlation method are unrealistically small (see supporting information of [Byrnes et al., 2017](#)), the minimum uncertainty for all measurements was set to 0.25 s. [Figure 2](#) shows examples of aligned waveforms for two events that include data from both onshore and offshore sites.

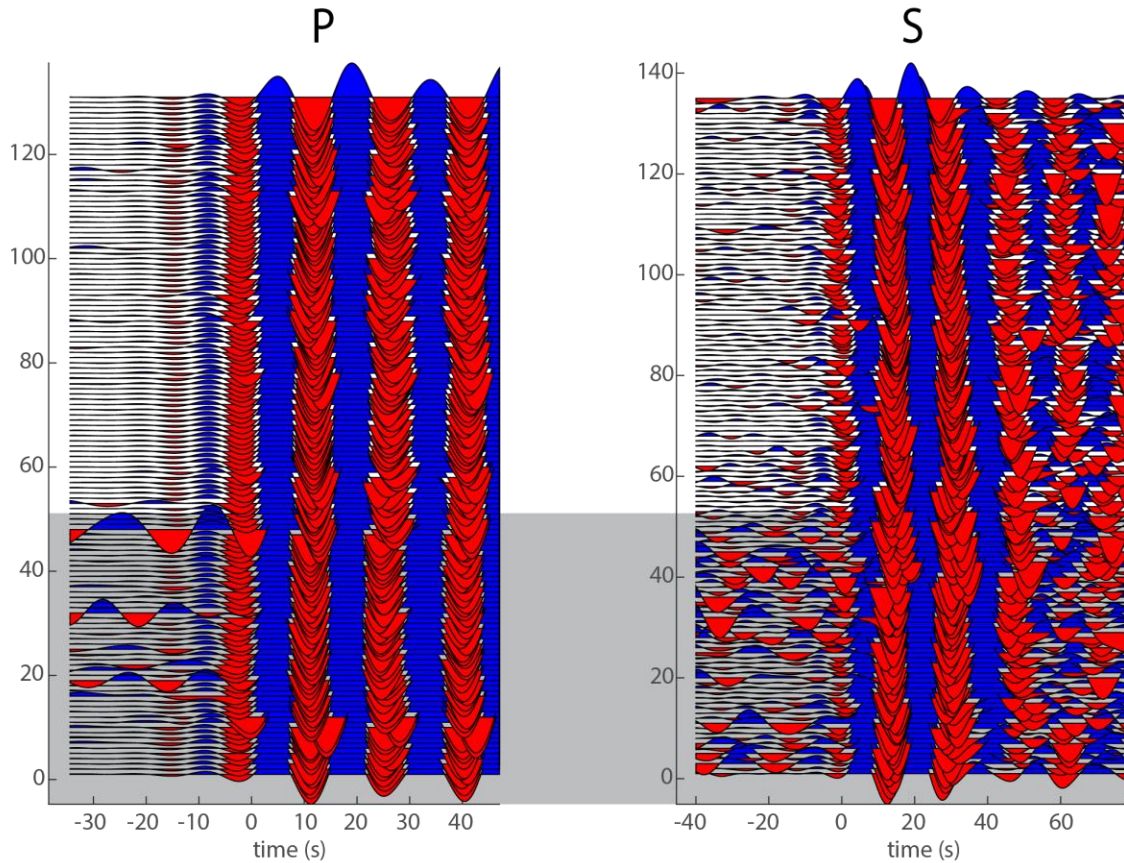


Figure 2: Example teleseismic waveforms for P- and S-waves. Waveforms are aligned on the predicted arrival time from a 1D model. Grey box highlights ocean bottom seismometer stations. Magnitude 6.9 event: 2015-07-18 02:27:33.

Several quality control criteria were adopted in order to remove stations and events considered to be outliers. We calculate average station-delay times for each receiver, correcting the arrivals for perturbations due to near surface structure, derived from our preferred starting model (see Sec. 6.2). Average station-delay times are most sensitive to structure near the receiver, thus if near surface structure is properly removed the average station-delay should tend towards zero. We remove stations with average delay times that exceed a standard deviation of 2.5σ for the entire dataset (P and S treated separately). These stations are either highly anomalous compared to the rest of the array or our preferred starting model does a poor job of accounting for the local near surface

structure; regardless we consider them erroneous. We also remove stations whose individual arrivals exceed a standard deviation of 1s (1.5s) for P (S) phases. These thresholds are larger than the standard deviations for the entire set of arrivals, 0.4 s and 1.1 s for P and S phases respectively. Finally, we subjectively remove offshore stations that display variations in average station-delay times over subsequent redeployments in the same location (Byrnes et al., 2017) or differ significantly from nearby stations.

Altogether, our analysis uses 105,039 teleseismic P-wave delay times from 1,663 events recorded at 1,077 stations (34,794 arrivals from CI) and 62,505 teleseismic S-wave delay times from 805 events recorded at 951 stations (39,740 arrivals from CI).

Figure 3 shows the distribution of teleseismic events, with the highest contributions from the Japan, South America, and Tonga regions.

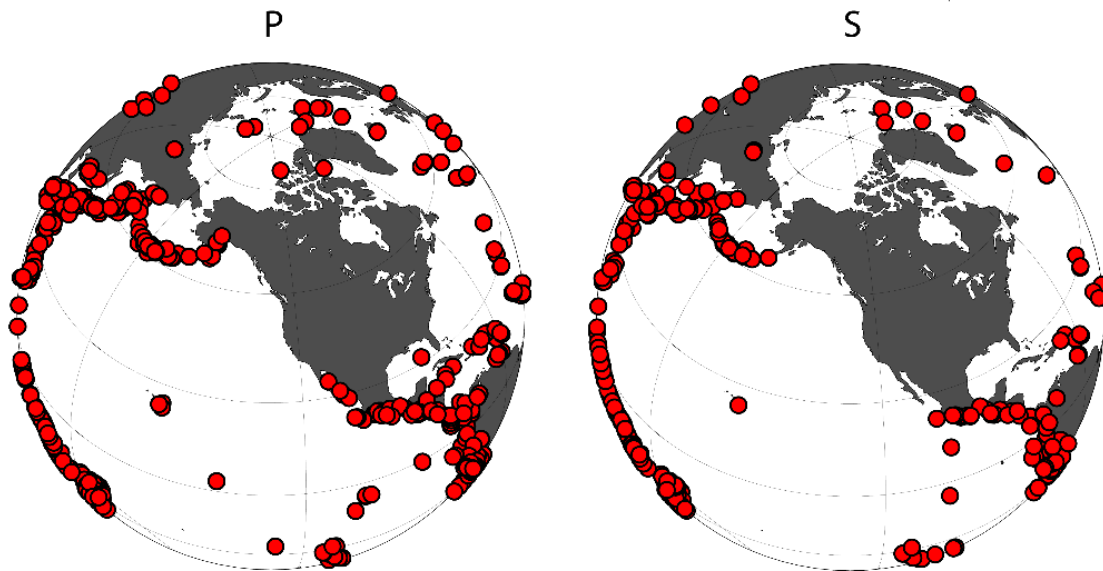


Figure 3: Event distribution for P and S events in the dataset.

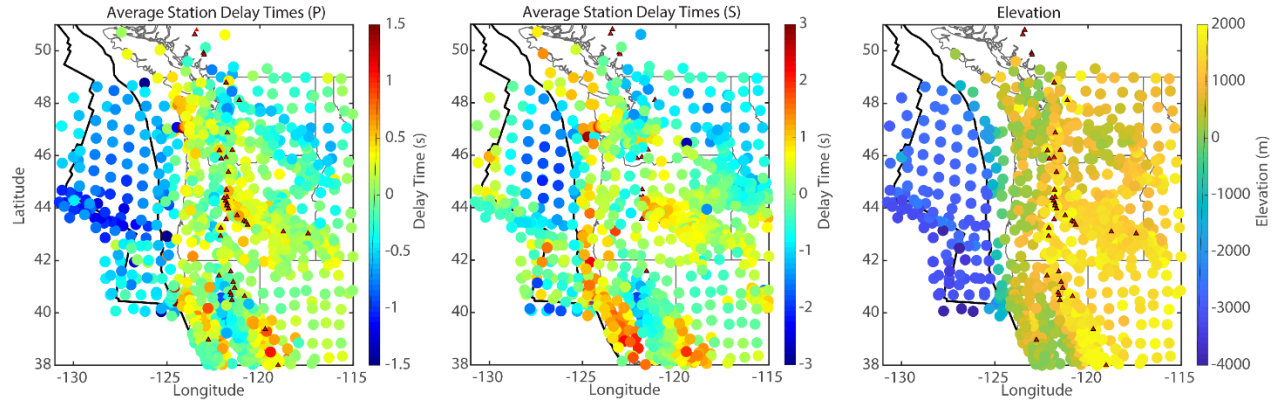


Figure 4: Average station delay times for P (Left) and S (Center) arrivals. No corrections have been applied to the data and quality control criteria are not yet applied. (Right) Elevation of each seismic station.

3.2. Observed Delay Times and Trends

The root mean square (RMS) of all delay times is 0.42 s for P and 1.12 s for S, with distributions skewed toward advanced arrivals (Figure 4); the peak-to-peak variation of the entire data set is -2.6 s to 2.9 s for P and -5.5 s to 4.9 s for S. Figure 4a-b shows the average delay time observed at each station. The peak-to-peak variation in station-averaged delay times is -2.2 s to 1.9 s for P and -2.8 s to +2.9 s for S. Station-averaged delay times show a clear onshore-offshore signal that correlates well with elevation (Figure 4c). We attribute this first-order signal to both changes in elevation and to the transition from oceanic to continental crust (see Sec. 5.1).

In addition to the substantial onshore-offshore trend in station-averaged delays, there are several other regional-scale trends (Figure 4a-b). For example, a north-south band of advanced delay times is observed in the region just west of the Cascade volcanic arc. Advanced delay times are also observed trending northeast-southwest in Washington and broadening in western Idaho. Regions of slower arrivals include central Oregon east of the Cascades, Northern California near the slab edge (Beudoin et al., 1998), and in the forearc along the coast. Offshore, the earliest arrival times are observed along the

Blanco Transform for P arrivals and in the center of the JdF plate for S arrivals.

Variations between regions like the JdF ridge and plate interior are much more pronounced in the S wave data. Average delays become less advanced along the JdF Ridge, east of the CSZ frontal wedge, and throughout the Gorda region.

4.0 Tomographic Method

Our tomographic method is well-suited for amphibious data because it treats the forward problem accurately and explicitly includes prior states of knowledge, including uncertainties (e.g., [Jackson, 1979](#); [Tarantola & Valette, 1982](#)). Simple examples of prior states of knowledge are elevation and regional-scale variations in crustal thickness associated with the ocean-continent transition. Detailed statements of prior knowledge, such as independent velocity models for example, can be used for hypothesis testing. Our philosophy is that seismic data do not provide unique tomographic results; consequently, there are advantages to testing observations against assumed models. In practice, this means that the user defines a state of information by choosing a prior model — including its uncertainty — and by choosing subjectively the values of inversion parameters that control regularization. The following discussion emphasizes aspects of our workflow that distinguish it from algorithms commonly used for teleseismic delay-time tomography: (1) the ability to define complex, three-dimensional starting models, (2) iterative, three-dimensional seismic ray tracing, and (3) a flexible scheme for regularizing inversions. Further details of our methods are presented elsewhere ([Bezada et al., 2013](#); [Byrnes et al., 2017](#); [Hammond & Toomey, 2003](#); [Schmandt & Humphreys, 2010b](#); [Toomey et al., 1994](#)).

The forward problem is parametrized in terms of slowness defined on a grid of nodes, which are sheared vertically to account for elevation (Toomey et al., 1994). Nodes may be defined at regular intervals of any length to adapt to model complexity, though in practice computational expense limits nodal spacing. Seismic ray tracing is performed in two parts: (1) Within the domain of the tomographic image where the model is three-dimensional, ray paths and travel times are calculated using Dijkstra’s algorithm (Dijkstra, 1959; Moser, 1991) and (2) outside the model domain where the structure is assumed to be radial, we used the tau-p method (Crotwell et al., 2011) with the AK135 1D velocity model (Kennett et al., 1995); see (Bezada et al., 2013) for details. The choice of a starting model directly influences the predicted ray paths and travel times. By using starting models that include known variations in elevation and near surface structure — such as regional-scale variations in crustal thickness — we can account for structure near the stations which is difficult to resolve with teleseismic body waves.

The inverse problem is solved by minimizing the prediction error, a penalty function applied to the Euclidean size of the model perturbation vector, and vertical and horizontal roughening operators applied to the slowness perturbational model (see Toomey et al., 1994 for details). The model perturbation vector includes slowness perturbations as well as event and station statics. Data and model covariance matrices are included in the inversion, which allow the user to enforce prior knowledge (e.g., Menke, 1985; Toomey et al., 1994). We use the “banana-doughnut” kernel approximation of Schmandt & Humphreys (2010b) to account for the frequency dependent sensitivity of delay times (Dahlen et al., 2000). Multiple iterations of the forward and inverse problem are performed, and model parameters are updated in either a jumping or creeping strategy

(Shaw & Orcutt, 1985). In practice, hundreds of non-linear tomographic inversions are conducted to test hypothetical models and to understand how inversion parameters and assumptions influence the results.

In this study, a 145 X 181 X 76 grid with 10 km nodal spacing is used for the forward calculations (centered about 125° W, 45° N). A 49 X 61 X 19 perturbational slowness model is nested within the forward model with 30 km horizontal spacing and a variable vertical spacing increasing from 30 to 60 km with depth. The fractional uncertainty of the model parameters decreases with depth below 300 km to prevent accumulation of anomalies. Final model weights for the penalty, vertical smoothness, horizontal smoothness, and station static damping are chosen through multiple inversions of real and synthetic data evaluating the data misfit and model recovery (For details of model parameterization see Toomey et al., 1994).

5.0 Synthetic Studies of Amphibious Data

Here we present results of forward and inverse modeling of synthetic data that illustrate the effects of near-surface structure (<50 km depth) on amphibious teleseismic delay times and tomographic imaging. We first estimate contributions from elevation, crustal thickness, and local geology by predicting delay times for two shore-crossing P-wave refraction profiles (Sec. 5.1). We then test the influence of shallow structure on tomographic inversions by inverting synthetic delay times predicted for a model that includes shallow structure and a subducting slab. For these inversions, we explore different starting models of near-surface structure and methodologies used to account for structure, investigating their impact on the recovered images.

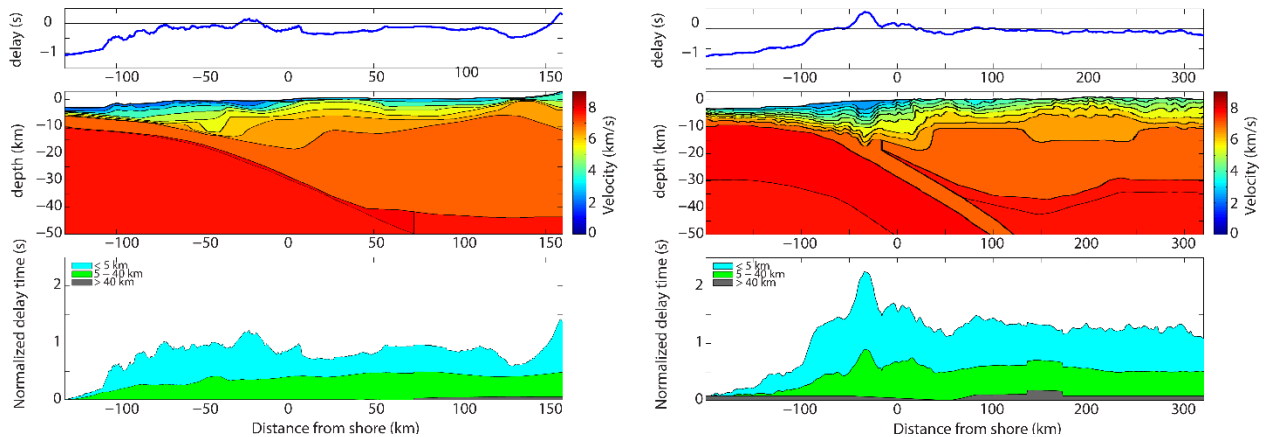


Figure 5: Synthetic delays predicted from 2D profiles; (Left) Trehu et al. (1994) at 44.5°N and (Right) Parsons et al. (2005) at 46.6°N. (Upper Panels) Predicted arrival times along profile relative to AK135 1D model predictions. (Middle Panels) Digitized reconstructions of the 2D velocity models. (Bottom Panels) Relative contributions to the total arrival time from structure 0-5 km depth (blue) and 5-40 km depth (green), Normalized by the minimum arrival time along profile.

5.1 Forward Modeling of Shore-Crossing Refraction Profiles

The results of two shore-crossing seismic refraction studies of the CSZ are used to quantify variations in P-wave delay-times due to shallow structure. Figure 5 shows results from Trehu et al. (1994) and Parsons et al. (2005) for refraction lines at 44.5°N and 46.5°N, respectively. In Figure 5, vertical travel times through the upper 50 km of each model are compared to predictions for a one-dimensional structure (AK135; Kennett et al., 1995). Each refraction model predicts about a 1 s difference in delay time between onshore and offshore regions. By comparison, the observed onshore-offshore difference of station-averaged delay times (P-waves) is ~0.6 s. Plotting the cumulative sum of vertical travel times (Figure 5) reveals that, to first approximation, half of the onshore-offshore signal is due to elevation (model depths <5km), while the other half is due to changes in crustal thickness (model depths 5-40 km). In addition, local fluctuations in excess of 0.5 s are observed in geologically distinct regions such as the continental shelf or volcanic arc.

These results show that structure in the upper 50 km contributes substantial signal to amphibious P-wave delay time data. It follows that prior models of elevation, crustal thickness, or crustal velocity can be used to predict and remove the near surface contribution to observed delay times. To illustrate this, we predict vertical delay times using only elevation data from each refraction profile, assuming isostasy to estimate crustal thickness and a simplified 2-layer crustal velocity structure (See [Figure S1](#)). For each refraction profile, the RMS misfit between these estimates and the results in [Figure 5](#) is about 0.3 s. If one assumes a model derived from elevation and isostasy alone, this misfit value would provide a conservative upper bound on the uncertainty of the model to predict near surface delay times (a proxy for the needed contribution from station statics). Good quality seismic results from prior studies can also be used to construct more accurate models of near surface structure. In addition, site-specific corrections can also be applied to the data; for example, when the offshore sediment thickness beneath a site is known ([Bell et al., 2016](#)). As the quality of a near-surface model or site-specific correction improves, the uncertainty attributed to station static terms can be reduced. In practice, the contributions due to local geology will not be well known at each site and station statics will be necessary. However, as shown in Sec. 5.2, limiting the contributions of station statics to a tomographic result is desirable.

5.2 Inverse Modeling of Synthetic Delay Times

To assess the impact of shallow structure on tomographic imaging, we calculated synthetic data for a 3D model of the CSZ that includes elevation, crustal thickness, and a subducting slab, and inverted these data assuming different prior models of near surface

structure. We find that results obtained using a detailed shallow starting model produce inversion results with less artifacts even though the data misfit is larger in comparison with other approaches.

5.2.1 Synthetic Delay Times

A generic 3D model of the CSZ was created by altering a flat-earth, 1D model to include elevation, crustal thickness, and a high-velocity, slab-like anomaly (Figure 6). The AK135 starting model (Kennett et al., 1995) has two near surface layers with P velocities of 5.8 km/s (0-20 km depth) and 6.5 km/s (20-35 km depth) and S velocities of 3.5 km/s (0-20 km depth) and 3.9 km/s (20-35 km depth). We vary the thickness of these layers to equal the distance between the surface elevation and the Moho depth estimated by CRUST1.0 (Laske et al., 2013), keeping the ratio of layer thicknesses constant. Vertical delay times are calculated through this model and these are used to determine slowness values on a regular 3D grid (10 km nodal spacing), so that the integrated times in the upper 50 km of each model are identical; this approach is necessary since the 10-km grid used for 3D ray tracing cannot exactly reproduce crustal thickness variations. Additionally, slowness perturbations representing the subducting Juan de Fuca slab are included, defined by a 50-km thick, high-velocity anomaly ($\Delta V_p=2\%$, $\Delta V_s=4\%$) extending to 410 km depth. The slab is defined by shallow and steeply dipping sections. The upper interface of the shallow section follows the inferred slab depths of McCrory et al. (2012) for depths of 50 to 100 km; below 100 km depth the slab dip is 50° .

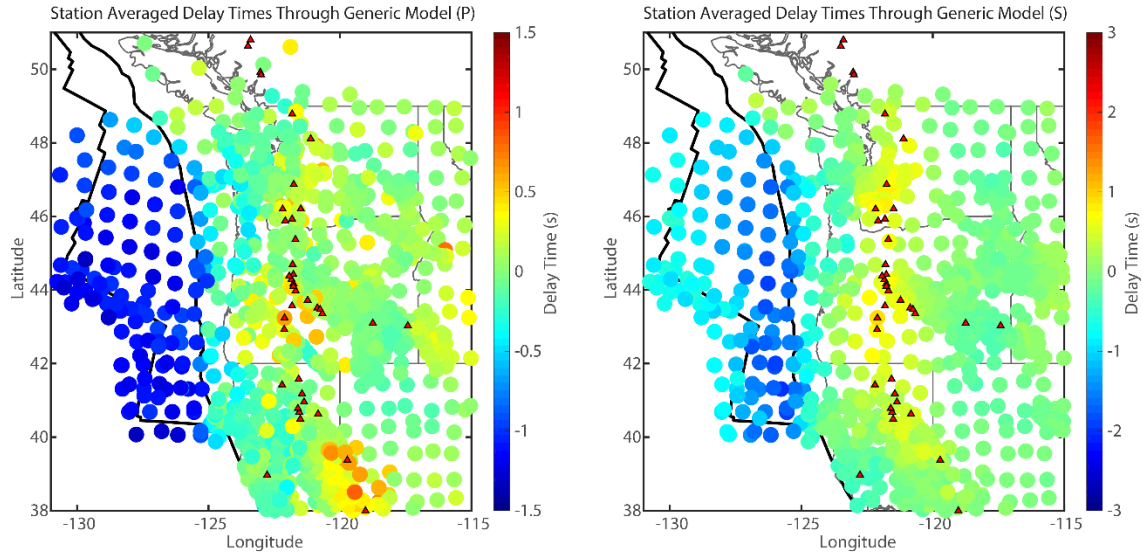


Figure 6: Station averaged delay times through the generic model of the Cascadia subduction zone for P (left) and S (right) data.

Figure 6 shows that station-averaged delay times through the shallow portion of the synthetic model have a clear onshore-offshore signal. The delay times were calculated using 3D ray tracing and the station/event distribution of the actual data. The histogram of all synthetic delay times is skewed towards advanced arrivals, with some P-wave arrivals as early as -1.5 s and S-wave arrivals as early as -2.5 s. The difference between the mean of onshore and offshore station-averaged delays is 1.3 s for P-waves and 1.9 s for S-waves, which is slightly larger than that predicted by the refraction profiles (Sec. 5.1). We note that these synthetic delays are not meant to reproduce the actual data; instead, they provide a test model that includes heterogeneity due to near surface structure and a primary mantle imaging target (i.e., the subducting slab). For all inversions presented below, Gaussian noise ($\sigma=0.25$ s) was added to the synthetic delays.

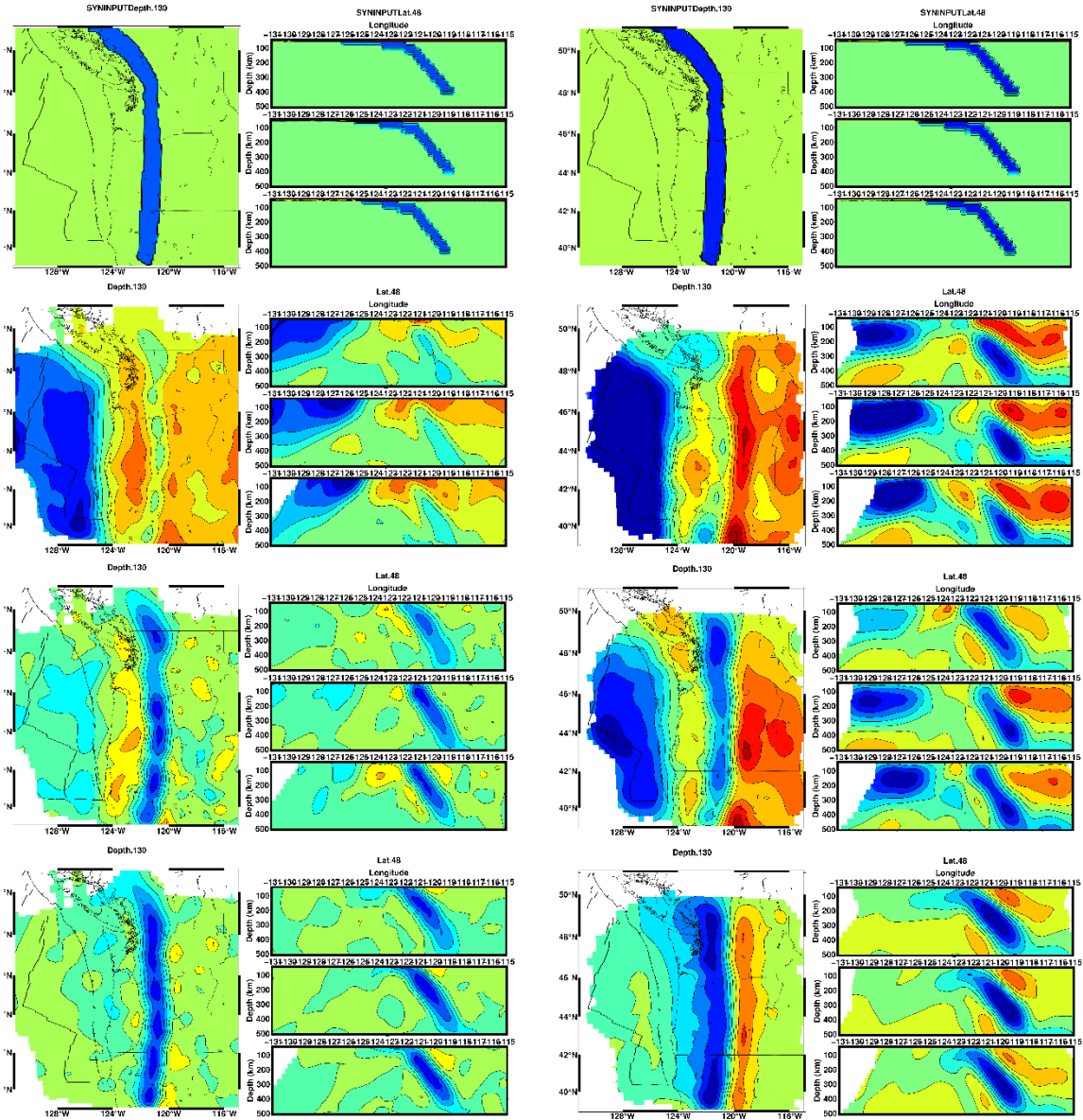


Figure 7: Synthetic tests of P and S wave data. P data on the left and S data on the right. (Top panel) The synthetic model. There is crustal structure in the upper 50 km and a synthetic slab. (Upper-mid panel) Inversion of synthetic data with no correction done for near surface structure. (Lower-mid panel) Inversion of synthetic data using undamped station statics. (Bottom panel) Inversion of synthetic data using an a priori starting model.

5.2.2 Tomographic Inversions

Figure 7b shows the results of inverting synthetic data without use of station statics and assuming a one-dimensional prior model. This is not a common workflow, but we present it as a baseline to demonstrate how near surface structure can streak

downward and obscure deeper structures. The resulting images show large amplitude artifacts concentrated at the top of the model. The velocity anomalies vary laterally in a predictable manner, with a sharp gradient separating the onshore and offshore regions. The vertical extent of the anomalies are streaked well below the 50-km limit of near surface structure and they mask the slab anomaly, except in the deepest portions of the model. The final RMS delay-time residual is 0.32 s for P and 0.56 s for S.

[Figure 7c](#) shows results of an inversion using a one-dimensional prior model and undamped station static terms. Station statics are free parameters in the inversion that can absorb travel times common to a station, an approach that is widely used (e.g. [Dziewonski & Anderson, 1983](#); [Hawley et al., 2016](#); [Roth et al., 2008](#)) due to ease of implementation. Our results show that station static terms do absorb much of the near surface structure for the P data. However, in the nearshore region the inversion introduces a coherent subslab, low-velocity anomaly that is a known artifact. We attribute this artifact to the heterogeneity of the region, which includes the ocean-continent boundary, the shallow dipping portion of slab and its transition to a steeper angle. S data shows similar low velocity anomalies subslab, but also has lingering anomalies due to the near surface structure. While the slab-like anomaly is better imaged compared to [Figure 7b](#), the uppermost portions of the slab are poorly recovered, which is likely due to station statics partially absorbing that structure. For this inversion, the RMS of the delay times is 0.27 s for P and 0.49 s for S, which is considerably less than the previous inversion. We attribute this relative reduction in RMS misfit to the addition of >1000 additional free parameters in the inversion.

Figure 7d shows results of an inversion using the known, three-dimensional shallow structure as a prior model. This prior model represents a workflow relying on accurate estimation of the shallow structure. The inversion results successfully reduce artifacts attributed to shallow structure, provides improved resolution of the subducting slab at all depths, and does not introduce any significant anomalies in the sub-slab region. This overall result is expected as the exact shallow structure is known. Prior models of near surface structure can never have this degree of certainty, but utilizing regional seismic studies (e.g., surface wave tomography and receiver functions) can provide good quality constraints. Interestingly, while this result contains fewer artifacts the RMS misfit is 0.28 s for P and 0.54 s for S, which is greater than the result obtained using undamped station statics. This is expected due to a change in the number of free parameters and suggests that RMS misfit alone may not be the best metric by which a tomographic result is evaluated.

While these inversions represent ideal conditions — synthetic data for a relatively simple, isotropic model — several general insights can be made. First, station static terms absorb structure at many depths, not just near the surface. Consequently, if mantle heterogeneity is laterally expansive, station statics will effectively remove this signal (see [Byrnes et al., 2017](#)). Second, inclusion of undamped station statics can introduce significant imaging artifacts, for example, in the sub-slab region near the ocean-continent transition. Third, using a good quality priori model of shallow structure reduces imaging artifacts and may increase data misfit if the number of free parameters decreases. Lastly, we note that RMS misfit does not directly correspond to improved model fidelity because station static terms absorb any structure (not just shallow) that reduces the data misfit.

6.0 Cascadia Subduction Zone Tomography

We present tomographic P-wave results using the measured CSZ data and modeling steps comparable to our synthetic inversions (Sec. 5). By comparing the results of multiple tomographic inversions, we identify parts of the model influenced by choice of workflow, note potential artifacts, and present our preferred model. We first construct a prior model of the CSZ near-surface structure, derived from previous studies, and compare its predictions to the synthetic data.

6.1 Near Surface Structural Model

Our prior model of near surface structure includes elevation and uses results of regional Rayleigh wave studies to constrain absolute velocities in the upper 50 km. We use two surface wave models representing the onshore (Schmandt & Lin, 2014; SL14) and offshore (Bell et al., 2016; B16) regions. To remove sharp discontinuities where the models join, they are smoothed together in a 100-km-wide band where they overlap offshore (Figure S2). SL14 was produced utilizing mainly data from the IRIS Transportable Array (2003) and was developed specifically as a starting model for teleseismic body wave inversions (Schmandt & Lin, 2014). SL14 is a 3-layer model (0-7 km, 7-15 km, and 15-Moho) with a variable crustal thickness spanning the continental US. Crustal thicknesses do not exceed 50 km in our study region. B16 is an offshore model produced using the Cascadia Initiative dataset. The model is available to relatively deep depths, but we restrict our use to the upper 50 km. Due to the low seismic frequencies used in this study, the upper 20 km is largely unconstrained by data (Bell, personal communication); however, this region is defined by a detailed starting mode that

includes an age-dependent lithosphere, sediment thicknesses, variable thicknesses for oceanic crustal layers (2A, 2B, and 3), and a distinct forearc region (See Sec. 3.3 of Bell et al., 2016 for more details). The B16 model defines both S-wave and P-wave velocities (See Sec. 3.3 of Bell et al., 2016), while the SL14 model defines only S-wave velocities; P-wave velocities were obtained by using the equations of Brocher (2005). Both models were modified slightly (e.g. a self-consistent definition of Moho depth) to ensure that they remained accurate when elevation is included.

Delay times due to sediments offshore are applied as a station specific correction prior to conducting the forward problem. Sediment thicknesses are taken from Gardner et al. (1993) and Divins (2003) and the average velocity is calculated using empirical relations from Bell et al. (2014). Where available for specific stations, thicknesses from Bell et al., (2014) are used. Within our starting model, sediment layers defined in the offshore portion are removed and replaced with crustal velocities. Sediment thickness variations can introduce delay times up to 2 s for S waves and 0.5 s for P waves.

Figure 8 shows that relative to AK135 predictions, the station-averaged delay times predicted by the CSZ near surface model are bimodal, with distinct onshore-offshore regions. The difference between average onshore and offshore station delays is about 1 s for P and 1.5 s for S, which is comparable to predictions from the 2D refraction profiles and our generic 3D model (see Sec. 5.0). Figure 8 shows that there is a significant reduction in station-averaged delay times after removing delay time contributions from the near surface starting model. The near-surface model reduces the variance in station-averaged delay times by 50% for P and 31% for S. Several notable regional-scale delay time patterns exist, for example, throughout the Gorda deformation

zone station-averaged delay times appear uncorrelated with tectonic boundaries and are consistently delayed with respect to the JdF region. Other patterns, such as the north-south trending advanced delays, that were present in the unaltered average station delay times are now more pronounced.

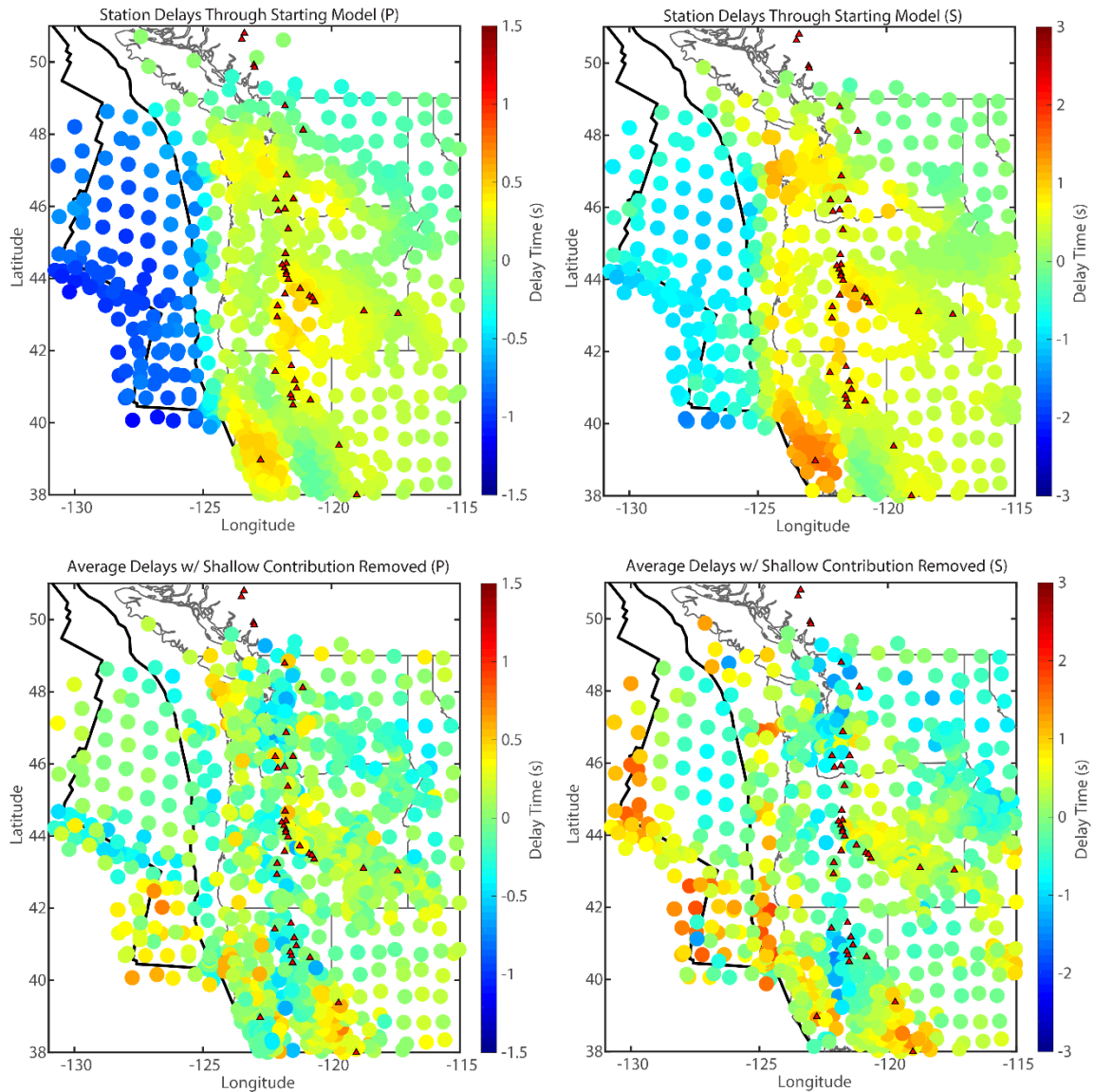


Figure 8: (Upper Panels) Predicted average station delays through the Cascadia subduction zone starting model for P (Left) and S (Right) models. (Bottom Panels) Station averaged delays after the contribution from the starting model has been removed, and the dataset is demeaned on an event basis for P (Left) and S (Right) models

6.2 Tomographic Inversions

Figure 9a shows the results of inverting the observed P delay-time data assuming a one-dimensional prior model without station statics. This inversion reconstructs pronounced low- and high-velocity anomalies down to 200 km depth beneath the continental and oceanic regions, respectively. Beneath much of the JdF plate, this inversion reconstructs high-velocity anomalies because variations in elevation and crustal thickness are not addressed. Beneath the western US, high-velocity anomalies are present in a north-south trend near the volcanic arc and broadly beneath western Idaho. Pronounced low-velocity anomalies are recovered at asthenospheric depths throughout much of the continent. Cross sections show dipping high-velocity perturbations consistent with a subducting slab, imaged clearly at depths below 150 km but obscured at shallower depths where large low-velocity anomalies are present. Synthetic results indicate that many of the structures in the upper 200 km are likely artifacts due to vertically smeared shallow structure, which is unaccounted for in the model.

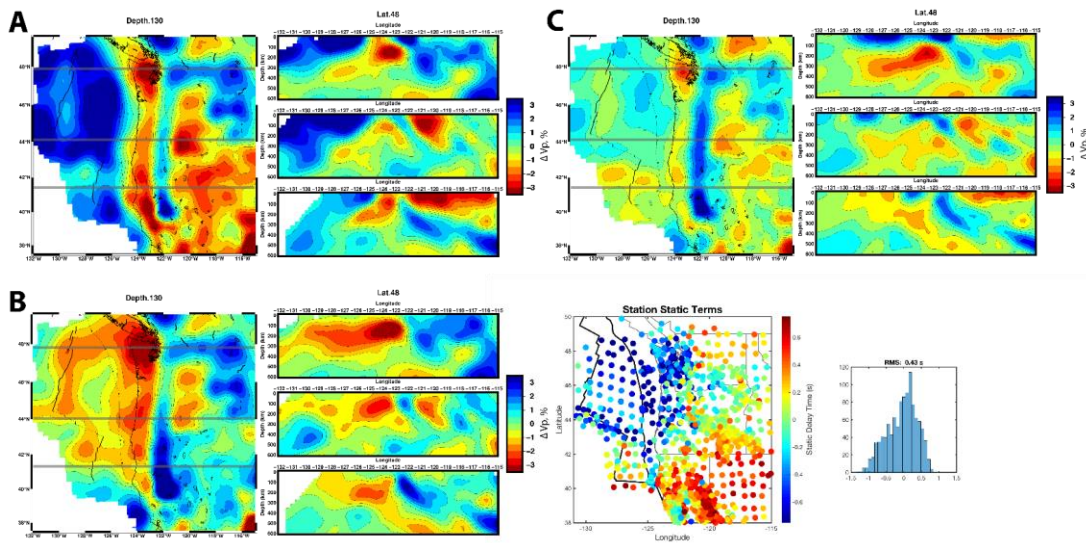


Figure 9: Tomographic inversions of the P-wave data. (A) Inversion with no station statics and no a priori starting model. (B) Inversion with undamped Station statics and no a priori starting model. Station static terms are shown to the right. (C) Inversion with an a priori starting model and no station statics.

Figure 9b shows the results of inversion assuming a one-dimensional starting model and using undamped station static terms. This workflow reduces the onshore-offshore variation reconstructed in the previous inversion. Broad low-velocity anomalies are present offshore in the upper 200 km beneath the entirety of the oceanic plate, with a concentrated high amplitude band in the sub-slab region at 100-200 km depth. Onshore, low-velocity anomalies in the upper 200 km are reduced in most regions and high-velocity anomalies associated with the slab increase in amplitude, especially in the south. The slab is imaged well at depths below 150 km, however, at shallower depths beneath central and northern Cascadia the slab structure is still obscured. Our synthetic studies suggest that low-velocity, sub-slab anomaly and poor amplitude recovery of the shallow slab are artifacts of a workflow that uses station statics alone to account for near surface structure.

Forward modeling (Sec. 5.1) indicates 3 shallow structure contributions to teleseismic delay times: elevation, crustal thickness, and local geology. Our preferred methodology to account for this structure uses a three-dimensional starting model of near surface structure (Sec. 6.1). Figure 9c shows heterogeneous offshore structure, a better-defined shallow slab, and an absence of broad low velocities sub-slab. Observations of velocity anomalies beneath the JdF ridge and the Gorda deformation zone are consistent with recent tomographic studies focusing on offshore structures (Bell et al., 2016; Byrnes et al., 2017) and suggest an improvement in resolution for this model. The absence of broad low-velocity anomalies sub-slab, replaced by local anomalies in the north and south, along with our synthetic tests suggest that margin wide low velocities subslab are likely an imaging artifact.

7.0 Discussion

7.1 Importance of a priori Starting Models

Crustal thickness, elevation, and sediment thickness variations between onshore-offshore regions lead to a significant signal in P- and S-wave travel-time data, which left unaccounted for, dominate structure in the upper 200 km of our images and obscure deeper mantle structure. We focus on the CSZ but our findings are analogous to any region containing oceanic-continental plate boundaries or large crustal heterogeneities (Waldhauser et al., 2002). Several techniques have been developed to address near surface structure, however, both synthetic and real data inversions show that different methods produce significantly different images. Our synthetic tests suggest that these variations occur where shallow structure changes rapidly and/or has a complex relationship with deeper structures, in this case beneath the CSZ forearc. We suggest that careful consideration of the employed methodology is necessary to avoid over-interpretation of potential imaging artifacts.

We prefer a methodology that accounts for shallow structure using a realistic starting model derived from independent constraints. This approach incorporates known delay time contributions such as elevation, crustal thickness, and velocity variations. By implementing this as a starting model, our iterative ray-tracing algorithm accounts for this structure when refining ray geometry. While uncertainties exist in any such starting model, we find them preferable to errors incurred by assuming a 1D velocity structure or that shallow structure can be accurately modeled by a static station term.

We caution against using station static terms alone, particularly in a subduction setting, as they can lead to unwanted artifacts and under-recovered structure. The source

and size of errors are difficult to assess when using station statics, which is important for onshore-offshore studies where these shallow variations dominate the relative travel-time signal. The station static term's dependence on the travel-time data propagates errors into the slowness perturbations and allows the array geometry, which is likely not evenly distributed between regions, to influence estimates of the static correction. Further, because the static terms depend on the integrated time along their raypaths, they absorb and are sensitive to mantle structure (Robertson & Woodhouse, 1997). This becomes problematic when imaging structures with a broad lateral extent, such as a shallow dipping slab, with sub-vertical rays because several incoming ray geometries will sample the structure making it favorable to absorb the resulting signal. Synthetic studies show broad patterns in the station statics where mantle structure has been absorbed.

7.2 Improved Resolution Beneath the Forearc and Identification of Artifacts

The region most influenced by our joint onshore-offshore dataset lies beneath forearc, in the sub-slab mantle where onshore and offshore event-station pairs share raypaths. This can be seen in the strong recovery of synthetic anomaly amplitudes here (Figure 7 and S3). The sub-slab mantle is of particular interest because there is still debate concerning the nature of seismic structures there and their impact on subduction dynamics (Bodmer et al., 2018; Bodmer, in review; Hawley et al., 2016).

We image two prominent localized sub-slab low-velocity features in the northern and southern sections of the CSZ between 100-250 km depth. Low-velocity anomalies are not present in central Cascadia. We do not find evidence for margin wide sub-slab low-velocity anomalies in the upper 200 km. This contrasts with the recent onshore-

offshore P-wave tomography of Hawley et al. (2016) who image low velocities at ~150 km depth sub-slab throughout the subduction zone interpreted as “pooling” of buoyant entrained mantle. We suggest that the discrepancy arises from differences in data processing methodology, specifically their use of station statics to account for shallow structure. We suggest that our inversion of the measured data with undamped station statics is analogous to the Hawley model, in that it recovers broad low velocities subslab and only used station statics to account for near surface structure. We note that our synthetic tests show that a station static approach can cause margin wide low-velocity artifacts sub-slab, thus we are hesitant to interpret this model instead preferring results that utilize a priori starting models to account for near surface structure.

7.3 Limitations

We are confident that our starting model approximates the actual CSZ near surface structure and consequently improves the fidelity of our tomographic images, however, improvements to the starting model and its implementation in the forward problem can and should be made in future studies. Our starting model is an amalgamation of available surface wave models for the region, which likely leads to some error. As more onshore-offshore results from teleseismic surface waves, ambient noise, and receiver functions become available starting models can be further refined and compared. Further, our ray-tracing grid is coarse compared to the length scale of variations in the upper 50 km. This is not particularly problematic for vertical teleseismic raypaths but must be considered in order to include regional seismicity for multiscale imaging. Finally, the assumption that the CSZ is isotropic is almost certainly violated. Though

many features of our isotropic model appear robust we caution that, until the effects of CSZ anisotropy are better characterized and incorporated into tomographic inversion, uncertainty remains.

7.3 Future Directions

Future work addressing the challenges of shore crossing data will come in two main forms. First, I have presented a new onshore-offshore S-wave delay time dataset, which was used for synthetic studies but has not yet been inverted for a model of Cascadia subduction zone structure. I will focus efforts on running these models and comparing them to the already published P-wave model. Based on these results we can identify regions where V_p and V_s models differ and begin to draw interpretations. Second, I will continue efforts to include anisotropy in synthetic modeling to get a better idea of how anisotropic structure impacts tomographic imaging. Some of this analysis has already begun but is outside the scope of this dissertation.

CHAPTER VI

CONCLUSIONS

This dissertation explored the important role that the oceanic mantle plays in subduction dynamics. It highlights the fact that most margin-scale subduction zone studies only are able to consider half the problem (onshore) and lack the coverage on the oceanic plate necessary to fully characterize the incoming system.

The collection of ocean bottom seismometer data collected during the Cascadia Initiative allowed me to investigate mantle structure of an entire oceanic plate, allowing me to interpret results in the context of the entire system instead of a single region. This allowed me to produce the first plate wide study of SKS shear wave splitting, investigating the heterogeneity of mantle flow beneath multiple diverse tectonic boundaries as well as the plate interior. These results highlight the non-uniform nature of mantle dynamics along-strike of the Cascadia margin. Asthenospheric flow patterns are related to the motion of tectonic plates as well as the deformation zones that define their boundaries.

The amphibious nature of the Cascadia Initiative along with recent dense onshore seismic deployments allowed for improved imaging of the mantle structure beneath the subduction zone. Through this data I discovered low-velocity anomalies beneath the subducting plate, which the aforementioned shear wave splitting study helped to interpret as local upwellings. I proposed a new hypothesis, that buoyancy subslab was able to impact megathrust processes, modulating the megathrusts behavior and influencing the spatial extent of segmentation. This is an entirely new view of subduction zone dynamics,

a bottom up approach, differing from previous studies which focus on properties on the overlying crust, uppermost oceanic structure, or plate interface to explain segmentation.

This model has potential implications for several other subduction related processes. One of these is the segmentation of forearc topography, which I observed was spatially correlated with the seismic anomalies I imaged. By synthesizing results from geomorphology, geodynamics, and seismology, I developed a model that explains how subslab buoyancy could contribute to the preferential uplift of certain regions of the forearc and provide lateral support for high topography through shear forces on the interface. This differs from previous margin wide models which suggested that plate age variations drove differential topography.

These seismic results were possible because of the increased, dense coverage afforded by large community experiments but also because of the methodology I employed to invert the shore crossing dataset. Teleseismic data is ill-suited to resolve structure near the surface (<50 km). Using synthetic forward modeling I showed that in a shore crossing environment, where changes in elevation, crustal thickness, and sediment cover are large, the effects of this structure can significantly impact delay times. Many practitioners still use station statics in their tomographic inversions to account for this structure, however, I showed that this can induce artifacts and decrease resolution of mantle targets.

In all, this work highlights an important gap in our knowledge, the detailed characterization of the incoming oceanic mantle into subduction zones. Through large community experiments and advances in ocean bottom seismometers, we are on the cusp of being able to fill this knowledge gap for subduction zones globally. For now, this work

has major implications for the Cascadia subduction zone and the dynamics of the megathrust. It also introduces new questions, however, such as: Is Cascadia an endmember case or do buoyant anomalies/subslab exist in other subduction zones? How do all the potential influences on the megathrust interact to give rise to the segmentation in behavior? Can we piece together the tectonic history of the Cascadia margin with regard to large scale mantle processes? What is the future of the margin and plate fragmentation processes continue in southern Cascadia? To address these questions, future work will focus on characterizing other convergent margins and focusing on multi-scale studies of the Cascadia margin to improve our understanding of subduction zone dynamics.

APPENDIX A

CHAPTER II SUPPORTING INFORMATION

Table DR1 Page 1 of 4

Station	Lat	Lon	dt	phi	events	error dt	error phi	Zone	Event IDs
BB030	42.95	-126.93	1.8	-66	1	0.2	3	bianco	28
BB060	42.86	-126.11	1.6	72	2	0.3	7	bianco	30 37
BB070	43.31	-126.01	1.6	76	3	0.2	3	bianco	28 30 33
BB090	43.37	-126.66	0.8	74	4	0.1	2	bianco	28 30 36 37
BB120	43.98	-127.30	0.7	78	3	0.2	13	bianco	28 33 36
BB130	43.64	-127.47	0.5	70	5	0.2	10	bianco	28 30 33 35 36
BB140	43.42	-127.69	1.0	-88	1	0.7	32	bianco	36
BB150	43.31	-127.35	0.7	-84	1	0.8	33	bianco	36
BB170	43.14	-127.78	1.0	-29	1	0.5	20	bianco	36
BB180	42.87	-128.30	1.2	-27	4	0.3	7	bianco	30 33 34 36
BB200	43.49	-127.96	0.7	-90	2	0.2	9	bianco	28 36
BB230	43.57	-128.26	0.7	-86	4	0.1	5	bianco	28 36 38 43
BB240	43.43	-128.36	2.7	-52	3	0.4	1	bianco	28 31 43
BB260	43.62	-128.86	1.7	-21	4	0.2	4	bianco	27 30 32 33
BB290	43.63	-128.51	1.2	-70	3	0.2	6	bianco	28 33 38
BB300	43.84	-128.32	0.7	82	3	0.2	6	bianco	30 34 38
BB320	44.17	-128.71	1.5	84	3	0.3	4	bianco	28 37 42
BB330	44.61	-128.60	0.7	70	5	0.1	6	bianco	28 31 34 38 44
BB350	43.99	-129.08	1.1	-60	4	0.2	2	bianco	28 31 37 42
BB370	43.78	-129.39	0.9	-37	4	0.1	5	bianco	30 33 37 38
BB390	43.99	-129.68	0.6	-37	2	0.2	11	bianco	36 42
BB410	43.93	-130.00	0.8	-52	4	0.1	5	bianco	30 33 37 38
BB420	43.63	-130.21	1.0	-58	5	0.1	5	bianco	30 32 36 37 38
BB440	44.21	-130.46	0.7	-64	3	0.1	7	bianco	28 36 38
BB450	44.23	-130.77	0.6	-70	3	0.2	12	bianco	30 36 38
BB480	44.35	-130.02	0.8	-78	3	0.1	5	bianco	28 36 38
BB510	44.31	-129.34	0.7	-78	5	0.1	5	bianco	30 31 33 36 38
BB530	44.55	-129.82	1.4	-84	3	0.1	3	bianco	28 31 36
BB540	44.59	-130.19	1.1	-74	5	0.1	2	bianco	28 30 34 36 38
BB550	44.68	-130.62	0.5	-39	2	0.3	22	bianco	36 44
G37B	42.59	-127.72	1.1	-66	10	0.1	1	bianco	25 26 28 30 33 34 36 37 38 44
J06Stack	43.25	-128.80	0.8	-37	5	0.2	9	bianco	6 13 14 36 37
FS01B	40.33	-124.95	1.4	-72	4	0.2	3	gora	24 34 37 38 41
FS02B	40.35	-124.80	1.5	-21	2	0.4	9	gora	30 33
FS04B	40.24	-124.51	NA	NA	0	NA	NA	gora	NA
FS05B	40.39	-124.90	NA	NA	0	NA	NA	gora	NA
FS06B	40.38	-124.79	NA	NA	0	NA	NA	gora	NA
FS07B	40.34	-124.66	1.8	-60	1	0.4	10	gora	36
FS09B	40.44	-124.81	NA	NA	0	NA	NA	gora	NA
FS11B	40.43	-124.58	1.1	-37	1	0.6	24	gora	36

Table DR1 Page 2 of 4

FS12B	40.44	-124.51	NA	NA	0	NA	NA	gorda	NA													
FS13B	40.49	-124.81	NA	NA	0	NA	NA	gorda	NA													
FS14B	40.50	-124.59	NA	NA	0	NA	NA	gorda	NA													
FS15B	40.49	-124.51	NA	NA	0	NA	NA	gorda	NA													
FS18B	40.57	-124.50	NA	NA	0	NA	NA	gorda	NA													
FS19B	40.63	-124.47	NA	NA	0	NA	NA	gorda	NA													
FS20B	40.39	-125.03	NA	NA	0	NA	NA	gorda	NA													
G02B	40.05	-125.30	1.4	-78	5	0.2	4	gorda	28	30	36	37	38									
G03Stack	40.06	-126.16	2.2	-35	2	0.3	5	gorda	11	36												
G05B	40.07	-127.75	1.6	-80	3	0.2	2	gorda	30	36	38											
G10B	40.68	-125.55	1.2	-72	9	0.1	1	gorda	28	30	33	36	37	38	39	41	44					
G11B	40.69	-126.38	1.8	-80	2	0.3	4	gorda	30	36												
G12B	40.69	-127.23	1.2	-74	1	1.0	35	gorda	27													
G13B	40.68	-128.03	1.3	-76	4	0.2	3	gorda	28	33	36	37										
G19B	41.31	-125.77	1.2	-74	3	0.1	2	gorda	23	28	36											
G20B	41.30	-126.61	1.4	-76	6	0.1	2	gorda	28	30	33	36	37	38								
G21B	41.42	-127.45	1.2	-70	4	0.2	4	gorda	27	36	37	38										
G22B	41.31	-128.27	1.1	-66	3	0.1	5	gorda	28	36	38											
G28B	41.94	-126.73	1.5	-62	7	0.1	2	gorda	28	29	30	32	36	42	43							
G29B	41.98	-127.48	1.1	-68	4	0.1	3	gorda	28	33	36	37										
G305Stack	41.96	-128.32	1.6	-76	3	0.4	11	gorda	6	33	36											
G36B2	42.60	-126.90	1.4	-80	5	0.2	3	gorda	28	30	33	38	40									
J09B	40.20	-124.73	0.9	9	1	0.5	25	gorda	36													
G27B	41.92	-126.02	1.5	86	3	0.1	2	jdf	28	38	42											
G35B	42.57	-126.06	1.8	76	2	0.2	4	jdf	25	38												
J11B	43.54	-126.37	0.8	64	5	0.1	5	jdf	25	30	36	37	38									
J19B	44.18	-126.27	0.6	66	5	0.1	5	jdf	25	28	30	36	38									
J20B	44.35	-127.10	0.8	62	5	0.1	2	jdf	28	30	33	36	38									
J21C	44.53	-128.04	1.7	78	2	0.5	6	jdf	48	55												
J27B	44.85	-126.31	1.2	74	3	0.3	7	jdf	23	33	36											
J28Stack	45.06	-127.16	1.2	74	7	0.2	2	jdf	18	28	33	36	48	56	58							
J29Stack	45.18	-128.01	1.1	58	4	0.1	2	jdf	13	18	45	51										
J30Stack	45.42	-128.91	0.8	52	8	0.1	3	jdf	4	5	6	14	45	46	48	51						
J35Stack	45.50	-126.27	1.1	62	12	0.1	3	jdf	1	6	7	8	12	17	18	21	45	48	56	58		
J36Stack	45.69	-127.12	0.9	56	9	0.1	2	jdf	1	2	15	21	45	48	51	52	58					
J37Stack	45.86	-127.99	0.6	78	6	0.1	6	jdf	6	13	18	45	51	58								
J38Stack	46.04	-128.85	0.6	56	5	0.1	9	jdf	6	10	12	13	56									
J43Stack	46.14	-126.17	0.8	72	14	0.1	3	jdf	1	3	6	7	9	19	20	21	45	47	51	52	55	58
J44Stack	46.32	-127.04	0.9	64	6	0.1	4	jdf	1	6	9	45	51	58								
J45Stack	46.52	-127.90	1.0	68	3	0.4	11	jdf	6	13	48	51	56	58								
J46Stack	46.66	-128.79	0.6	13	11	0.1	3	jdf	6	12	13	19	45	46	47	48	54	56	58			

Table DR1 Page 3 of 4

J51A	46.80	-126.16	0.7	50	4	0.2	6	jdf	6	17	20	21							
J52Stack	46.99	-127.02	0.8	74	5	0.1	5	jdf	6	13	47	50	51						
J53Stack	47.16	-127.92	0.7	66	5	0.1	5	jdf	6	47	53	56	58						
J59Stack	47.51	-126.42	0.6	54	5	0.1	7	jdf	1	21	22	47	58						
J61Stack	47.87	-128.20	1.2	58	8	0.1	2	jdf	6	12	13	46	47	48	49	53			
J67Stack	48.15	-127.08	1.0	56	11	0.1	3	jdf	5	6	12	13	15	17	45	47	51	52	58
J68Stack	48.48	-127.83	1.2	54	4	0.1	6	jdf	6	48	51	56							
A04D	48.72	-122.71	0.6	70	4	0.1	4	land	6	30	51	58							
E04D	46.56	-122.57	1.0	76	4	0.1	1	land	28	30	36	38							
I04D	43.79	-122.41	1.9	64	4	0.1	2	land	6	30	36	38							
K02D	42.70	-123.67	1.8	46	4	0.1	1	land	6	30	36	51							
O02D	40.18	-121.80	0.9	44	4	0.1	8	land	6	30	33	37							
J48Stack	47.13	-130.64	1.5	-74	3	0.2	2	pacific	30	37	51								
J63Stack	48.21	-130.00	0.8	-64	10	0.1	4	pacific	12	14	25	26	30	33	36	47	51	58	
J23Stack	44.84	-129.68	0.7	-80	7	0.1	4	ridge	12	26	30	36	38	45	51				
J31Stack	45.55	-129.67	0.7	68	5	0.2	10	ridge	13	14	45	51	56						
J32C	45.71	-130.60	1.5	-11	2	0.3	5	ridge	48	56									
J39Stack	46.18	-129.64	0.8	5	10	0.1	4	ridge	6	7	9	14	47	48	51	53	56	58	
J47Stack	46.84	-129.71	0.8	33	7	0.1	2	ridge	6	9	13	45	53	57	58				
J54Stack	47.34	-128.81	0.6	-7	4	0.2	15	ridge	7	10	48	51							
J55Stack	47.53	-129.71	1.2	-37	1	1.0	25	ridge	6										
J69C	48.63	-128.74	1.4	52	2	0.2	3	ridge	51	58									
FN01C	46.88	-124.33	NA	NA	0	NA	NA	subduction	NA										
FN02C	46.95	-124.43	NA	NA	0	NA	NA	subduction	NA										
FN03C	46.89	-124.53	NA	NA	0	NA	NA	subduction	NA										
FN04C	46.92	-124.60	NA	NA	0	NA	NA	subduction	NA										
FN05Stack	46.86	-124.66	NA	NA	0	NA	NA	subduction	NA										
FN07Stack	46.86	-124.79	NA	NA	0	NA	NA	subduction	NA										
FN08Stack	46.89	-124.88	NA	NA	0	NA	NA	subduction	NA										
FN09C	46.84	-124.89	NA	NA	0	NA	NA	subduction	NA										
FN10C	46.90	-124.99	NA	NA	0	NA	NA	subduction	NA										
FN11C	46.82	-125.05	NA	NA	0	NA	NA	subduction	NA										
FN12Stack	46.89	-125.12	NA	NA	0	NA	NA	subduction	NA										
FN13C	47.00	-125.30	1.0	66	2	0.2	6	subduction	56	59									
FN14Stack	46.02	-124.96	1.3	31	2	0.2	2	subduction	1	20									
FN16A	46.80	-125.52	1.3	80	3	0.3	6	subduction	1	6	13								
FN18A	46.70	-124.72	1.4	90	2	0.5	9	subduction	1	6									
FN19C	46.73	-124.37	NA	NA	0	NA	NA	subduction	NA										
G09B	40.66	-124.72	NA	NA	0	NA	NA	subduction	NA										
G17B	41.28	-124.34	NA	NA	0	NA	NA	subduction	NA										
G18B	41.30	-124.94	NA	NA	0	NA	NA	subduction	NA										

Table DR1 Page 4 of 4

G25B	41.92	-124.59	1.7	74	3	0.3	1	subduction	30	36	37
G26B	41.92	-125.18	1.4	74	1	0.8	21	subduction	37		
G34B	42.56	-125.20	2.4	72	2	0.4	6	subduction	30	33	
J10B	43.35	-125.54	1.6	76	4	0.2	2	subduction	28	33	37 38
J17B	43.79	-124.61	NA	NA	0	NA	NA	subduction	NA		
J18B	44.01	-125.47	1.2	70	6	0.1	1	subduction	28	30	36 37 38 43
J25Stack	44.47	-124.62	1.2	46	2	0.4	15	subduction	1	2	
J26C	44.65	-125.47	0.9	58	2	0.6	23	subduction	47	58	
J33Stack	45.11	-124.57	1.1	50	5	0.2	6	subduction	6	13	20 36 51
J34C	45.31	-125.42	NA	NA	0	NA	NA	subduction	NA		
J41Stack	45.81	-124.54	1.9	25	2	0.3	5	subduction	1	58	
J42C	45.93	-125.30	1.7	54	1	0.4	12	subduction	56		
J49Stack	46.44	-124.43	NA	NA	0	NA	NA	subduction	NA		
J50Stack	46.64	-125.30	0.9	56	7	0.2	6	subduction	1	12	20 21 47 50 58
J57Stack	47.08	-124.45	NA	NA	0	NA	NA	subduction	NA		
J58Stack	47.32	-125.58	1.2	70	5	0.3	7	subduction	13	14	20 50 59
J65Stack	47.89	-125.14	NA	NA	0	NA	NA	subduction	NA		
J73Stack	48.77	-126.19	NA	NA	0	NA	NA	subduction	NA		
M01Stack	49.15	-126.72	NA	NA	0	NA	NA	subduction	NA		
M02C	48.31	-125.60	NA	NA	0	NA	NA	subduction	NA		
M03Stack	47.89	-126.10	1.4	66	4	0.1	2	subduction	6	47	50 53
M04C	45.56	-125.19	1.7	76	2	0.4	2	subduction	48	58	
M05C	46.17	-124.93	2.1	76	1	0.6	5	subduction	58		
M06C	45.53	-124.93	1.6	-9	1	0.9	9	subduction	58		
M07A	44.90	-125.12	1.9	17	5	0.3	4	subduction	1	4	8 16 20
M08Stack	44.12	-124.90	NA	NA	0	NA	NA	subduction	NA		
M09B	44.25	-125.06	1.0	48	1	0.6	18	subduction	23		
M11B	42.93	-125.02	1.5	52	2	0.4	13	subduction	30	32	
M12B	42.18	-124.95	NA	NA	0	NA	NA	subduction	NA		
M14B	40.99	-124.59	0.4	-88	4	0.2	19	subduction	27	28	30 36

Table DR1: Summary of the stacked splitting observations for results shown in Figs. 2 and 3. Sites reporting a single year of data retain the original station name; sites reporting multiple years of data are followed by 'stack'. Uncertainties are reported at the one-sigma level of confidence; same as Fig. 3. Event IDs refer to Table DR2.

Table. DR2 (page 2 of 2)

ID #	year	day	hour	min	sec	mag	Lat	Lon	depth	# used
1	2011	296	10	41	23	7.1	38.7	43.5	16	12
2	2011	306	14	59	28	6.2	-55.3	-128.8	10	2
3	2011	318	4	5	11	6.4	-1.0	126.9	17	1
4	2011	334	0	27	7	6.0	15.5	119.0	9	1
5	2011	341	22	23	10	6.1	-27.9	-70.9	20	2
6	2011	348	5	4	59	7.1	-7.6	146.8	141	18
7	2012	10	18	36	59	7.2	2.4	93.2	19	4
8	2012	15	13	40	20	6.6	-61.0	-56.1	8	2
9	2012	37	3	49	13	6.7	10.0	123.2	11	4
10	2012	37	10	10	20	6.0	9.9	123.1	9	2
11	2012	80	17	56	19	6.3	-3.8	140.3	66	1
12	2012	81	22	15	6	6.6	-6.2	146.0	118	8
13	2012	85	22	37	6	7.1	-35.2	-72.2	41	13
14	2012	102	8	38	37	8.6	2.3	93.1	20	6
15	2012	105	10	56	19	6.2	-57.7	-65.3	15	1
16	2012	106	5	57	40	6.3	2.6	90.3	25	1
17	2012	108	3	50	16	6.7	-32.6	-71.4	29	3
18	2012	108	7	13	49	6.9	-5.5	147.1	198	4
19	2012	112	1	25	13	6.0	-1.6	134.2	17	2
20	2012	149	5	7	23	6.7	-28.0	-63.1	587	7
21	2012	175	4	34	53	6.1	3.0	97.9	95	5
22	2012	185	10	36	16	6.3	-40.0	173.8	230	1
23	2012	244	12	47	33	7.6	10.8	126.6	28	3
24	2012	247	18	23		6.3	-10.7	113.9	14	1
25	2012	258	4	51	47	6.3	-3.3	100.6	19	5
26	2012	282	11	43	31	6.2	-4.5	129.1	10	3
27	2012	286	0	31	28	6.6	-4.9	134.0	13	3
28	2012	316	1	12	39	6.9	23.0	95.9	14	17
29	2012	342	18	19	6	6.3	-38.5	176.1	163	1
30	2012	345	16	53	8	7.1	-6.5	129.8	155	20
31	2013	30	20	15	43	6.8	-28.1	-70.7	45	4
32	2013	47	4	37	36	6.2	5.8	125.8	105	2
33	2013	96	4	42	36	7.0	-3.5	138.5	66	14
34	2013	99	11	52	50	6.3	28.4	51.6	12	3
35	2013	104	1	32	22	6.5	-6.5	154.6	31	1
36	2013	106	10	44	20	7.7	28.0	62.0	80	30
37	2013	106	22	55	27	6.6	-3.2	142.5	13	15
38	2013	110	0	2	48	6.6	30.3	102.9	14	17
39	2013	131	2	8	9	6.2	26.6	57.8	15	1
40	2013	140	9	49	5	6.3	-44.9	-80.8	10	1
41	2013	153	5	43	4	6.3	23.8	121.1	17	2
42	2013	164	16	47	23	6.6	-10.0	107.2	9	2
43	2013	166	11	20	36	6.0	-33.9	179.4	195	2
44	2013	166	16	11	3	6.3	34.4	25.0	10	2
45	2013	228	2	31	6	6.5	-41.7	174.2	8	12
46	2013	244	11	52	30	6.5	-7.4	128.2	112	3
47	2013	267	11	29	48	7.8	27.0	65.5	15	12
48	2013	271	7	34	7	6.8	27.3	65.6	15	13

Table DR2 (page 1 of 2)

49	2013	273	5	55	56	6.4	-30.9	-178.4	42	1
50	2013	284	21	25	0	6.2	-30.7	-178.5	151	4
51	2013	285	13	11	53	6.8	35.5	23.3	40	18
52	2013	288	0	12	2	7.1	9.9	124.1	19	4
53	2013	304	23	3	59	6.5	-30.3	-71.6	29	5
54	2013	320	3	34	31	6.9	-60.3	-47.1	10	1
55	2013	321	9	4	55	7.8	-60.3	-46.4	10	2
56	2013	335	1	24	14	6.5	-7.0	128.4	10	12
57	2014	33	9	26	38	6.4	-32.9	-177.9	44	1
58	2014	43	9	19	49	6.9	35.9	82.6	10	22
59	2014	174	19	19	16	6.9	-30.0	-177.7	20	2

Table DR2: List of the events used in this study. Plots of the events by back azimuth are shown in Fig. DR2.

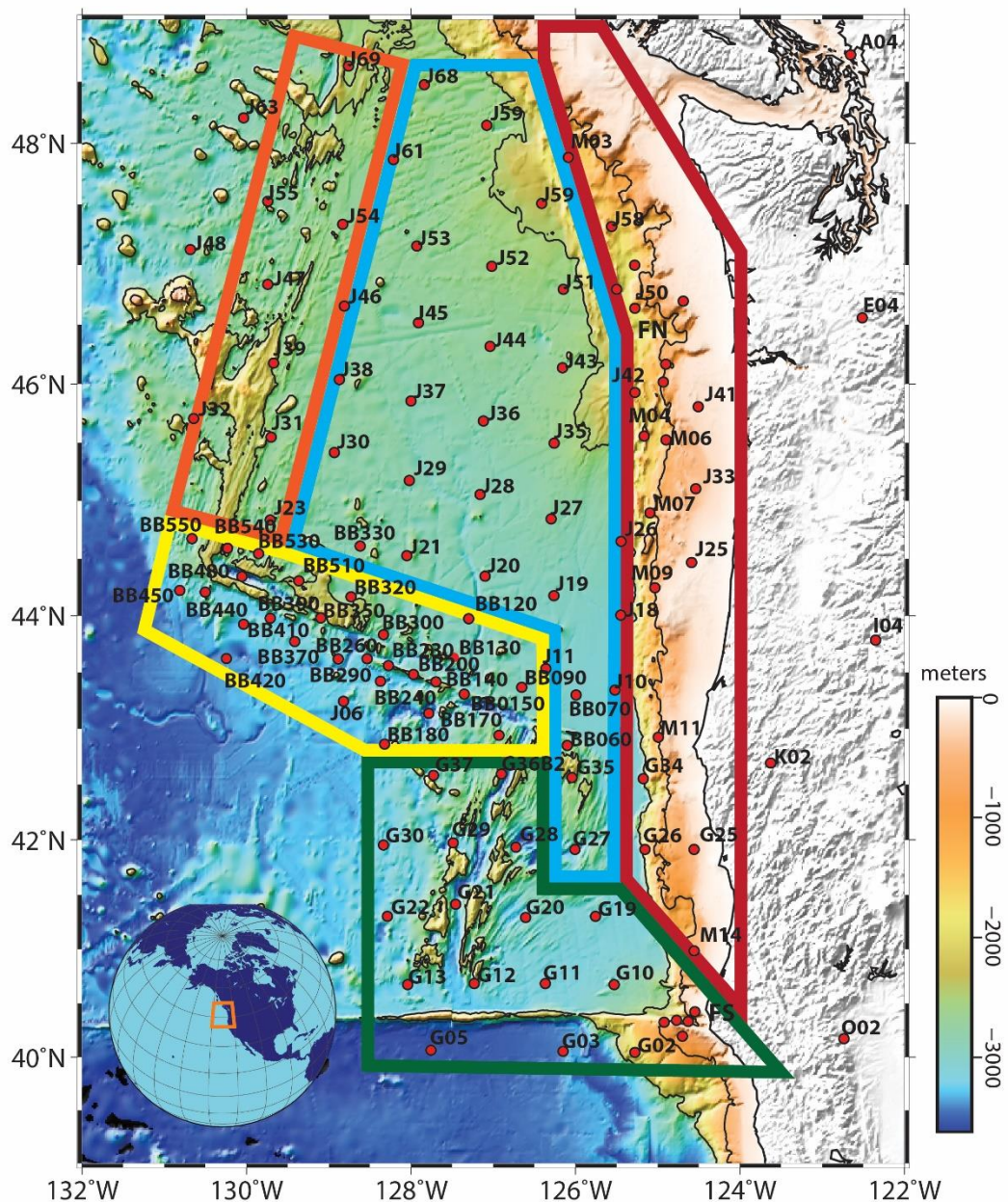


Fig. DR1: Bathymetric map showing stations used in this study (red circles) along with site names.

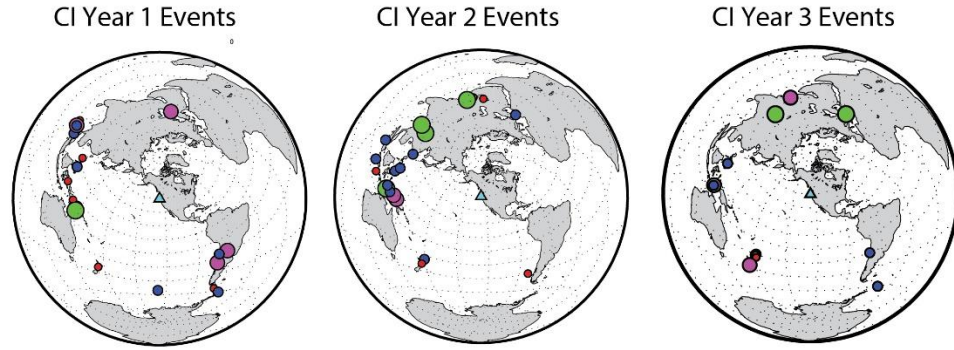


Fig.DR2: Distribution of events by back azimuth. Color and size of a circle corresponds to the number of stations that used a particular event: red = 1-2; blue = 3-5; magenta = 6-15; green = 16 or more. Each panel corresponds to one year of the Cascadia Initiative. Results obtained from the Blanco array used a subset of the events shown in year 1 and 2 panels.

A)

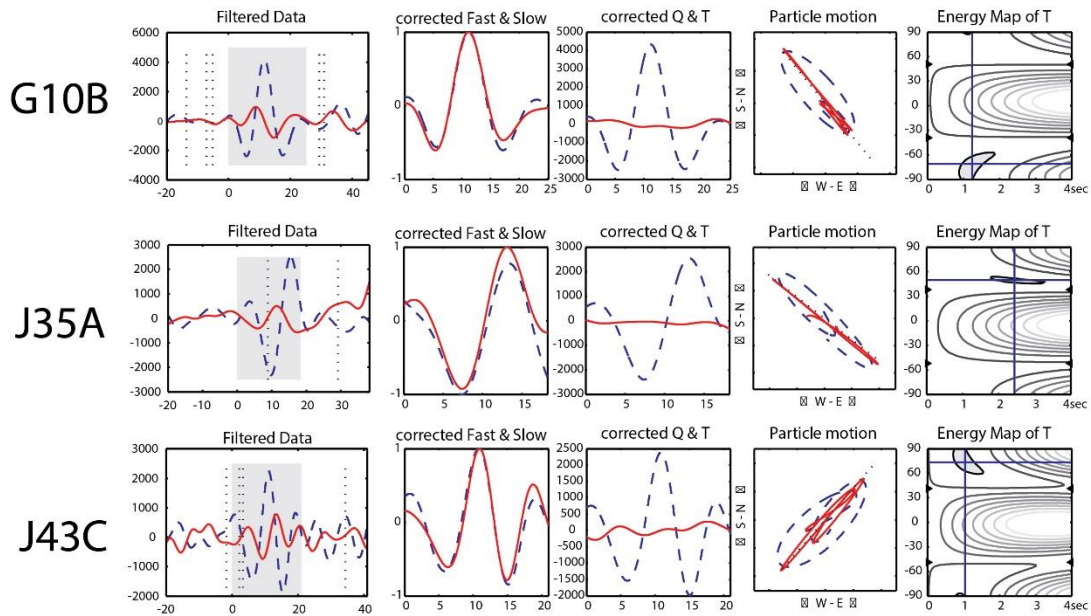
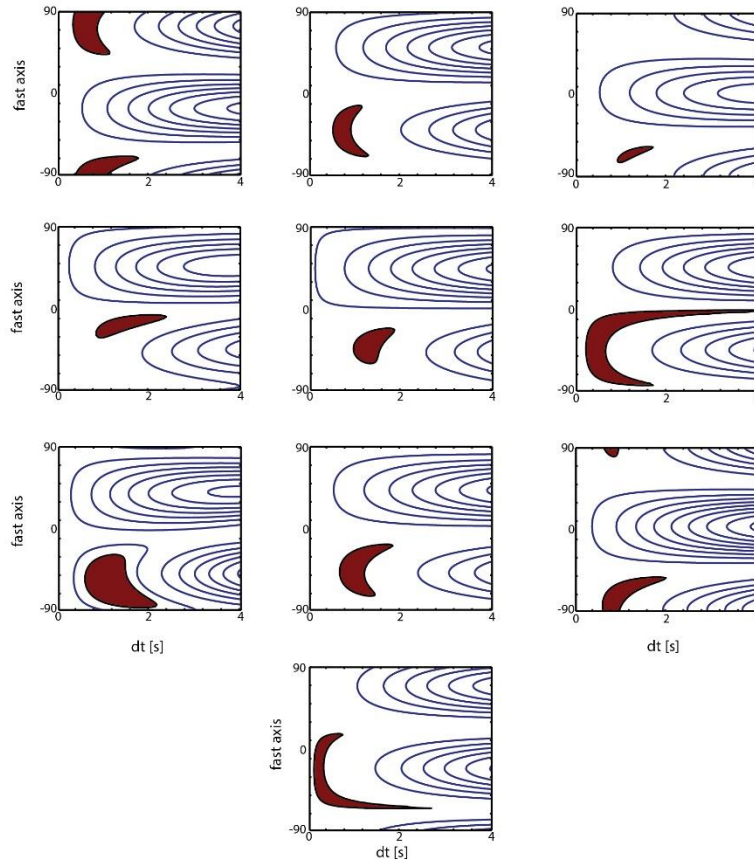


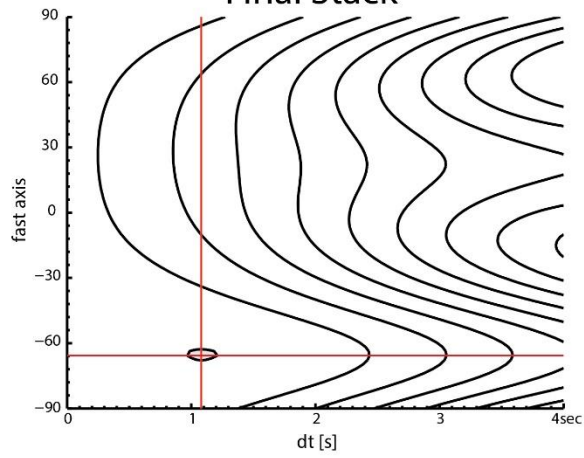
Fig. DR3: Examples of the data used in this study. A) Splitting measurements from G10B, J35A, and J43C. From left to right: i) filtered waveforms in the radial (blue dashed) and transverse (red) directions. Grey band indicates data used for a splitting measurement. ii) The waveforms after correcting for splitting in the fast (blue dashed) and slow (red) directions normalized by peak amplitude. iii) Corrected waveforms in the radial (blue dashed) and transverse (red) directions. iv) Particle motion before (blue dashed) and after (red) correcting for splitting. v) Energy map of the transverse channel produced by grid searching the fast polarization-delay time parameter space. The minimum is marked by the blue crosshairs and the gray region represents the 95% confidence interval. B) The transverse energy maps used to calculate the splitting parameters for station G37B (panels 1 to 10); 95% confidence interval for a single measurement is shown in red. These energy maps are normalized and stacked to produce the final map (panel 11).

B)

G37B Individual Measurements



Final Stack



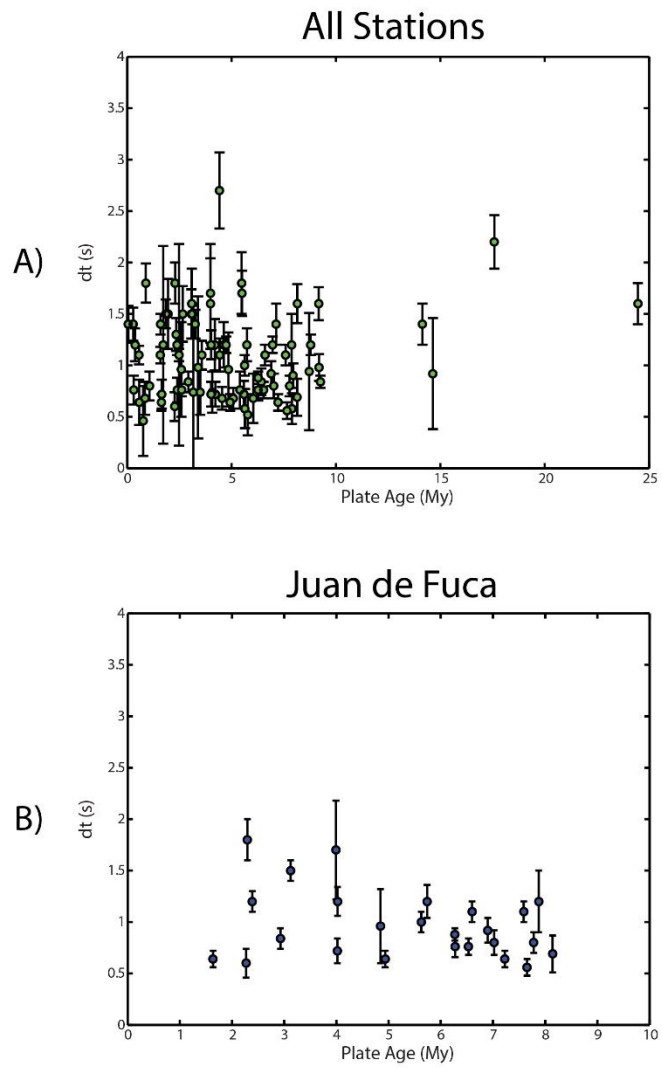


Fig. DR4: Observed delay times plotted by plate age for A) all OBSs used in this study and B) the subset of sites within the interior of the Juan de Fuca plate. Neither plot displays an age dependence.

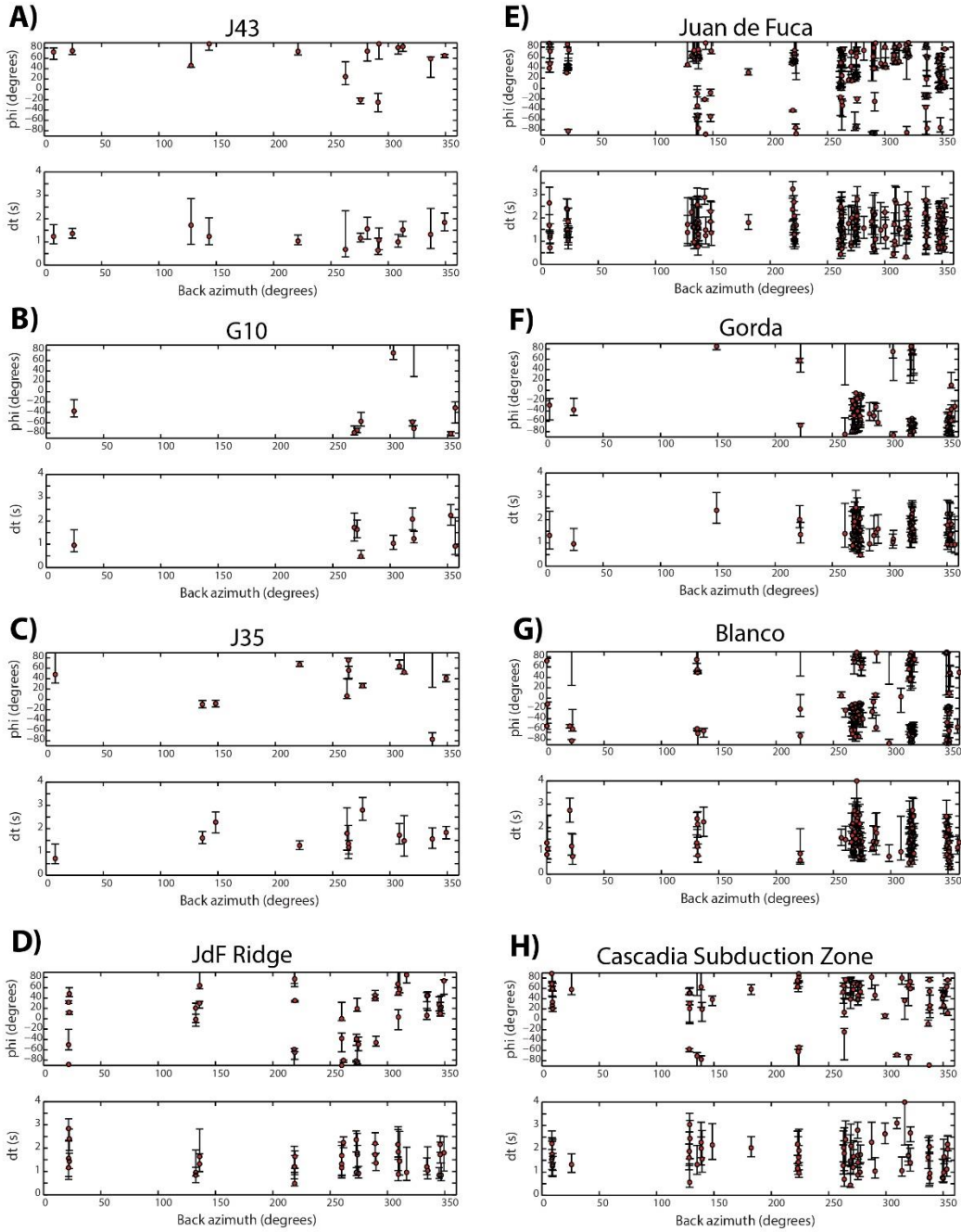


Fig. DR5: Results of individual measurements as a function of back azimuth for selected stations (J43, G10, and J35) and for each tectonic zone defined in Fig. 1. The presence of multiple anisotropic layers is predicted to produce splitting parameters that are dependent on back azimuth (see Fig. DR6). Results for individual stations and for tectonic zones are not adequate to identify a dependence on back azimuth. For each tectonic zone, the individual measurements generally cluster around the average obtained by stacking error surfaces.

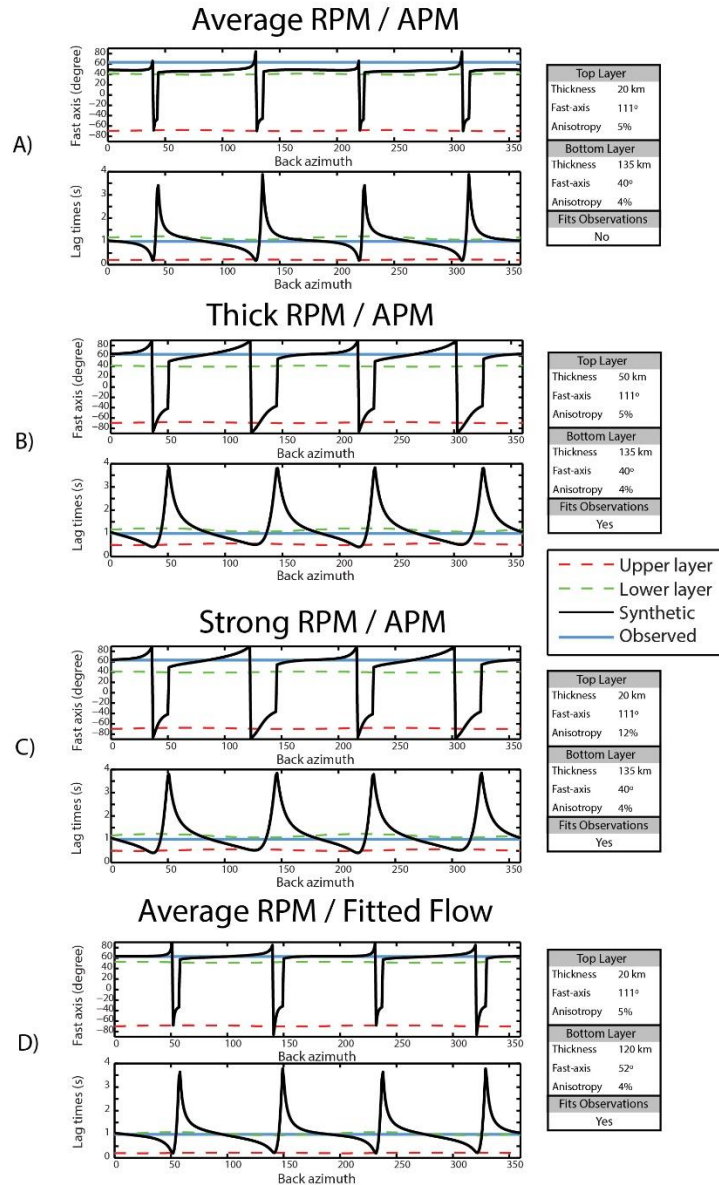


Fig. DR6: Predicted splitting parameters plotted by back azimuth for several two-layer models of anisotropy. Predictions are made using methodology of (Silver and Savage, 1994) and the MSAT software package (Walker and Wookey, 2012). Red and green dashed lines show contributions of upper and lower layers, respectively. Solid black line is the predicted apparent splitting parameter, which is the result of interactions in both layers. Solid blue line shows the average splitting parameters observed for sites located within the Juan de Fuca plate. Model parameters are provided to the right of each panel. A) Model with a 20-km-thick upper layer aligned with RPM and a 135-km-thick lower layer aligned with APM. The thickness of the top layer (20 km) is typical for the JdF plate, which varies between 5 and 30 km. This model does not fit the fast polarization observations (rotated ~15-20°). B) Model with a 50-km-thick upper layer aligned with RPM and a 135-km-thick lower layer aligned with APM. This model fits the observations. C) Model with a highly anisotropic (12% in 20 km) upper layer aligned with RPM and a 135-km-thick lower layer aligned with APM. This model fits the observations. D) Model with a 20-km-thick upper layer (5% anisotropic) aligned with RPM and a 120-km-thick lower layer with fast axis at N52°E. This model fits the observations. See text for discussion.

APPENDIX B

CHAPTER III SUPPORTING INFORMATION

Delay-time Measurement Details

We processed CI waveform data as follows. Instrument response was deconvolved (Haney et al., 2012) and a third-order Butterworth filter (corner frequencies of 0.0303 and 0.0833 Hz) was applied prior to measurement of delay times using cross-correlation (VanDecar & Crosson, 1990) (see Figure S1 for waveform examples).. Because the errors reported by the cross-correlation method are unrealistically small (Byrnes et al., 2017), the minimum uncertainty in these measurements was set to 0.25 s. For the previously reported onshore data, we use a subset that covers the geographic area of interest (see Figure 1). Relative delay times of P, pP, and PKP phases were measured in multiple frequency bands using a cross-correlation method (VanDecar & Crosson, 1990). The onshore data of Schmandt & Humphreys (2010a) provides 72,726 delay times (48%, 29%, 22%, and 1% at 1, 0.5, 0.3, and 0.1 Hz center frequency, respectively); for additional details see Sec. 2 of Schmandt & Humphreys (2010a).

Quality Control

A number of quality control criteria were adopted in order to identify stations and events considered to be outliers. First, we calculate vertical delays through a model of the upper 50 km (see below for details) and subtract this contribution from the measured delays. After this adjustment, we eliminate stations with station-averaged delay-times that fall outside of a 2.5σ threshold, assuming a Gaussian distribution. Next, we identify several

stations in the offshore data whose station-averaged delay-times either differed significantly between deployments at the same site or that differ significantly from nearby sites. We use information from S-wave data to support these manual selections; see Byrnes et al. (2017) for details and related figures. Lastly, we identify events that are poorly fit after several inversions and remove the associated data from the analysis.

Inversion Details

In this study, a 145 X 181 X 76 grid with 10 km nodal spacing is used for the forward calculations (centered about 125° W, 45° N). A 49 X 61 X 19 perturbational slowness model is nested within the forward model with 30 km horizontal spacing and a variable vertical spacing increasing from 30 to 60 km with depth. The fractional uncertainty of the model parameters decreases with depth below 300 km to prevent accumulation of anomalies. Final model weights for the penalty, vertical smoothness, horizontal smoothness, and station static damping are chosen through multiple inversions of real and synthetic data evaluating the data misfit and model recovery [For details of model parameterization see Toomey et al. (1994)].

3D Starting Model

Our prior model of near surface structure includes elevation and uses results of regional Rayleigh wave studies to constrain absolute velocities in the upper 50 km. We use two surface wave models (Bell et al., 2016; Schmandt & Lin, 2014) representing the onshore and offshore regions. To remove sharp discontinuities where the models join, we smoothed them in a 100-km-wide band where they overlap offshore (Figure S4). The

onshore model is a 3-layer model (0-7 km, 7-15 km, and 15-Moho) with a variable crustal thickness spanning the continental US. Crustal thicknesses do not exceed 50 km in our study region. The offshore model is available to relatively deep depths, but we restrict our use to the upper 50 km. The offshore model includes an age-dependent lithosphere, sediment thicknesses, variable thicknesses for oceanic crustal layers (2A, 2B, and 3), and a distinct forearc region (See Sec. 3.3 of Bell et al. (2016) for more details). The offshore model was already converted from an S-wave into a P-wave model using a variable V_p/V_s depending on the layer involved (Bell et al., 2016), while the onshore model was converted using the equations of Brocher (2005) in the same manner as Schmandt & Lin (2014). Both models were modified slightly to ensure that they remained accurate when elevation is included.

Figure S5a shows that relative to a one-dimensional model, the station-averaged delay times predicted by our near surface (< 50 km depth) starting model are bimodal, with distinct onshore-offshore regions. The average difference in the onshore and offshore station delays is about 1.2 s. Figure S5b shows that there is a significant reduction in station-averaged delay times after removing the contribution of the near surface prior model from the actual data. This suggests that our shallow model is a good representation of actual structure. The variance of station-averaged delay times is reduced by 64% after removing the near surface contribution.

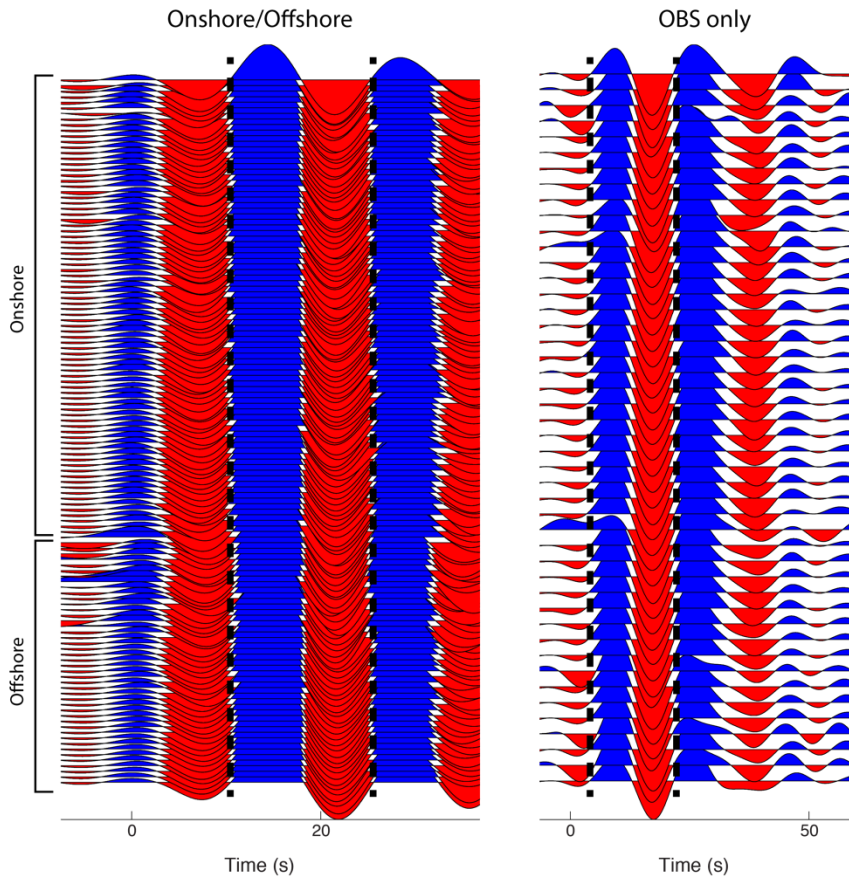


Figure S1: Examples of P-wave data. Traces are aligned using cross correlation and bandpass filtered between 12 and 33s. Black dashed lines denote the window used for cross correlations. (Left) Example of the combined onshore and offshore data. Stations are ordered by elevation. (Right) Example of arrivals at ocean bottom seismometer sites only.

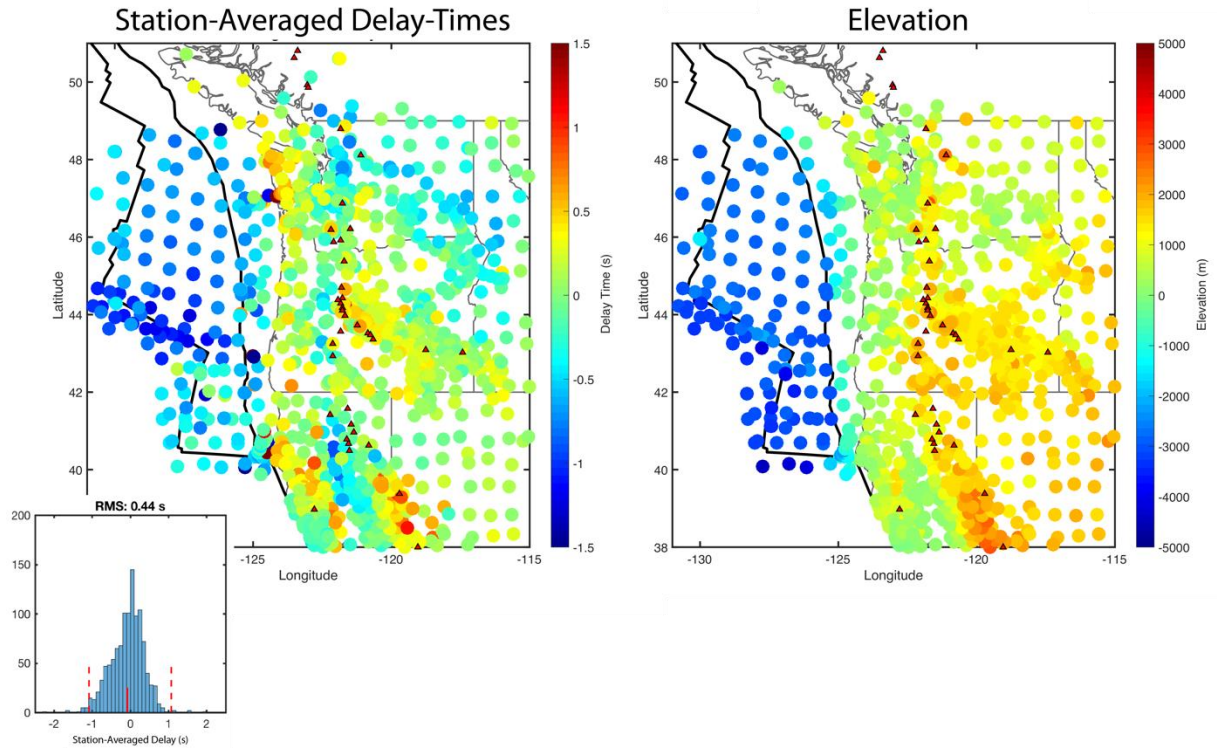


Figure S2: (Left) Average delay time for each station. Delay times are measured relative to a one-dimensional radial earth model. The RMS of the mean station delays is 0.44 s, with a mean of -0.08 s; see inset. The mean station delays exhibit a clear onshore-offshore signal that we attribute to differences in elevation, crustal thickness, and crustal velocity. (Right) Elevation at each station. Red triangles are locations of regional volcanoes.

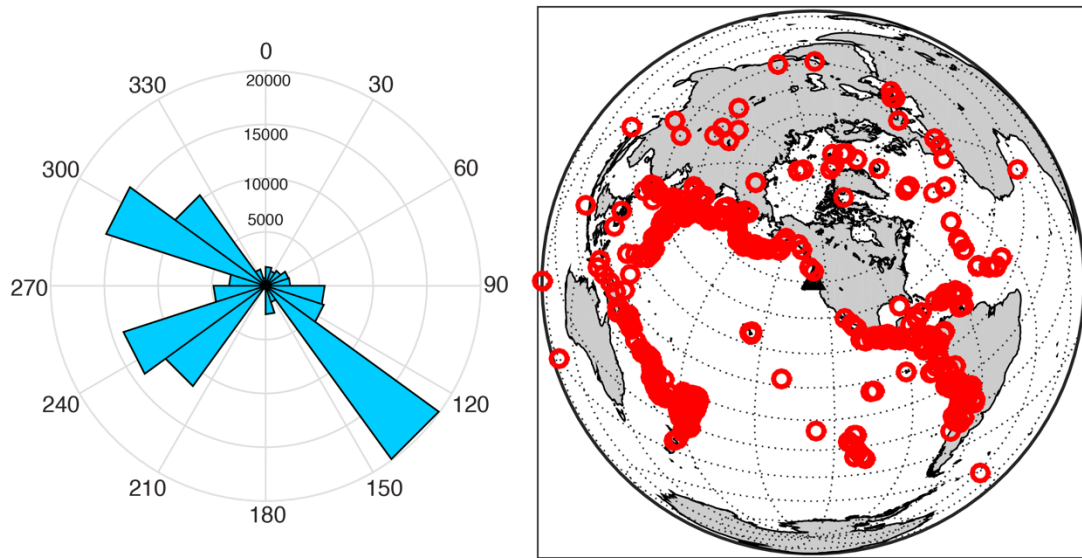


Figure S3: Event distribution. (Left) Rose plot showing the density of arrivals by back-azimuth. Arrivals are most abundant from the Japan, South America, and Tonga regions. (Right) Distribution of events used in this study. Red circles are events and the black triangle represents our study area.

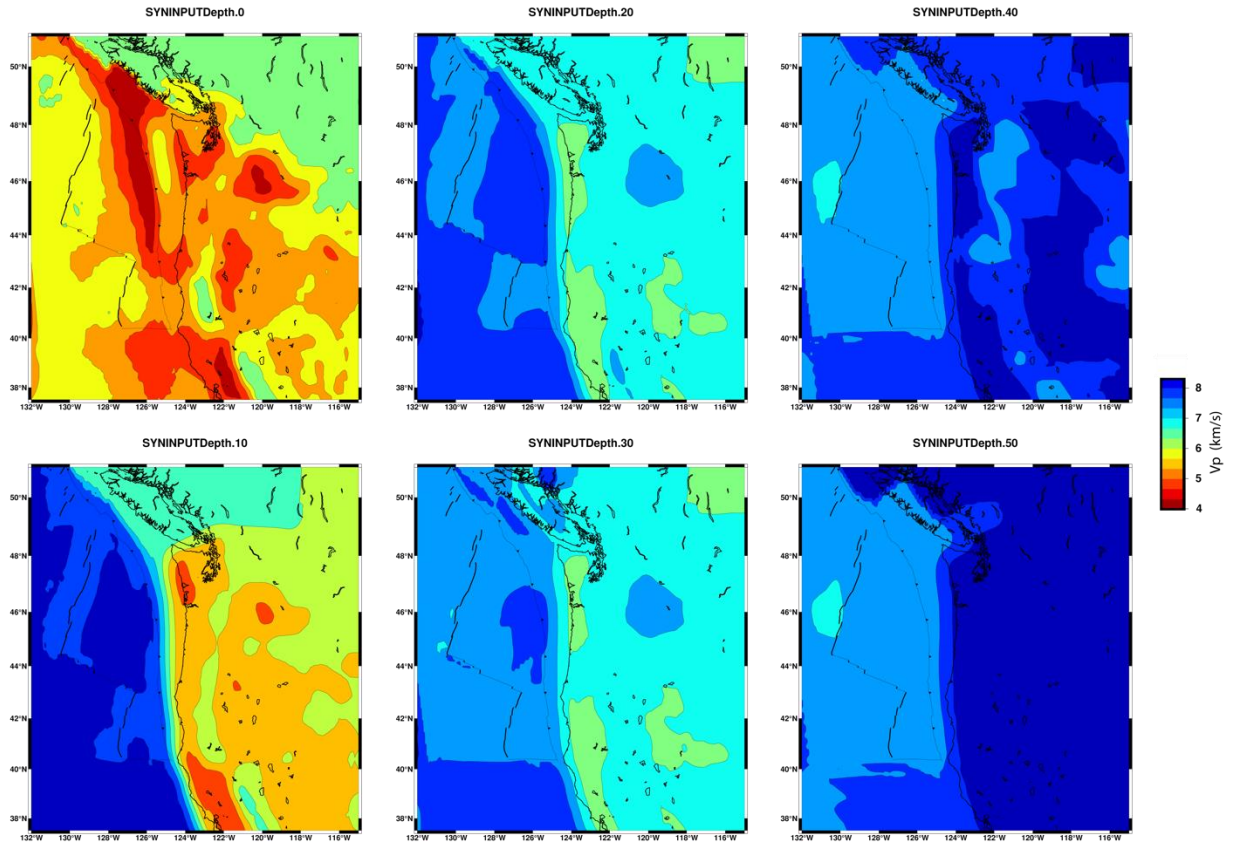


Figure S4: Depth slices through our *a priori* starting model of shallow structure (<50 km depth). This model is constructed by merging offshore (Bell et al., 2016) and onshore (Schmandt and Lin, 2014) surface wave models. Velocities are plotted as absolute velocities; manuscript shows perturbations relative to this starting model.

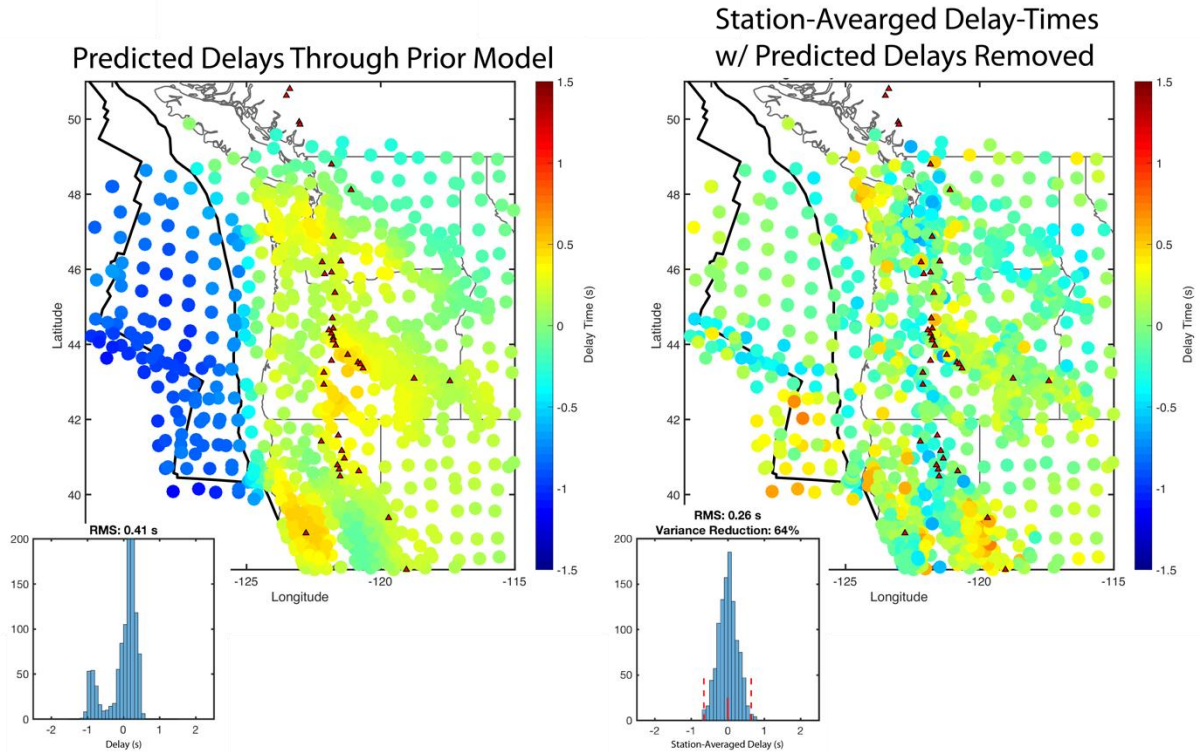


Figure S5: (Left) Predicted station-averaged delay-times through our *a priori* starting model (Supplementary Figure 4). Delays are calculated assuming vertical ray paths and are relative to the AK135 1D reference model. Predicted mean station delays have a bimodal distribution with a clear onshore-offshore signal. (Right) Station-averaged delay times after the predicted signal from the shallow starting model has been removed. Delay times for each event are demeaned after making the adjustment for the starting model. The *a priori* starting model reduces the variance of the station-averaged delay-times by 64% (RMS = 0.26 s) and removes the onshore-offshore signal.

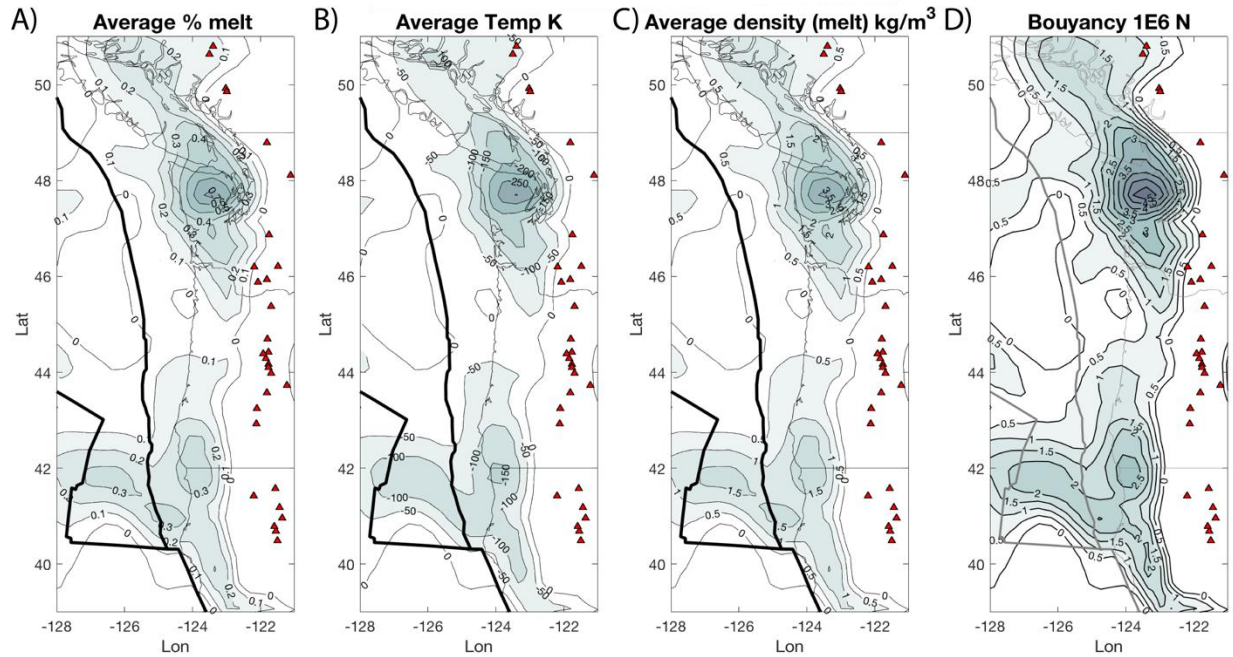


Figure S6: Map view plots of physical properties estimated from the vertical average (100 to 250 km depth) of low-velocity anomalies imaged in the sub-slab region (Figure 3a). All estimates assume that velocity anomalies are explained by partial melt and/or temperature variations (See Methods). (A) Partial melt variations only. (B) Temperature variations only. (C) Density variations due solely to partial melt. Density variations which include a contribution from temperature are larger. (D) Buoyancy per unit area due to changes in density for the partial melt only case. Buoyancy variations that include temperature variations are larger.

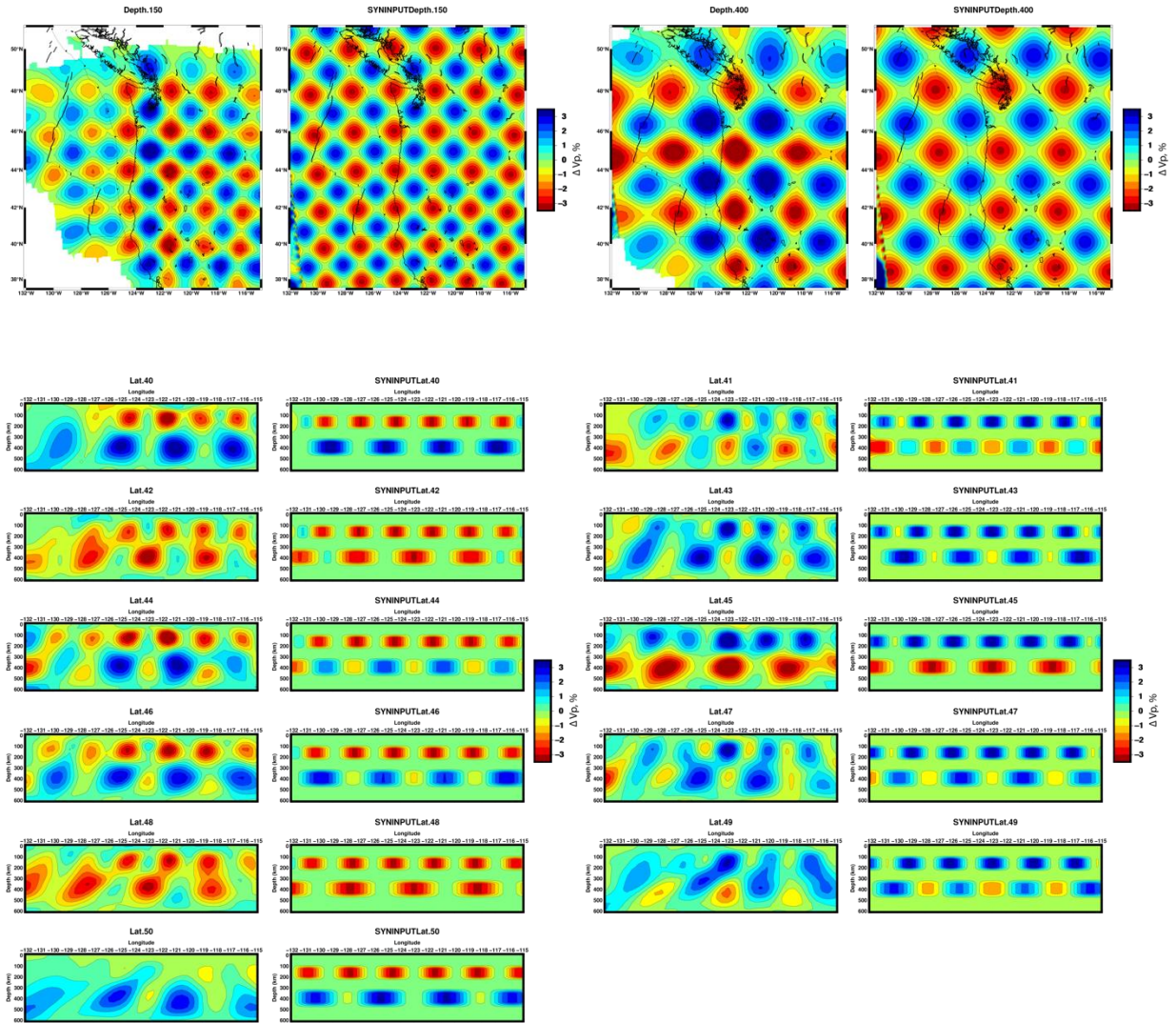


Figure S7: Synthetic checkerboard resolution tests. Sinusoidal high and low-velocity anomalies have a maximum amplitude of $\pm 3\%$ and are centered at depths of 150 km and 400 km. The vertical thicknesses of the anomalies are 100 km and 150 km, respectively. The upper layer has a lateral wavelength of 225 km and the lower layer a wavelength of 350 km. Tests show that we have good lateral resolution and amplitude recovery of the deepest anomalies. Shallower anomalies have reduced amplitude recovery in the offshore section. Vertical resolution is poorer due to sub-vertical ray paths.

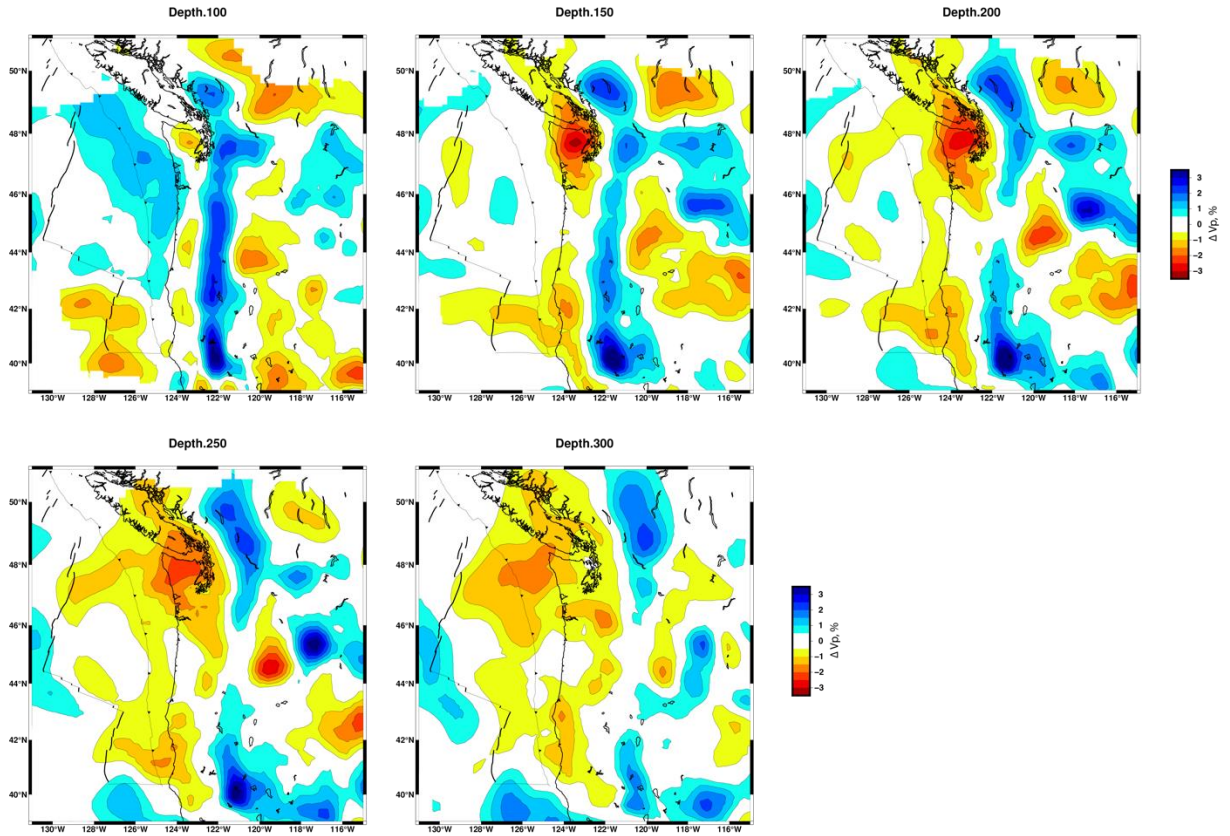


Figure S8: Depth slices through our preferred tomographic model at 50 km intervals.

APPENDIX C

CHAPTER IV SUPPORTING INFORMATION

This Supporting Information presented here contains 5 additional figures, supplementing the main text. The figures are as follows:

Figure S1: Map of inferred oceanic plate ages for the Juan de Fuca and Pacific plates.

Figure S2: Along-strike topographic relief.

Figure S3: Analysis of isotropic contributions from various models.

Figure S4: Along-strike variations in crustal thickness from various models.

Figure S5: Tradeoff curves from modeling results.

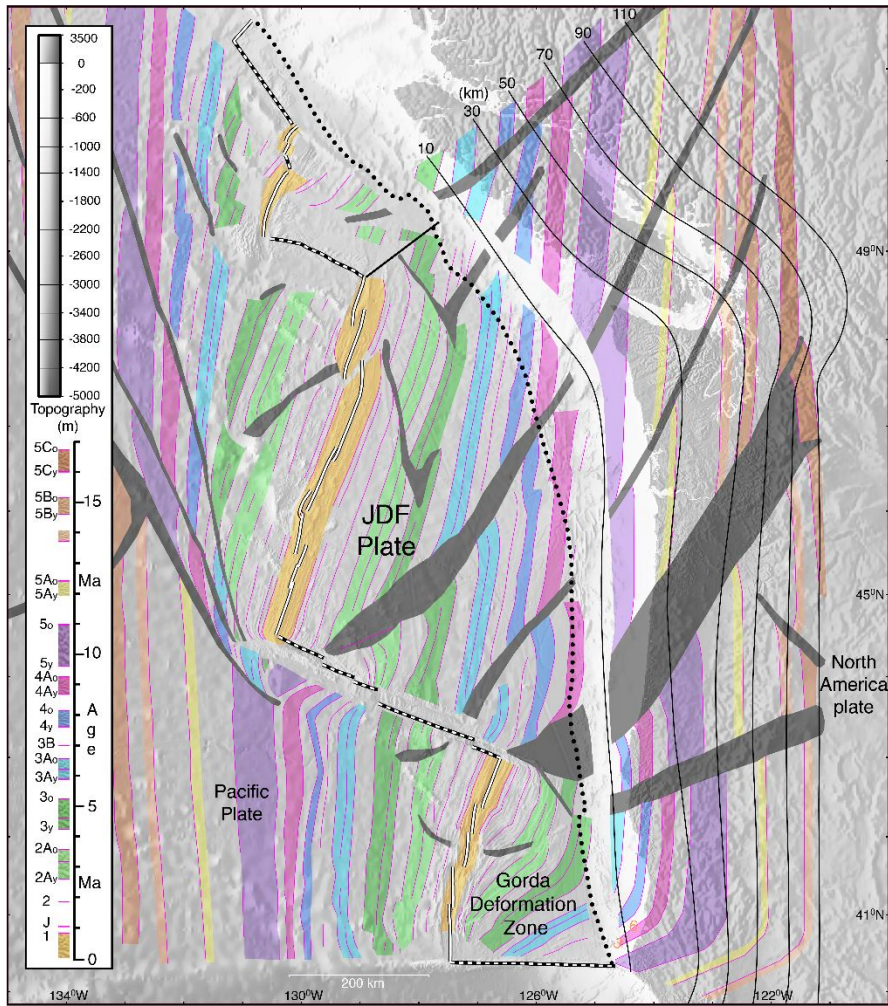


Figure S1: Map showing magnetic anomalies offshore and inferred anomalies of the down-going slab (Wilson, 2002). Figure modified from Nedimovic et al. (2009). Black lines represent slab interface contours.

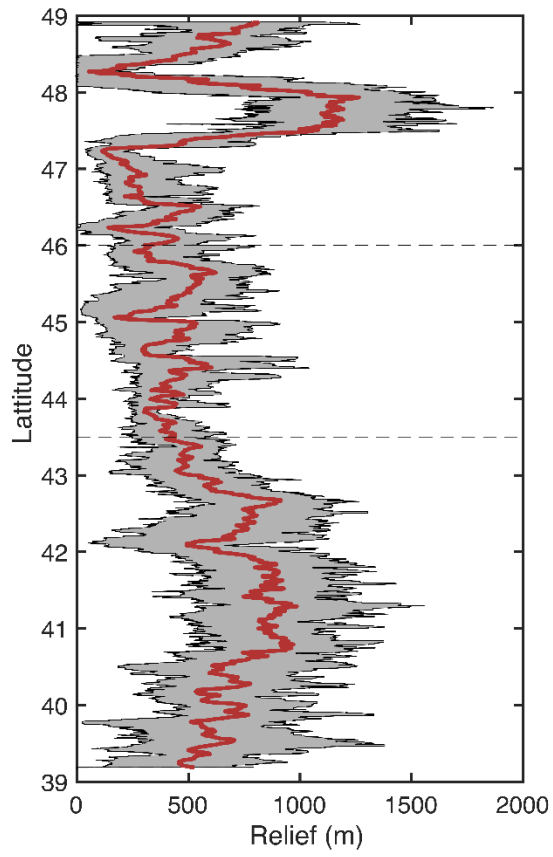


Figure S2: Topographic relief within the defined forearc swath. Relief is calculated within a radius of 2.5 km. Red line represents the average at a given latitude and the grey area represents the total range of observations.

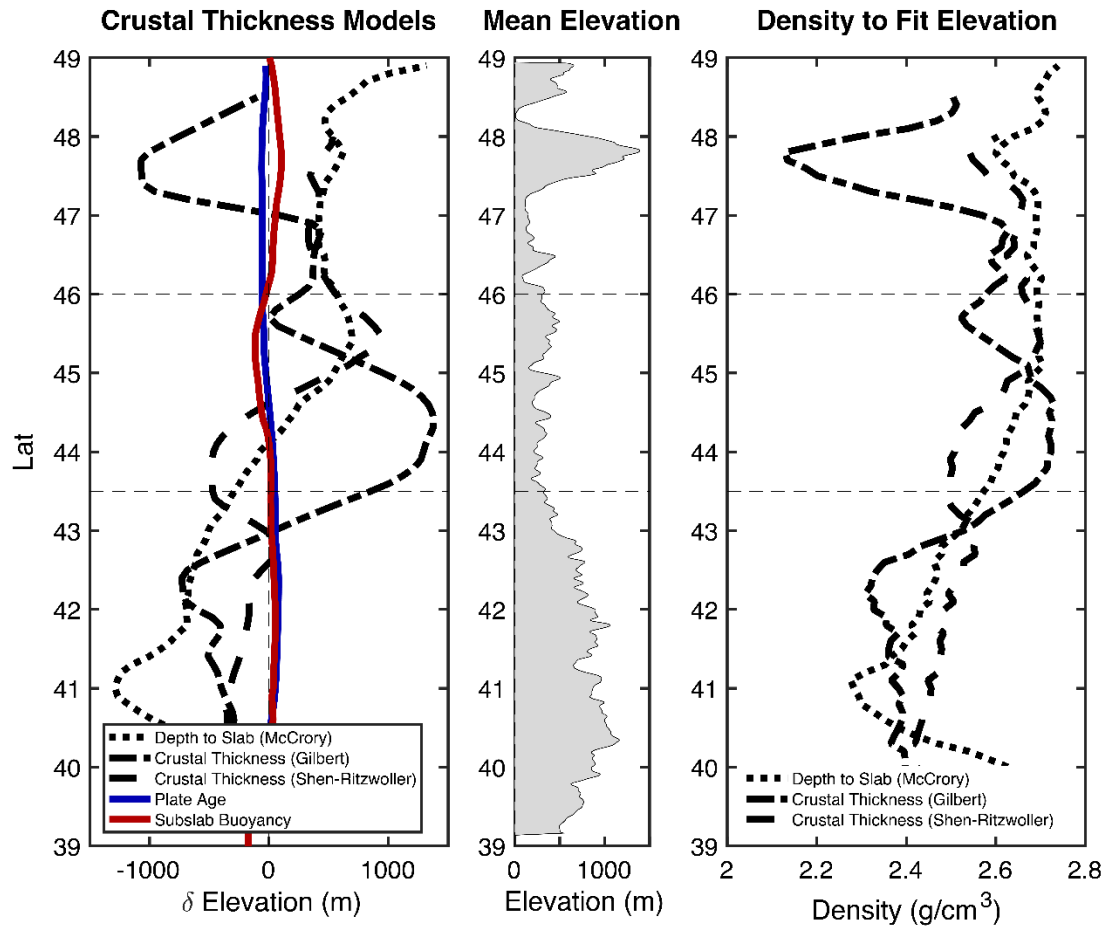


Figure S3: Along-strike profiles examining the isostatic contribution of the upper crust, down-going plate, and subslab asthenosphere. Left) relative changes to isostatically predicted forearc elevation due to variations in crustal thickness (three models in black), plate age (blue line), and subslab heterogeneity (red line). Crustal thickness models assume a constant density. Depth to slab model assumes crustal thickness is equivalent to mean elevation + slab depth. All measurements are defined for the forearc swath in Figure 1. Center) Mean elevation along strike within the swath. Right) Estimates of average crustal density needed to satisfy the elevation data using a given crustal thickness model. Estimates are much lower than average crustal density of 2.8 g/cm^3 .

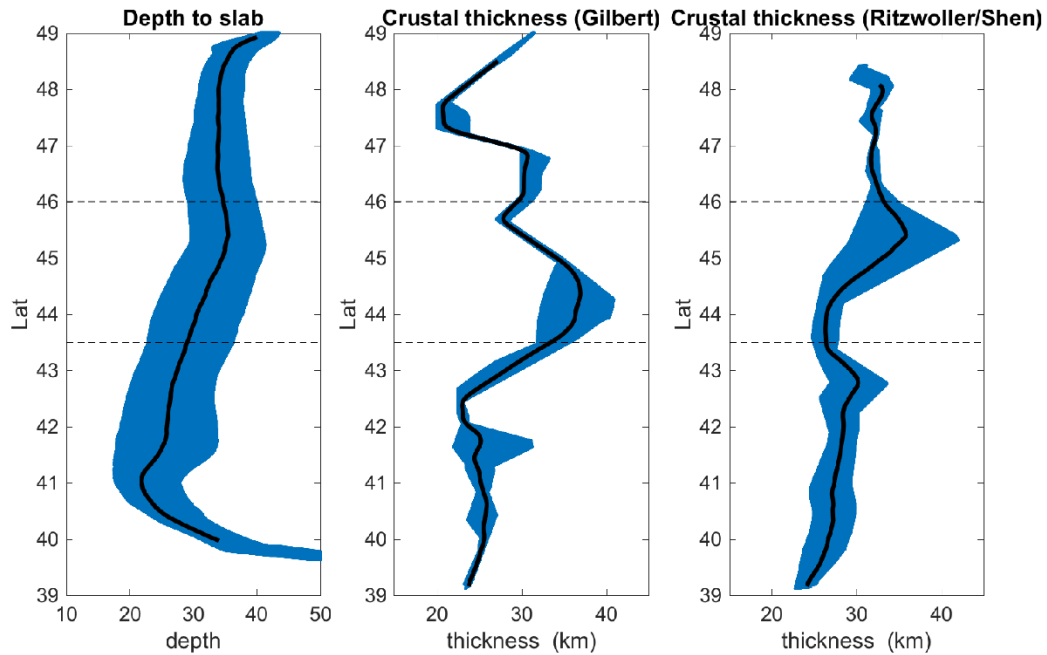


Figure S4: Estimates of crustal thickness beneath the defined forearc swath. Black lines represent the average values at a given latitude and the blue area is the range of values. Left) Depth to the slab interface (McCroly et al., 2012). Combined with topography above sea level this is treated as a maximum thickness. Center) Crustal thickness estimate from (Gilbert, 2012). Right) Crustal thickness estimated from (Shen et al., 2013).

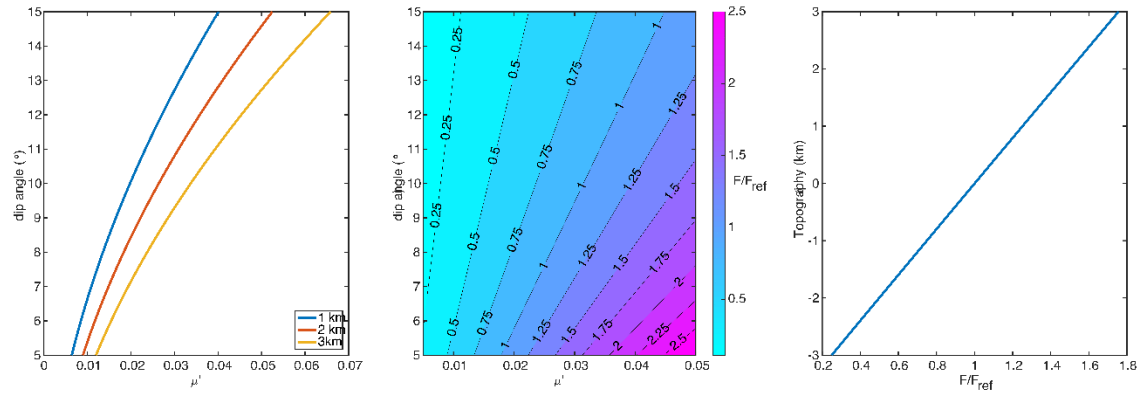


Figure S5: Left) Tradeoff between interface dip angle and the effective coefficient of friction (μ'). Colored lines represent various degrees of forearc relief above sea level and the interface dip - μ' values required to support it. Center) Plot showing how the normalized resistive shear force changes with variations of interface dip and μ' . Right) Relationship between the normalized resistive shear force and the topography above sea level which it can support. F is normalized assuming $\mu' = 0.03$, $\alpha = 1.5^\circ$, and $\beta = 11.5^\circ$.

APPENDIX D

CHAPTER V SUPPORTING INFORMATION

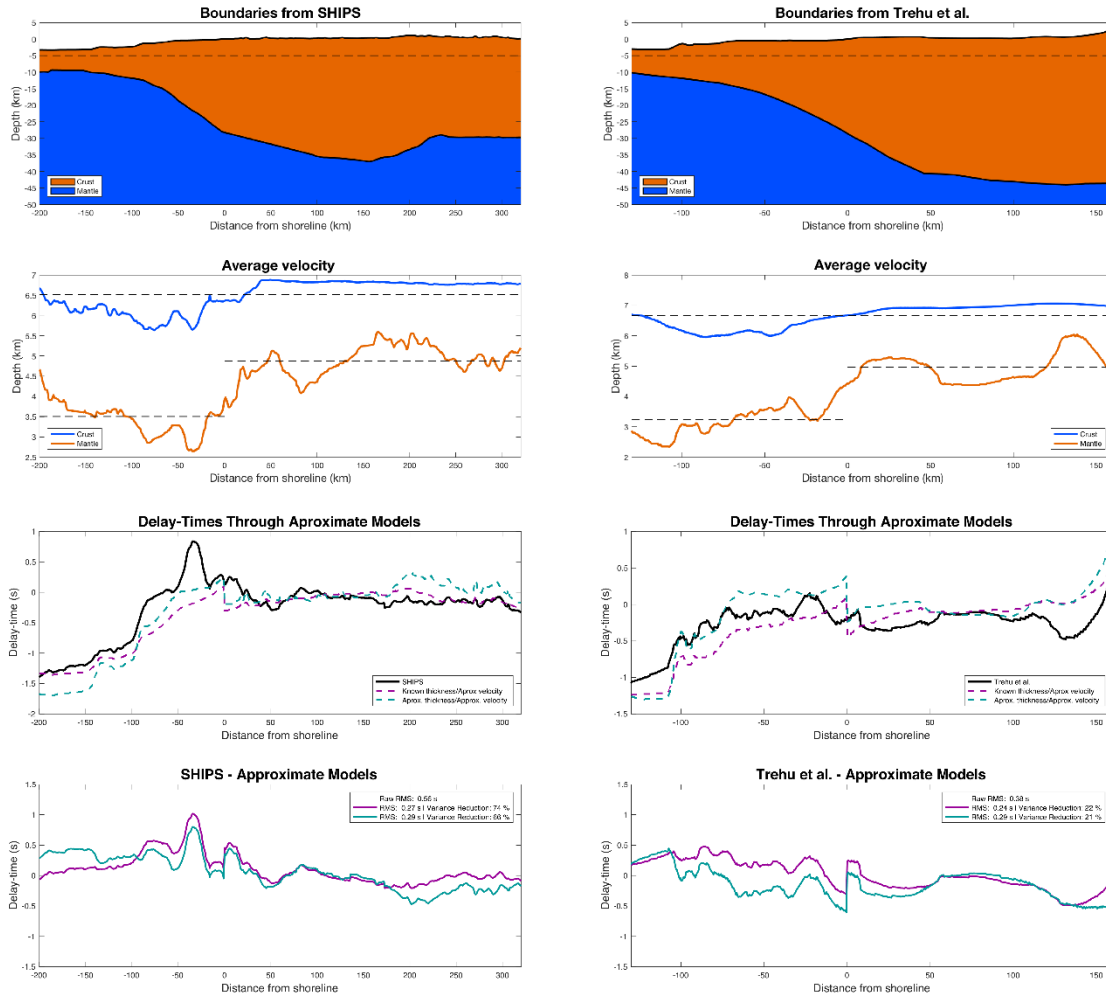


Figure S1: (Upper panels) Estimated crustal thickness from the 2D refraction models. (Upper-mid Panels) Plot of the average along profile velocity in the crust (brown) and mantle (blue). Black dotted lines represent the regional average for both regions where the crust has been separated into onshore and offshore sections. (Lower-mid panels) Black line represents the predicted delay times relative to AK135 through the model. Dashed purple line represents estimated delay times through a model where the crustal thickness is known (taken from the upper panel) and velocities are approximated for the entire crust and mantle layers. Dashed blue line represents estimated delay times through a model where crustal thickness is estimated using only elevation and isostasy. (Lower panel) Misfit between the predicted delay times from the full 2d model and the two simplified models using approximations for structure.

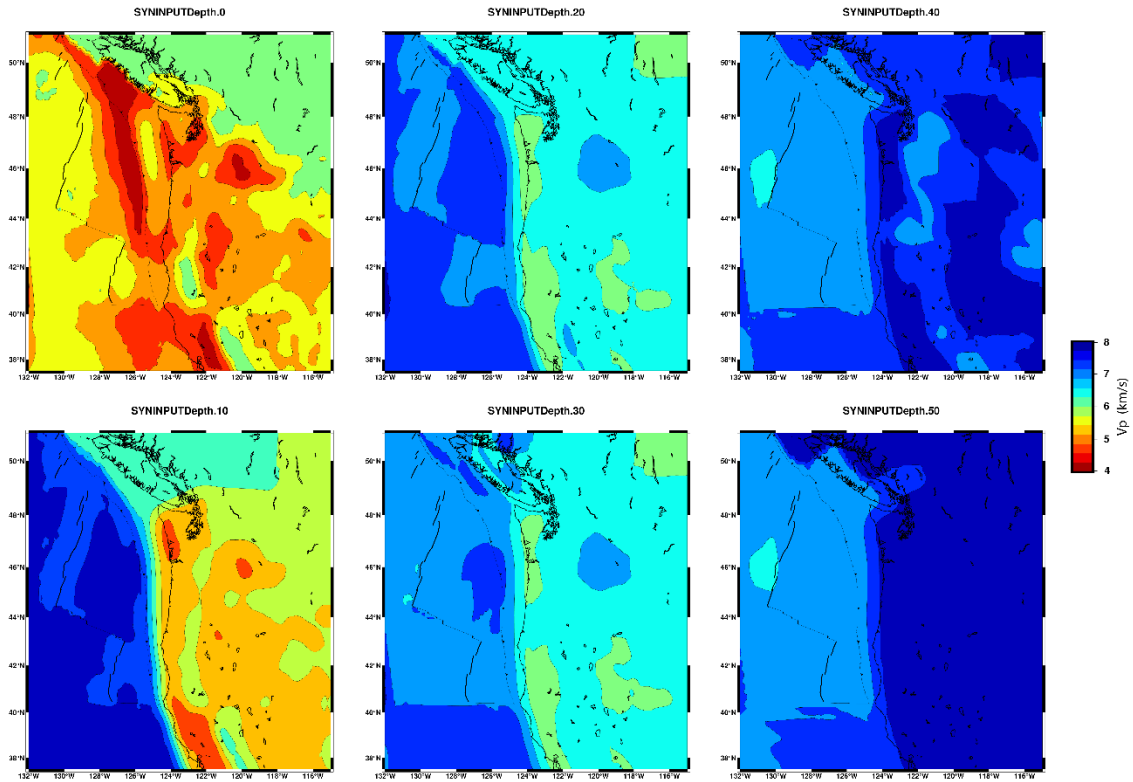


Figure S2: Depth slices through our a priori P-wave starting model of shallow structure (<50 km depth). This model is constructed by merging offshore (Bell et al., 2016) and onshore (Schmandt and Lin, 2014) surface wave models. Velocities are plotted as absolute velocities.

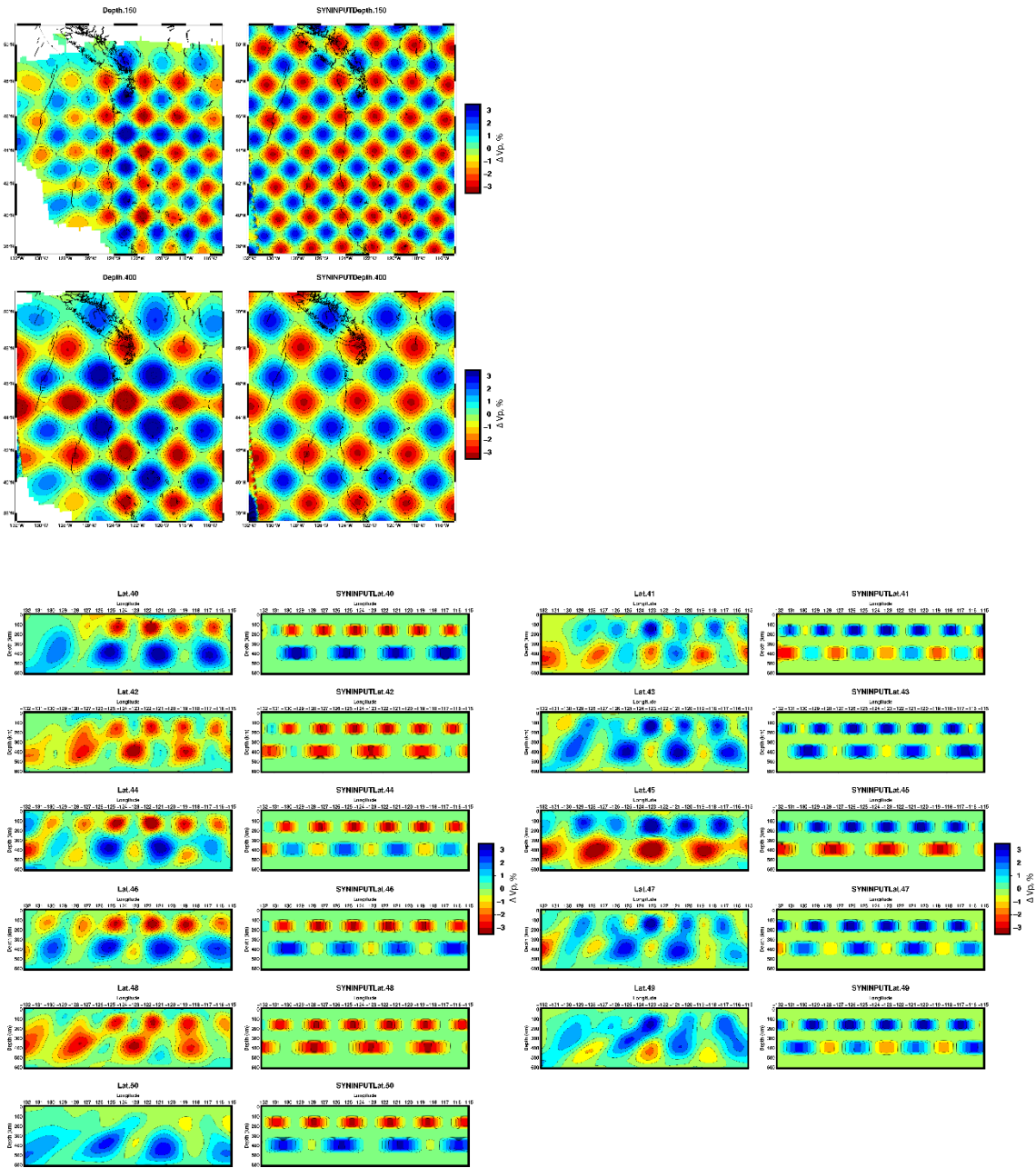


Figure S3: Synthetic checkerboard resolution tests. Sinusoidal high and low-velocity anomalies have a maximum amplitude of $\pm 3\%$ for P data and are centered at depths of 150 km and 400 km. The vertical thicknesses of the anomalies are 100 km and 150 km, respectively. The upper layer has a lateral wavelength of 225 km and the lower layer a wavelength of 350 km. Tests show that we have good lateral resolution and amplitude recovery of the deepest anomalies. Shallower anomalies have reduced amplitude recovery in the offshore section. Vertical resolution is poorer due to sub-vertical ray paths.

REFERENCES CITED

Chapter II

- Bonnin, M., Barruol, G., and Bokelmann, G.H., 2010, Upper mantle deformation beneath the North American–Pacific plate boundary in California from SKS splitting: *Journal of Geophysical Research*, v. 115, B04306, doi: 10.1029 /2009JB006438.
- Bowman, J.R., and Ando, M., 1987, Shear-wave splitting in the upper-mantle wedge above the Tonga subduction zone: *Geophysical Journal International*, v. 88, p. 25–41, doi:10.1111/j.1365-246X.1987.tb01367.x.
- Chaytor, J.D., Goldfinger, C., Dziak, R.P., and Fox, C.G., 2004, Active deformation of the Gorda plate: Constraining deformation models with new geophysical data: *Geology*, v. 32, p. 353–356, doi:10.1130/G20178.2.
- Currie, C.A., Cassidy, J.F., Hyndman, R.D., and Bostock, M.G., 2004, Shear wave anisotropy beneath the Cascadia subduction zone and western North American craton: *Geophysical Journal International*, v. 157, p. 341–353, doi: 10.1111 /j .1365 -246X .2004 .02175.x.
- DeMets, C., Gordon, R.G., and Argus, D.F., 2010, Geologically current plate motions: *Geophysical Journal International*, v. 181, p. 1–80, doi:10.1111/j .1365 -246X .2009 .04491.x.
- Eakin, C.M., Obrebski, M., Allen, R.M., Boyarko, D.C., Brudzinski, M.R., and Porritt, R., 2010, Seismic anisotropy beneath Cascadia and the Mendocino triple junction: Interaction of the subducting slab with mantle flow: *Earth and Planetary Science Letters*, v. 297, p. 627–632, doi:10.1016/j .epsl .2010 .07.015.
- Faccenda, M., and Capitanio, F.A., 2012, Development of mantle seismic anisotropy during subduction-induced 3-D flow: *Geophysical Research Letters*, v. 39, L11305, doi:10.1029/2012GL051988.
- Ghorbani, P., Nabelek, J., and Braunmiller, J., 2015, Gorda and Juan de Fuca plate seismicity recorded by the Cascadia Initiative and Blanco transform fault zone seismic arrays [abs.]: *Seismological Research Letters*, v. 86, p. 682, doi:10.1785/0220150017.
- Lynner, C., and Long, M.D., 2014, Testing models of sub-slab anisotropy using a global compilation of source-side shear wave splitting data: *Journal of Geophysical Research*, v. 119, p. 7226–7244, doi:10.1002/2014JB010983.
- McCrory, P.A., Blair, J.L., Waldhauser, F., and Oppenheimer, D.H., 2012, Juan de Fuca slab geometry and its relation to Wadati-Benioff zone seismicity: *Journal of Geophysical Research*, v. 117, B09306, doi:10.1029/2012JB009407.

- Mosher, S.G., Audet, P., and L'Heureux, I., 2014, Seismic evidence for rotating mantle flow around subducting slab edge associated with oceanic microplate capture: *Geophysical Research Letters*, v. 41, p. 4548–4553, doi: 10.1002/2014GL060630.
- Nedimović, M.R., Bohnenstiehl, D.R., Carbotte, S.M., Canales, J.P., and Dziak, R.P., 2009, Faulting and hydration of the Juan de Fuca plate system: *Earth and Planetary Science Letters*, v. 284, p. 94–102, doi:10.1016/j.epsl.2009.04.013.
- Restivo, A., and Helffrich, G., 1999, Teleseismic shear wave splitting measurements in noisy environments: *Geophysical Journal International*, v. 137, p. 821–830, doi:10.1046/j.1365-246x.1999.00845.x.
- Silver, P.G., and Chan, W.W., 1991, Shear wave splitting and subcontinental mantle deformation: *Journal of Geophysical Research*, v. 96, p. 16,429–16,454, doi: 10.1029/91JB00899.
- Sumy, D.F., Lodewyk, J.A., Woodward, R.L., and Evers, B., 2015, Ocean-bottom seismograph performance during the Cascadia Initiative: *Seismological Research Letters*, v. 86, doi:10.1785/0220150110.
- Toomey, D.R., et al., 2014, The Cascadia initiative: A sea change in seismological studies of subduction zones: *Oceanography*, v. 27, p. 138–150, doi:10.5670/oceanog.2014.49.
- VanderBeek, B.P., Toomey, D.R., Hooft, E.E.E., and Wilcock, W.S.D., 2014, Segment-scale seismic structure of slow-, intermediate-, and fast-spreading mid-ocean ridges: Constraints on the origin of ridge segmentation and the geometry of shallow mantle flow: *American Geophysical Union Fall Meeting*, abs. V23E-07.
- Vecsey, L., Plomerová, J., and Babuška, V., 2008, Shear-wave splitting measurements—Problems and solutions: *Tectonophysics*, v. 462, p. 178–196, doi: 10.1016/j.tecto.2008.01.021.
- Wang, K., He, J., and Davis, E.E., 1997, Transform push, oblique subduction resistance, and intraplate stress of the Juan de Fuca plate: *Journal of Geophysical Research*, v. 102, no. B1, p. 661–674, doi:10.1029/96JB03114.
- Wilson, D.S., 1988, Tectonic history of the Juan de Fuca ridge over the last 40 million years: *Journal of Geophysical Research*, v. 93, p. 11,863–11,876, doi: 10.1029/JB093iB10p11863.
- Wilson, D.S., 1993, Confidence intervals for motion and deformation of the Juan de Fuca plate: *Journal of Geophysical Research*, v. 98, p. 16,053–16,071, doi: 10.1029/93JB01227.

- Wolfe, C.J., and Silver, P.G., 1998, Seismic anisotropy of oceanic upper mantle: Shear wave splitting methodologies and observations: *Journal of Geophysical Research*, v. 103, p. 749–771, doi:10.1029/97JB02023.
- Wüstefeld, A., Bokelmann, G., Zaroli, C., and Barruol, G., 2008, SplitLab: A shear-wave splitting environment in Matlab: *Computers & Geosciences*, v. 34, p. 515–528, doi:10.1016/j.cageo.2007.08.002.
- Zandt, G., and Humphreys, E., 2008, Toroidal mantle flow through the western US slab window: *Geology*, v. 36, p. 295–298, doi:10.1130/G24611A.1.

Chapter III

- Allmann, B. P., & Shearer, P. M. (2009). Global variations of stress drop for moderate to large earthquakes. *Journal of Geophysical Research: Solid Earth*, 114(1), 1–22. <https://doi.org/10.1029/2008JB005821>
- Ando, M. (1975). Source mechanisms and tectonic significance of historical earthquakes along the nankai trough, Japan. *Tectonophysics*, 27(2), 119–140. [https://doi.org/10.1016/0040-1951\(75\)90102-X](https://doi.org/10.1016/0040-1951(75)90102-X)
- Audet, P., Bostock, M. G., Christensen, N. I., & Peacock, S. M. (2009). Seismic evidence for overpressured subducted oceanic crust and megathrust fault sealing. *Nature*, 457(7225), 76–78. <https://doi.org/10.1038/nature07650>
- Bell, S., Ruan, Y., & Forsyth, D. W. (2016). Ridge asymmetry and deep aqueous alteration at the trench observed from Rayleigh wave tomography of the Juan de Fuca plate. *Journal of Geophysical Research: Solid Earth*, 121(10), 7298–7321. <https://doi.org/10.1002/2016JB012990>
- Bezada, M. J., Humphreys, E. D., Toomey, D. R., Harnafi, M., Dávila, J. M., & Gallart, J. (2013). Evidence for slab rollback in westernmost Mediterranean from improved upper mantle imaging. *Earth and Planetary Science Letters*, 368(Complete), 51–60. <https://doi.org/10.1016/j.epsl.2013.02.024>
- Bodmer, M., Toomey, D. R., Hooft, E. E., Nábelek, J., & Braunmiller, J. (2015). Seismic anisotropy beneath the Juan de Fuca plate system: Evidence for heterogeneous mantle flow. *Geology*, 43(12), 1095–1098. <https://doi.org/10.1130/G37181.1>
- Brocher, T. M. (2005). Empirical Relations between Elastic Wavespeeds and Density in the Earth's Crust. *Bulletin of the Seismological Society of America*, 95(6), 2081–2092. <https://doi.org/10.1785/0120050077>
- Brudzinski, M. R., & Allen, R. M. (2007). Segmentation in episodic tremor and slip all along Cascadia. *Geology*, 35(10), 907. <https://doi.org/10.1130/G23740A.1>
- Burgette, R. J., Weldon, R. J., & Schmidt, D. A. (2009). Interseismic uplift rates for western Oregon and along-strike variation in locking on the Cascadia subduction zone. *Journal of Geophysical Research: Solid Earth*, 114(1). <https://doi.org/10.1029/2008JB005679>

- Byrnes, J. S., Toomey, D. R., Hooft, E. E. E., Nábělek, J., & Braunmiller, J. (2017). Mantle dynamics beneath the discrete and diffuse plate boundaries of the Juan de Fuca plate: Results from Cascadia Initiative body wave tomography. *Geochemistry, Geophysics, Geosystems*, *18*(8), 2906–2929. <https://doi.org/10.1002/2017GC006980>
- Chadwick, J., Keller, R., Kamenov, G., Yogodzinski, G., & Lupton, J. (2014). The Cobb hot spot: HIMU-DMM mixing and melting controlled by a progressively thinning lithospheric lid. *Geochemistry, Geophysics, Geosystems*, *15*(8), 3107–3122. <https://doi.org/10.1002/2014GC005334>
- Chaytor, J. D., Goldfinger, C., Dziak, R. P., & Fox, C. G. (2004). Active deformation of the Gorda plate: Constraining deformation models with new geophysical data. *Geology*, *32*(4), 353–356. <https://doi.org/10.1130/G20178.2>
- Chen, C., Zhao, D., & Wu, S. (2015). Tomographic imaging of the Cascadia subduction zone: Constraints on the Juan de Fuca slab. *Tectonophysics*, *647*, 73–88. <https://doi.org/10.1016/j.tecto.2015.02.012>
- Cloos, M. (1992). Thrust-type subduction-zone earthquakes and seamount asperities: A physical model for seismic rupture. *Geology*, *20*(7), 601. [https://doi.org/10.1130/0091-7613\(1992\)020<0601:TTSZEA>2.3.CO;2](https://doi.org/10.1130/0091-7613(1992)020<0601:TTSZEA>2.3.CO;2)
- Conder, J. A., Forsyth, D. W., & Parmentier, E. M. (2002). Asthenospheric flow and asymmetry of the East Pacific Rise, MELT area. *Journal of Geophysical Research: Solid Earth*, *107*(B12), ETG 8-1-ETG 8-13. <https://doi.org/10.1029/2001JB000807>
- Courtillot, V., Davaille, A., Besse, J., & Stock, J. (2003). Three distinct types of hotspots in the Earth's mantle TL - 205. *Earth and Planetary Science Letters*, *205*, 295–308. [https://doi.org/10.1016/S0012-821X\(02\)01048-8](https://doi.org/10.1016/S0012-821X(02)01048-8)
- DeMets, C., Gordon, R. G., & Argus, D. F. (2010). Geologically current plate motions. *Geophysical Journal International*, *181*(1), 1–80. <https://doi.org/10.1111/j.1365-246X.2009.04491.x>
- Eilon, Z. C., & Abers, G. A. (2017). High seismic attenuation at a mid-ocean ridge reveals the distribution of deep melt. *Science Advances*, *3*(May), e1602829. <https://doi.org/10.1126/sciadv.1602829>
- Gao, H. (2018). Three-dimensional variations of the slab geometry correlate with earthquake distributions at the Cascadia subduction system. *Nature Communications*, (2018), 1–8. <https://doi.org/10.1038/s41467-018-03655-5>
- Goldfinger, C., Nelson, C. H., Morey, A. E., Joel E., J., Patton, J., Karabanov, E., et al. (2012). Turbidite Event History — Methods and Implications for Holocene Paleoseismicity of the Cascadia Subduction Zone. *U.S. Geological Survey Professional Paper*, 1661.
- Hammond, W. C., & Humphreys, E. D. (2000). Upper mantle seismic wave velocity: Effects of realistic partial melt geometries. *Journal of Geophysical Research: Solid Earth*, *105*(B5), 10975–10986. <https://doi.org/10.1029/2000JB900041>

- Hammond, W. C., & Toomey, D. R. (2003). Seismic velocity anisotropy and heterogeneity beneath the Mantle Electromagnetic and Tomography Experiment (MELT) region of the East Pacific Rise from analysis of P and S body waves. *J. Geophys. Res.*, *108*(B4), 2176. <https://doi.org/10.1029/2002jb001789>
- Hawley, W. B., Allen, R. M., & Richards, M. A. (2016). Tomography reveals buoyant asthenosphere accumulating beneath the Juan de Fuca plate. *Science (New York, N.Y.)*, *353*(6306), 1406–1408. <https://doi.org/10.1126/science.aad8104>
- Heaton, T. H., & Hartzell, S. H. (1987). Earthquake hazards on the Cascadia subduction zone. *Science (New York, N.Y.)*, *236*(4798), 162–168. <https://doi.org/10.1126/science.236.4798.162>
- Honda, S., Morishige, M., & Orihashi, Y. (2007). Sinking hot anomaly trapped at the 410 km discontinuity near the Honshu subduction zone, Japan. *Earth and Planetary Science Letters*, *261*(3–4), 565–577. <https://doi.org/10.1016/j.epsl.2007.07.028>
- Hooft, E. E. E., & Detrick, R. S. (1995). Relationship between axial morphology, crustal thickness, and mantle temperature along the Juan-de-Fuca and Gorda Ridges. *Journal of Geophysical Research-Solid Earth*, *100*(B11), 22499–22508. <https://doi.org/10.1029/95JB02502>
- Huang, Z., Zhao, D., Hasegawa, A., Umino, N., Park, J. H., & Kang, I. B. (2013). Aseismic deep subduction of the Philippine Sea plate and slab window. *Journal of Asian Earth Sciences*, *75*, 82–94. <https://doi.org/10.1016/j.jseaes.2013.07.002>
- Jackson, D. D. (1979). The use of a priori data to resolve non-uniqueness in linear inversion. *Geophysical Journal International*, *57*(1), 137–157. <https://doi.org/10.1111/j.1365-246X.1979.tb03777.x>
- Jha, K., Parmentier, E. M., & Phipps Morgan, J. (1994). The role of mantle-depletion and melt-retention buoyancy in spreading-center segmentation. *Earth and Planetary Science Letters*, *125*(1–4), 221–234. [https://doi.org/10.1016/0012-821X\(94\)90217-8](https://doi.org/10.1016/0012-821X(94)90217-8)
- Karato, S., Jung, H., Katayama, I., & Skemer, P. (2008). Geodynamic significance of seismic anisotropy of the upper mantle: New insights from laboratory studies. *Annual Review of Earth and Planetary Sciences*, *36*(1), 59–95. <https://doi.org/10.1146/annurev.earth.36.031207.124120>
- Kelleher, J. a. (1972). Rupture zones of large South American earthquakes and some predictions. *Journal of Geophysical Research*, *77*(11), 2087. <https://doi.org/10.1029/JB077i011p02087>
- Kennett, B. L. N., Engdahl, E. R., & Buland, R. (1995). Constraints on seismic velocities in the Earth from traveltimes. *Geophysical Journal International*, *122*(1), 108–124. <https://doi.org/10.1111/j.1365-246X.1995.tb03540.x>
- Kodaira, S., Kato, A., & Park, J. (2004). High Pore Fluid Pressure May Cause Silent Slip in the Nankai Trough High Pore Fluid Pressure May Cause Silent Slip in the Nankai Trough. *Science*, *304*(May), 1295–1299. <https://doi.org/10.1126/science.1096535>

- Martin-Short, R., Allen, R. M., Bastow, I. D., Totten, E., & Richards, M. A. (2015). Mantle flow geometry from ridge to trench beneath the Gorda-Juan de Fuca plate system. *Nature Geoscience*, 8(12), 965–968. <https://doi.org/10.1038/ngeo2569>
- McCrary, P. A., Blair, J. L., Waldhauser, F., & Oppenheimer, D. H. (2012). Juan de Fuca slab geometry and its relation to Wadati-Benioff zone seismicity. *Journal of Geophysical Research: Solid Earth*, 117(9), 1–23. <https://doi.org/10.1029/2012JB009407>
- Mercier, J. P., Bostock, M. G., Cassidy, J. F., Dueker, K., Gaherty, J. B., Garnero, E. J., et al. (2009). Body-wave tomography of western Canada. *Tectonophysics*, 475(3–4), 480–492. <https://doi.org/10.1016/j.tecto.2009.05.030>
- Nishikawa, T., & Ide, S. (2014). Earthquake size distribution in subduction zones linked to slab buoyancy. *Nature Geoscience*, 7(12), 904–908. <https://doi.org/10.1038/ngeo2279>
- Obara, K. (2002). Nonvolcanic deep tremor associated with subduction in southwest Japan. *Science*, 296(5573), 1679–1681. <https://doi.org/10.1126/science.1070378>
- Portner, D. E., Beck, S., Zandt, G., & Scire, A. (2017). The nature of subslab slow velocity anomalies beneath South America. *Geophysical Research Letters*, 44(10), 4747–4755. <https://doi.org/10.1002/2017GL073106>
- Riddihough, R. (1984). Recent movements of the Juan de Fuca plate system. *Journal of Geophysical Research: Solid Earth*, 89(B8), 6980–6994. <https://doi.org/10.1029/JB089iB08p06980>
- Roth, J. B., Fouch, M. J., James, D. E., & Carlson, R. W. (2008). Three-dimensional seismic velocity structure of the northwestern United States. *Geophysical Research Letters*, 35(15), 1–6. <https://doi.org/10.1029/2008GL034669>
- Ruff, L. J. (1989). Do trench sediments affect great earthquake occurrence in subduction zones? *Pure and Applied Geophysics PAGEOPH*, 129(1–2), 263–282. <https://doi.org/10.1007/BF00874629>
- Schmalzle, G. M., McCaffrey, R., & Creager, K. C. (2014). Central Cascadia subduction zone creep. *Geochemistry, Geophysics, Geosystems*, 15(4), 1515–1532. <https://doi.org/10.1002/2013GC005172>
- Schmandt, B., & Humphreys, E. (2010a). Complex subduction and small-scale convection revealed by body-wave tomography of the western United States upper mantle. *Earth and Planetary Science Letters*, 297(3–4), 435–445. <https://doi.org/10.1016/j.epsl.2010.06.047>
- Schmandt, B., & Humphreys, E. (2010b). Seismic heterogeneity and small-scale convection in the southern California upper mantle. *Geochemistry, Geophysics, Geosystems*, 11(5), 1–19. <https://doi.org/10.1029/2010GC003042>
- Schmandt, B., & Lin, F. (2014). P and S wave tomography of the mantle beneath the United States. *Geophysical Research Letters*, 41(18), 6342–6349. <https://doi.org/10.1002/2014GL061231>

- Scholz, C. H. (2015). On the stress dependence of the earthquake b-value. *Geophysical Research Letters*, 10964. <https://doi.org/10.1002/2014GL062863>
- Sleep, N. H. (1990). Hotspots and mantle plumes: some phenomenology. *Journal of Geophysical Research*, 95(B5), 6715–6736. <https://doi.org/10.1029/JB095iB05p06715>
- Spada, M., Tormann, T., Wiemer, S., & Enescu, B. (2013). Generic dependence of the frequency-size distribution of earthquakes on depth and its relation to the strength profile of the crust. *Geophysical Research Letters*, 40(4), 709–714. <https://doi.org/10.1029/2012GL054198>
- Tarantola, A., & Valette, B. (1982). Generalized nonlinear inverse problems solved using the least squares criterion. *Reviews of Geophysics*, 20(2), 219. <https://doi.org/10.1029/RG020i002p00219>
- Thatcher, W. (1990). Order and diversity in the modes of Circum-Pacific Earthquake recurrence. *Journal of Geophysical Research*, 95(B3), 2609. <https://doi.org/10.1029/JB095iB03p02609>
- Toomey, D., Allen, R., Barclay, A., Bell, S., Bromirski, P., Carlson, R., et al. (2014). The Cascadia Initiative: A sea change in seismological studies of subduction zones. *Oceanography*, 27(2), 138–150. <https://doi.org/10.5670/oceanog.2014.49>
- Toomey, D. R., Solomon, S. C., & Purdy, G. M. (1994). Tomographic imaging of the shallow crustal structure of the East Pacific Rise at 9°30'N. *Journal of Geophysical Research*, 99(B12), 24135–24157. <https://doi.org/10.1029/94JB01942>
- Toomey, D. R., Wilcock, W. S. D., Conder, J. A., Forsyth, D. W., Blundy, J. D., Parmentier, E. M., & Hammond, W. C. (2002). Asymmetric mantle dynamics in the MELT region of the East Pacific Rise. *Earth and Planetary Science Letters*, 200(3–4), 287–295. [https://doi.org/10.1016/S0012-821X\(02\)00655-6](https://doi.org/10.1016/S0012-821X(02)00655-6)
- VanDecar, J. C., & Crosson, R. S. (1990). Determination of teleseismic relative phase arrival times using multi-channel cross-correlation and least squares. *Bulletin of the Seismological Society of America*, 80(1), 150–169. Retrieved from <http://www.bssaonline.org/content/80/1/150.short>
- Wang, K., & He, J. (1999). Mechanics of low-stress forearcs: Nankai and Cascadia. *Journal of Geophysical Research*, 104(B7), 15191. <https://doi.org/10.1029/1999JB900103>
- Wang, K., & Suyehiro, K. (1999). How does plate coupling affect crustal stresses in Northeast and Southwest Japan? *Geophysical Research Letters*, 26(15), 2307–2310. <https://doi.org/10.1029/1999GL900528>
- Wang, K., Mulder, T., Rogers, G. C., & Hyndman, R. D. (1995). Case for very low coupling stress on the Cascadia subduction Fault. *Journal of Geophysical Research*, 100(B7), 12907–12918. <https://doi.org/10.1029/95JB00516>
- Wang, K., He, J., & Davis, E. E. (1997). Transform push, oblique subduction resistance, and intraplate stress of the Juan de Fuca Plate. *Journal of Geophysical Research*, 102(B1), 661. <https://doi.org/10.1029/96JB03114>

- Wells, R. E., Blakely, R. J., Wech, A. G., McCrory, P. A., & Michael, A. (2017). Cascadia subduction tremor muted by crustal faults. *Geology*, *45*(6), 515–518. <https://doi.org/10.1130/G38835.1>
- Wilson, D. S. (1986). A kinematic model for the Gorda Deformation Zone as a diffuse southern boundary of the Juan de Fuca Plate. *Journal of Geophysical Research*, *91*(B10), 10259. <https://doi.org/10.1029/JB091iB10p10259>
- Wilson, D. S. (2002). *The Juan de Fuca plate and slab: Isochron structure and Cenozoic plate motions. Earthquake.*
- Xue, M., & Allen, R. M. (2010). Mantle structure beneath the western United States and its implications for convection processes. *Journal of Geophysical Research: Solid Earth*, *115*(7), B07303. <https://doi.org/10.1029/2008JB006079>
- Zhao, D. (2007). Seismic images under 60 hotspots: Search for mantle plumes. *Gondwana Research*, *12*(4), 335–355. <https://doi.org/10.1016/j.gr.2007.03.001>

Chapter IV

- Aalto, K. R. (2006). The Klamath peneplain : A review of J . S . Diller ’ s classic erosion surface. *Geological Society of America Special Paper.* [https://doi.org/10.1130/2006.2410\(22\)](https://doi.org/10.1130/2006.2410(22)).
- Amante, C., & Eakins, B. W. (2009). ETOPO1 1 arc-minute global relief model: Procedures, data sources and analysis. *NOAA Tech. Mem. NESDIS, NGDC-24*, 1–19. <https://doi.org/10.1594/PANGAEA.769615>
- Ando, M. (1975). Source mechanisms and tectonic significance of historical earthquakes along the nankai trough, Japan. *Tectonophysics*, *27*(2), 119–140. [https://doi.org/10.1016/0040-1951\(75\)90102-X](https://doi.org/10.1016/0040-1951(75)90102-X)
- Balco, G., Finnegan, N., Gendaszek, A., Stone, J. O. H., & Thompson, A. (2013). Erosional response to northward-propagating crustal thickening in the coastal ranges of the U.S. pacific northwest. *American Journal of Science*, *313*(8), 790–806. <https://doi.org/10.2475/11.2013.01>
- Bassett, D., & Watts, A. B. (2015). Gravity anomalies, crustal structure, and seismicity at subduction zones: 2. Interrelationships between fore-arc structure and seismogenic behavior. *Geochemistry, Geophysics, Geosystems*, *16*(5), 1541–1576. <https://doi.org/10.1002/2014GC005685>
- Betts, P. G., Mason, W. G., & Moresi, L. (2012). The influence of a mantle plume head on the dynamics of a retreating subduction zone. *Geology*, *40*(8), 739–742. <https://doi.org/10.1130/G32909.1>

- Bierman, P., Clapp, E., Nichols, K., Gillespie, A., & Caffee, M. W. (2001). Using Cosmogenic Nuclide Measurements In Sediments To Understand Background Rates Of Erosion And Sediment Transport. In *Landscape Erosion and Evolution Modeling* (pp. 89–115). Boston, MA: Springer US. https://doi.org/10.1007/978-1-4615-0575-4_5
- Bletery, Q., Thomas, A. M., Rempel, A. W., Karlstrom, L., Sladen, A., & De Barros, L. (2016). Mega-earthquakes rupture flat megathrusts. *Science*, *354*(6315), 1027–1031. <https://doi.org/10.1126/science.aag0482>
- Bodmer, M., Toomey, D. R., Hooft, E. E., Nábelek, J., & Braunmiller, J. (2015). Seismic anisotropy beneath the Juan de Fuca plate system: Evidence for heterogeneous mantle flow. *Geology*, *43*(12), 1095–1098. <https://doi.org/10.1130/G37181.1>
- Bodmer, M., Toomey, D. R., Hooft, E. E. E., & Schmandt, B. (2018). Buoyant Asthenosphere Beneath Cascadia Influences Megathrust Segmentation. *Geophysical Research Letters*, *45*(14), 6954–6962. <https://doi.org/10.1029/2018GL078700>
- Bostock, M. G., Christensen, N. I., & Peacock, S. M. (2019). Seismicity in Cascadia. *Lithos*, *332–333*, 55–66. <https://doi.org/10.1016/j.lithos.2019.02.019>
- Brandon, M. T., & Calderwood, A. R. (1990). High-pressure metamorphism and uplift of the Olympic subduction complex. *Geology*, *18*(12), 1252–1255. [https://doi.org/10.1130/0091-7613\(1990\)018<1252:HPMAUO>2.3.CO;2](https://doi.org/10.1130/0091-7613(1990)018<1252:HPMAUO>2.3.CO;2)
- Brandon, M. T., Roden-Tice, M. K., & Carver, J. I. (1998). Late Cenozoic exhumation of the Cascadia accretionary wedge in the Olympic Mountains, northwest Washington State. *Bulletin of the Geological Society of America*, *110*(8), 985–1009. [https://doi.org/10.1130/0016-7606\(1998\)110<0985:LCEOTC>2.3.CO;2](https://doi.org/10.1130/0016-7606(1998)110<0985:LCEOTC>2.3.CO;2)
- Brocher, T. M. (2005). Empirical relations between elastic wavespeeds and density in the Earth's crust. *Bulletin of the Seismological Society of America*, *95*(6), 2081–2092. <https://doi.org/10.1785/0120050077>
- Brudzinski, M. R., & Allen, R. M. (2007). Segmentation in episodic tremor and slip all along Cascadia. *Geology*, *35*(10), 907. <https://doi.org/10.1130/G23740A.1>
- Burgette, R. J., Weldon, R. J., & Schmidt, D. A. (2009). Interseismic uplift rates for western Oregon and along-strike variation in locking on the Cascadia subduction zone. *Journal of Geophysical Research: Solid Earth*, *114*(1). <https://doi.org/10.1029/2008JB005679>
- Cattin, R., Lyon-Caen, H., & Chéry, J. (1997). Quantification of interplate coupling in subduction zones and forearc topography. *Geophysical Research Letters*, *24*(13), 1563–1566. <https://doi.org/http://dx.doi.org/10.1029/97GL01550>
- Christensen, N. I., & Mooney, W. D. (1995). Seismic velocity structure and composition of the continental crust: A global view. *Journal of Geophysical Research: Solid Earth*, *100*(B6), 9761–9788. <https://doi.org/10.1029/95JB00259>

- Cloos, M. (1992). Thrust-type subduction-zone earthquakes and seamount asperities: A physical model for seismic rupture. *Geology*, 20(7), 601. [https://doi.org/10.1130/0091-7613\(1992\)020<0601:TTSZEA>2.3.CO;2](https://doi.org/10.1130/0091-7613(1992)020<0601:TTSZEA>2.3.CO;2)
- Dahlen, F. A. (1990). Fold-and-Thrust Belts and Accretionary Wedges. *Annual Reviews in Earth and Planetary Sciences*, 18, 55–99. <https://doi.org/10.1146/annurev.ea.18.050190.000415>
- Delph, J. R., Levander, A., & Niu, F. (2018). Fluid Controls on the Heterogeneous Seismic Characteristics of the Cascadia Margin. *Geophysical Research Letters*, 45(20), 11,021–11,029. <https://doi.org/10.1029/2018GL079518>
- Diller, J. S. (1902). *Topographic development of the Klamath Mountains*. <https://doi.org/10.3133/b196>
- Ferrier, K. L., Kirchner, J. W., & Finkel, R. C. (2005). Erosion rates over millennial and decadal timescales at Caspar Creek and Redwood Creek, Northern California Coast Ranges. *Earth Surface Processes and Landforms*, 30(8), 1025–1038. <https://doi.org/10.1002/esp.1260>
- Fountain, A. G., Glenn, B., & Basagic, H. J. (2017). The Geography of Glaciers and Perennial Snowfields in the American West. *Arctic, Antarctic, and Alpine Research*, 49(3), 391–410. <https://doi.org/10.1657/aaar0017-003>
- Fuller, T. K., Perg, L. A., Willenbring, J. K., & Lepper, K. (2009). Field evidence for climate-driven changes in sediment supply leading to strath terrace formation. *Geology*, 37(5), 467–470. <https://doi.org/10.1130/G25487A.1>
- Gilbert, H. (2012). Crustal structure and signatures of recent tectonism as influenced by ancient terranes in the western United States. *Geosphere*, 8(1), 141. <https://doi.org/10.1130/GES00720.1>
- Goldfinger, C., Nelson, C. H., Morey, A. E., Joel E., J., Patton, J., Karabanov, E., et al. (2012). Turbidite Event History — Methods and Implications for Holocene Paleoseismicity of the Cascadia Subduction Zone. *U.S. Geological Survey Professional Paper*, 1661.
- Heller, P. L., & Ryberg, P. T. (1983). Sedimentary record of subduction of forearc transition in the rotated Eocene basin of western Oregon (USA). *Geology*. [https://doi.org/10.1130/0091-7613\(1983\)11<380:SROSTF>2.0.CO;2](https://doi.org/10.1130/0091-7613(1983)11<380:SROSTF>2.0.CO;2)
- Huybers, P., & Langmuir, C. (2009). Feedback between deglaciation, volcanism, and atmospheric CO₂. *Earth and Planetary Science Letters*, 286(3–4), 479–491. <https://doi.org/10.1016/j.epsl.2009.07.014>
- Hyndman, R. D., & Wang, K. (1995). The rupture zone of Cascadia great earthquakes from current deformation and the thermal regime. *Journal of Geophysical Research: Solid Earth*, 100(B11), 22133–22154. <https://doi.org/10.1029/95JB01970>

- Kelsey, H. M., Engebretson, D. C., Mitchell, C. E., & Ticknor, R. L. (1994). Topographic form of the Coast Ranges of the Cascadia Margin in relation to coastal uplift rates and plate subduction. *Journal of Geophysical Research: Solid Earth*. <https://doi.org/10.1029/93JB03236>
- Kelsey, H. M., Ticknor, R. L., Bockheim, J. G., & Mitchell, C. E. (1996). Quaternary upper plate deformation in coastal Oregon. *Bulletin of the Geological Society of America*. [https://doi.org/10.1130/0016-7606\(1996\)108<0843:QUPDIC>2.3.CO;2](https://doi.org/10.1130/0016-7606(1996)108<0843:QUPDIC>2.3.CO;2)
- Kopp, H. (2013). Invited review paper: The control of subduction zone structural complexity and geometry on margin segmentation and seismicity. *Tectonophysics*, 589, 1–16. <https://doi.org/10.1016/j.tecto.2012.12.037>
- Leonard, L. J., Currie, C. A., Mazzotti, S., & Hyndman, R. D. (2010). Rupture area and displacement of past Cascadia great earthquakes from coastal coseismic subsidence. *Bulletin of the Geological Society of America*, 122(11–12), 2079–2096. <https://doi.org/10.1130/B30108.1>
- Li, S., Wang, K., Wang, Y., Jiang, Y., & Dosso, S. E. (2018). Geodetically Inferred Locking State of the Cascadia Megathrust Based on a Viscoelastic Earth Model. *Journal of Geophysical Research: Solid Earth*, 123(9), 8056–8072. <https://doi.org/10.1029/2018JB015620>
- Littel, G. F., Thomas, A. M., & Baltay, A. S. (2018). Using Tectonic Tremor to Constrain Seismic Wave Attenuation in Cascadia. *Geophysical Research Letters*, 45(18), 9579–9587. <https://doi.org/10.1029/2018GL079344>
- Livermore, L. (2001). Stochastic Processes of Soil Production and Transport: Erosion Rates, Topographic Variation and Cosmogenic Nuclides in the Oregon Coast Range, 552, 1–22. Retrieved from <file:///Users/paulrichardson/Dropbox/Library.papers3/Files/87/87F40A14-1868-4548-8A39-B6FF386AB9CB.pdf%0Apapers3://publication/uuid/80FDFED5-0877-466D-8E16-A75F6A193E25>
- Marshall, J. A., Roering, J. J., Gavin, D. G., & Granger, D. E. (2017). Late quaternary climatic controls on erosion rates and geomorphic processes in western Oregon, USA. *Bulletin of the Geological Society of America*, 129(5–6), 715–731. <https://doi.org/10.1130/B31509.1>
- McCrorry, P. A., Blair, J. L., Waldhauser, F., & Oppenheimer, D. H. (2012). Juan de Fuca slab geometry and its relation to Wadati-Benioff zone seismicity. *Journal of Geophysical Research: Solid Earth*, 117(9), 1–23. <https://doi.org/10.1029/2012JB009407>
- McNeill, L. C., Goldfinger, C., Kulm, L. V.D., & Yeats, R. S. (2000). Tectonics of the Neogene Cascadia forearc basin: Investigations of a deformed late Miocene unconformity. *Bulletin of the Geological Society of America*, 112(8), 1209–1224. [https://doi.org/10.1130/0016-7606\(2000\)112<1209:TOTNCF>2.0.CO;2](https://doi.org/10.1130/0016-7606(2000)112<1209:TOTNCF>2.0.CO;2)

- Mortimer, N., & Coleman, R. G. (1985). A Neogene structural dome in the Klamath Mountains, California and Oregon. *Geology*, *13*(4), 253–256.
[https://doi.org/10.1130/0091-7613\(1985\)13<253:ANSDIT>2.0.CO;2](https://doi.org/10.1130/0091-7613(1985)13<253:ANSDIT>2.0.CO;2)
- Nishikawa, T., & Ide, S. (2014). Earthquake size distribution in subduction zones linked to slab buoyancy. *Nature Geoscience*, *7*(12), 904–908.
<https://doi.org/10.1038/ngeo2279>
- Pazzaglia, F. J., & Brandon, M. T. (2001). A fluvial record of long-term steady-state uplift and erosion across the Cascadia forearc high, western Washington State. *American Journal of Science*, *301*(4–5), 385–431. <https://doi.org/10.2475/ajs.301.4-5.385>
- Penserini, B. D., Roering, J. J., & Streig, A. (2017). A morphologic proxy for debris flow erosion with application to the earthquake deformation cycle, Cascadia Subduction Zone, USA. *Geomorphology*, *282*(January 2017), 150–161.
<https://doi.org/10.1016/j.geomorph.2017.01.018>
- Piotraschke, R., Cashman, S. M., Furlong, K. P., Kamp, P. J. J., Danišik, M., & Xu, G. (2015). Unroofing the Klamaths—Blame it on Siletzia? *Lithosphere*, *7*(4), 427–440.
<https://doi.org/10.1130/L418.1>
- Ramírez-Herrera, M. T., Gaidzik, K., Forman, S., Kostoglodov, V., Bürgmann, R., & Johnson, C. W. (2018). Relating the long-term and short-term vertical deformation across a transect of the forearc in the central Mexican subduction zone. *Geosphere*, *14*(2), 419–439. <https://doi.org/10.1130/GES01446.1>
- Riddihough, R. (1984). Recent movements of the Juan de Fuca plate system. *Journal of Geophysical Research: Solid Earth*, *89*(B8), 6980–6994.
<https://doi.org/10.1029/JB089iB08p06980>
- Roering, J. J., Perron, J. T., & Kirchner, J. W. (2007). Functional relationships between denudation and hillslope form and relief. *Earth and Planetary Science Letters*, *264*(1–2), 245–258. <https://doi.org/10.1016/j.epsl.2007.09.035>
- Roering, J. J., Mackey, B. H., Handwerker, A. L., Booth, A. M., Schmidt, D. A., Bennett, G. L., & Cerovski-Darriau, C. (2015). Beyond the angle of repose: A review and synthesis of landslide processes in response to rapid uplift, Eel River, Northern California. *Geomorphology*, *236*, 109–131.
<https://doi.org/10.1016/j.geomorph.2015.02.013>
- Royden, L. H., & Husson, L. (2009). Subduction with Variations in Slab Buoyancy: Models and Application to the Banda and Apennine Systems. In *Subduction Zone Geodynamics* (pp. 35–45). <https://doi.org/10.1007/978-3-540-87974-9>
- Schmalzle, G. M., McCaffrey, R., & Creager, K. C. (2014). Central Cascadia subduction zone creep. *Geochemistry, Geophysics, Geosystems*, *15*(4), 1515–1532.
<https://doi.org/10.1002/2013GC005172>

- Scholz, C. H. (2015). On the stress dependence of the earthquake b-value. *Geophysical Research Letters*, 10964. <https://doi.org/10.1002/2014GL062863>
- Shen, W., Ritzwoller, M. H., & Schulte-Pelkum, V. (2013). A 3-D model of the crust and uppermost mantle beneath the Central and Western US by joint inversion of receiver functions and surface wave dispersion. *Journal of Geophysical Research: Solid Earth*, 118(1), 262–276. <https://doi.org/10.1029/2012JB009602>
- Snoke, A. W., & Barnes, C. G. (2006). The development of tectonic concepts for the Klamath Mountains province, California and Oregon. *SPECIAL PAPERS- GEOLOGICAL SOCIETY OF AMERICA*. [https://doi.org/10.1130/2006.2410\(01\)](https://doi.org/10.1130/2006.2410(01)).
- Spada, M., Tormann, T., Wiemer, S., & Enescu, B. (2013). Generic dependence of the frequency-size distribution of earthquakes on depth and its relation to the strength profile of the crust. *Geophysical Research Letters*, 40(4), 709–714. <https://doi.org/10.1029/2012GL054198>
- Tabor, R. W., & Cady, W. M. (1978). The structure of the Olympic Mountains, Washington—Analysis of a subduction zone. *Geological Survey Professional Paper 1033*.
- Wang, K., & He, J. (1999). Mechanics of low-stress forearcs: Nankai and Cascadia. *Journal of Geophysical Research*, 104(B7), 15191. <https://doi.org/10.1029/1999JB900103>
- Wang, P. L., Engelhart, S. E., Wang, K., Hawkes, A. D., Horton, B. P., Nelson, A. R., & Witter, R. C. (2013). Heterogeneous rupture in the great Cascadia earthquake of 1700 inferred from coastal subsidence estimates. *Journal of Geophysical Research: Solid Earth*, 118(5), 2460–2473. <https://doi.org/10.1002/jgrb.50101>
- Wells, R., Bukry, D., Friedman, R., Pyle, D., Duncan, R., Haeussler, P., & Wooden, J. (2014). Geologic history of Siletzia, a large igneous province in the Oregon and Washington Coast Range: Correlation to the geomagnetic polarity time scale and implications for a long-lived Yellowstone hotspot. *Geosphere*, 10(4), 692–719. <https://doi.org/10.1130/GES01018.1>
- Wells, R. E., Blakely, R. J., Wech, A. G., McCrory, P. A., & Michael, A. (2017). Cascadia subduction tremor muted by crustal faults. *Geology*, 45(6), 515–518. <https://doi.org/10.1130/G38835.1>
- Wilson, D. S. (2002). *The Juan de Fuca plate and slab: Isochron structure and Cenozoic plate motions. Earthquake*.

Chapter V

- Atwater, T. (1970). Implications of plate tectonics for the cenozoic tectonic evolution of western north america. *Bulletin of the Geological Society of America*.
[https://doi.org/10.1130/0016-7606\(1970\)81\[3513:IOPTFT\]2.0.CO;2](https://doi.org/10.1130/0016-7606(1970)81[3513:IOPTFT]2.0.CO;2)
- Atwater, T., & Stock, J. (1998). Pacific-north america plate tectonics of the neogene southwestern united states: An update. *International Geology Review*.
<https://doi.org/10.1080/00206819809465216>
- Audet, P., Bostock, M. G., Christensen, N. I., & Peacock, S. M. (2009). Seismic evidence for overpressured subducted oceanic crust and megathrust fault sealing. *Nature*, 457(7225), 76–78. <https://doi.org/10.1038/nature07650>
- Beaudoin, B. C., Hole, J. A., Klemperer, S. L., & Tréhu, A. M. (1998). Location of the southern edge of the Gorda slab and evidence for an adjacent asthenospheric window: Results from seismic profiling and gravity. *Journal of Geophysical Research: Solid Earth*. <https://doi.org/10.1029/98jb02231>
- Becker, T. W. (2012). On recent seismic tomography for the western United States. *Geochemistry, Geophysics, Geosystems*, 13(1), 1–11.
<https://doi.org/10.1029/2011GC003977>
- Bell, S., Ruan, Y., & Forsyth, D. W. (2016). Ridge asymmetry and deep aqueous alteration at the trench observed from Rayleigh wave tomography of the Juan de Fuca plate. *Journal of Geophysical Research: Solid Earth*, 121(10), 7298–7321.
<https://doi.org/10.1002/2016JB012990>
- Bezada, M. J., Humphreys, E. D., Toomey, D. R., Harnafi, M., Dávila, J. M., & Gallart, J. (2013). Evidence for slab rollback in westernmost Mediterranean from improved upper mantle imaging. *Earth and Planetary Science Letters*, 368(Complete), 51–60.
<https://doi.org/10.1016/j.epsl.2013.02.024>
- Bodmer, M., Toomey, D. R., Hooft, E. E., Nábelek, J., & Braunmiller, J. (2015). Seismic anisotropy beneath the Juan de Fuca plate system: Evidence for heterogeneous mantle flow. *Geology*, 43(12). <https://doi.org/10.1130/G37181.1>
- Bodmer, Miles, Toomey, D. R., Hooft, E. E. E., & Schmandt, B. (2018). Buoyant Asthenosphere Beneath Cascadia Influences Megathrust Segmentation. *Geophysical Research Letters*, 45(14), 6954–6962. <https://doi.org/10.1029/2018GL078700>
- Brocher, T. M. (2005). Empirical Relations between Elastic Wavespeeds and Density in the Earth's Crust. *Bulletin of the Seismological Society of America*, 95(6), 2081–2092. <https://doi.org/10.1785/0120050077>

- Brudzinski, M. R., & Allen, R. M. (2007). Segmentation in episodic tremor and slip all along Cascadia. *Geology*, *35*(10), 907. <https://doi.org/10.1130/G23740A.1>
- Burgette, R. J., Weldon, R. J., & Schmidt, D. A. (2009). Interseismic uplift rates for western Oregon and along-strike variation in locking on the Cascadia subduction zone. *Journal of Geophysical Research: Solid Earth*, *114*(1). <https://doi.org/10.1029/2008JB005679>
- Byrnes, J. S., Toomey, D. R., Hooft, E. E. E., Nábělek, J., & Braunmiller, J. (2017). Mantle dynamics beneath the discrete and diffuse plate boundaries of the Juan de Fuca plate: Results from Cascadia Initiative body wave tomography. *Geochemistry, Geophysics, Geosystems*, *18*(8), 2906–2929. <https://doi.org/10.1002/2017GC006980>
- Camp, V. E. (2015). Origin of Columbia River Basalt: Passive rise of shallow mantle, or active upwelling of a deep-mantle plume? [https://doi.org/10.1130/2013.2497\(07\)](https://doi.org/10.1130/2013.2497(07))
- Chaytor, J. D., Goldfinger, C., Dziak, R. P., & Fox, C. G. (2004). Active deformation of the Gorda plate: Constraining deformation models with new geophysical data. *Geology*, *32*(4), 353–356. <https://doi.org/10.1130/G20178.2>
- Chen, C., Zhao, D., & Wu, S. (2015). Tomographic imaging of the Cascadia subduction zone: Constraints on the Juan de Fuca slab. *Tectonophysics*, *647*, 73–88. <https://doi.org/10.1016/j.tecto.2015.02.012>
- Cloos, M. (1992). Thrust-type subduction-zone earthquakes and seamount asperities: A physical model for seismic rupture. *Geology*, *20*(7), 601. [https://doi.org/10.1130/0091-7613\(1992\)020<0601:TTSZEA>2.3.CO;2](https://doi.org/10.1130/0091-7613(1992)020<0601:TTSZEA>2.3.CO;2)
- Crotwell, H. P., Owens, T. J., & Ritsema, J. (2011). The TauP Toolkit: Flexible Seismic Travel-time and Ray-path Utilities. *Seismological Research Letters*. <https://doi.org/10.1785/gssrl.70.2.154>
- Dahlen, F. A., Hung, S.-H., & Nolet, G. (2000). Fréchet kernels for finite-frequency traveltimes-I. Theory. *Geophysical Journal International*, *141*(1), 157–174. <https://doi.org/10.1046/j.1365-246X.2000.00070.x>
- DeCelles, P. G. (2004). Late Jurassic to Eocene evolution of the Cordilleran thrust belt and foreland basin system, western U.S.A. *American Journal of Science*. <https://doi.org/10.2475/ajs.304.2.105>
- Delph, J. R., Levander, A., & Niu, F. (2018). Fluid Controls on the Heterogeneous Seismic Characteristics of the Cascadia Margin. *Geophysical Research Letters*, *45*(20), 11,021–11,029. <https://doi.org/10.1029/2018GL079518>
- Dijkstra, E. W. (1959). A note on two problems in connexion with graphs. *Numerische Mathematik*. <https://doi.org/10.1007/BF01386390>

- Divins; D.L. (2003). Total Sediment Thickness of the World's Oceans & Marginal Seas. *NOAA National Geophysical Data Center, Boulder, CO.*
- Dziewonski, A. M., & Anderson, D. L. (1983). Travel times and station corrections for P waves at teleseismic distances. *Journal of Geophysical Research*.
<https://doi.org/10.1029/JB088iB04p03295>
- Furlong, K. P., & Schwartz, S. Y. (2004). INFLUENCE OF THE MENDOCINO TRIPLE JUNCTION ON THE TECTONICS OF COASTAL CALIFORNIA. *Annual Review of Earth and Planetary Sciences*.
<https://doi.org/10.1146/annurev.earth.32.101802.120252>
- Gao, H. (2018). Three-dimensional variations of the slab geometry correlate with earthquake distributions at the Cascadia subduction system. *Nature Communications*, (2018), 1–8. <https://doi.org/10.1038/s41467-018-03655-5>
- Hammond, W. C., & Toomey, D. R. (2003). Seismic velocity anisotropy and heterogeneity beneath the Mantle Electromagnetic and Tomography Experiment (MELT) region of the East Pacific Rise from analysis of P and S body waves. *J. Geophys. Res.*, 108(B4), 2176. <https://doi.org/10.1029/2002jb001789>
- Haney, M. M., Power, J., West, M., & Michaels, P. (2012). Causal instrument corrections for short-period and broadband seismometers. *Seismological Research Letters*, 83(5), 834–845. <https://doi.org/10.1785/0220120031>
- Hawley, W. B., Allen, R. M., & Richards, M. A. (2016). Tomography reveals buoyant asthenosphere accumulating beneath the Juan de Fuca plate. *Science*, 353(6306), 1406–1408. <https://doi.org/10.1126/science.aad8104>
- Hooper, P. R., Binger, G. B., & Lees, K. R. (2002). Ages of the Steens and Columbia River flood basalts and their relationship to extension-related calc-alkalic volcanism in eastern Oregon. *Bulletin of the Geological Society of America*.
[https://doi.org/10.1130/0016-7606\(2002\)114<0043:AOTSAC>2.0.CO;2](https://doi.org/10.1130/0016-7606(2002)114<0043:AOTSAC>2.0.CO;2)
- IRIS Transportable Array (2003): USArray Transportable Array. International Federation of Digital Seismograph Networks. Dataset/Seismic Network. 10.7914/SN/TA
- Jackson, D. D. (1979). The use of a priori data to resolve non-uniqueness in linear inversion. *Geophysical Journal International*, 57(1), 137–157.
<https://doi.org/10.1111/j.1365-246X.1979.tb03777.x>
- Kelsey, H. M., Engebretson, D. C., Mitchell, C. E., & Ticknor, R. L. (1994). Topographic form of the Coast Ranges of the Cascadia Margin in relation to coastal uplift rates and plate subduction. *Journal of Geophysical Research: Solid Earth*.
<https://doi.org/10.1029/93JB03236>

- Kennett, B. L. N., Engdahl, E. R., & Buland, R. (1995). Constraints on seismic velocities in the Earth from traveltimes. *Geophysical Journal International*, 122(1), 108–124. <https://doi.org/10.1111/j.1365-246X.1995.tb03540.x>
- Laske, G., Masters, G., Ma, Z., Pasyanos, M. E., & Livermore, L. (2013). Update on CRUST1.0: A 1-degree Global Model of Earth's Crust. *Geophys. Res. Abstracts*.
- Leonard, L. J., Currie, C. A., Mazzotti, S., & Hyndman, R. D. (2010). Rupture area and displacement of past Cascadia great earthquakes from coastal coseismic subsidence. *Bulletin of the Geological Society of America*, 122(11–12), 2079–2096. <https://doi.org/10.1130/B30108.1>
- Lin, F. C., & Schmandt, B. (2014). Upper crustal azimuthal anisotropy across the contiguous U.S. determined by Rayleigh wave ellipticity. *Geophysical Research Letters*, 41(23), 8301–8307. <https://doi.org/10.1002/2014GL062362>
- Littel, G. F., Thomas, A. M., & Baltay, A. S. (2018). Using Tectonic Tremor to Constrain Seismic Wave Attenuation in Cascadia. *Geophysical Research Letters*. <https://doi.org/10.1029/2018GL079344>
- Long, M. D. (2016). The Cascadia Paradox: Mantle flow and slab fragmentation in the Cascadia subduction system. *Journal of Geodynamics*. <https://doi.org/10.1016/j.jog.2016.09.006>
- McCrary, P. A., Blair, J. L., Waldhauser, F., & Oppenheimer, D. H. (2012). Juan de Fuca slab geometry and its relation to Wadati-Benioff zone seismicity. *Journal of Geophysical Research: Solid Earth*, 117(9), 1–23. <https://doi.org/10.1029/2012JB009407>
- Menke, W. (1985). *Geophysical Data Analysis: Discrete Inverse Theory*. *Geophysical Data Analysis: Discrete Inverse Theory*. <https://doi.org/10.1016/C2011-0-69765-0>
- Moser, T. J. (1991). Shortest path calculation of seismic rays. *Geophysics*, 56(1), 59–67. <https://doi.org/10.1190/1.1442958>
- Obrebski, M., Allen, R. M., Xue, M., & Hung, S. H. (2010). Slab-plume interaction beneath the Pacific Northwest. *Geophysical Research Letters*, 37(14), 1–6. <https://doi.org/10.1029/2010GL043489>
- Parsons, T., Blakely, R. J., Brocher, T. M., Christensen, N. I., Fisher, M. A., Flueh, E., et al. (2005). Crustal Structure of the Cascadia Fore Arc of Washington. *U.S Geological Survey Professional Paper 1661-D, Earthquake*, 36. Retrieved from <http://govreports.library.gatech.edu/handle/123456789/599>
- Pierce, K. L., & Morgan, L. A. (1992). The track of the Yellowstone hot spot: Volcanism, faulting, and uplift. *Regional Geology of Eastern Idaho and Western Wyoming: Geological Society of America Memoir*. <https://doi.org/10.1130/MEM179-p1>

- Portner, D. E., Beck, S., Zandt, G., & Scire, A. (2017). The nature of subslab slow velocity anomalies beneath South America. *Geophysical Research Letters*, *44*(10), 4747–4755. <https://doi.org/10.1002/2017GL073106>
- Riddihough, R. (1984). Recent movements of the Juan de Fuca plate system. *Journal of Geophysical Research: Solid Earth*, *89*(B8), 6980–6994. <https://doi.org/10.1029/JB089iB08p06980>
- Riddihough, R. P. (1980). Gorda plate motions from magnetic anomaly analysis. *Earth and Planetary Science Letters*, *51*(1), 163–170. [https://doi.org/10.1016/0012-821X\(80\)90263-0](https://doi.org/10.1016/0012-821X(80)90263-0)
- Robertson, G. S., & Woodhouse, J. H. (1997). Comparison of P and S station corrections and their relationship to upper mantle structure. *Journal of Geophysical Research: Solid Earth*. <https://doi.org/10.1029/97jb02348>
- Roth, J. B., Fouch, M. J., James, D. E., & Carlson, R. W. (2008). Three-dimensional seismic velocity structure of the northwestern United States. *Geophysical Research Letters*, *35*(15), L15304. <https://doi.org/10.1029/2008GL034669>
- Ruff, L. J. (1989). Do trench sediments affect great earthquake occurrence in subduction zones? *Pure and Applied Geophysics PAGEOPH*, *129*(1–2), 263–282. <https://doi.org/10.1007/BF00874629>
- Schmalzle, G. M., McCaffrey, R., & Creager, K. C. (2014). Central Cascadia subduction zone creep. *Geochemistry, Geophysics, Geosystems*, *15*(4), 1515–1532. <https://doi.org/10.1002/2013GC005172>
- Schmandt, B., & Humphreys, E. (2010a). Complex subduction and small-scale convection revealed by body-wave tomography of the western United States upper mantle. *Earth and Planetary Science Letters*, *297*(3–4), 435–445. <https://doi.org/10.1016/j.epsl.2010.06.047>
- Schmandt, B., & Humphreys, E. (2010b). Seismic heterogeneity and small-scale convection in the southern California upper mantle. *Geochemistry, Geophysics, Geosystems*, *11*(5), 1–19. <https://doi.org/10.1029/2010GC003042>
- Schmandt, B., & Humphreys, E. (2011). Seismically imaged relict slab from the 55 Ma Siletzia accretion to the northwest United States. *Geology*, *39*(2), 175–178. <https://doi.org/10.1130/G31558.1>
- Schmandt, B., & Lin, F. (2014). P and S wave tomography of the mantle beneath the United States. *Geophysical Research Letters*, *41*(18), 6342–6349. <https://doi.org/10.1002/2014GL061231>
- Schmandt, B., Dueker, K., Humphreys, E., & Hansen, S. (2012). Hot mantle upwelling across the 660 beneath Yellowstone. *Earth and Planetary Science Letters*, *331–332*, 224–236. <https://doi.org/10.1016/j.epsl.2012.03.025>

- Shaw, P. R., & Orcutt, J. A. (1985). Waveform inversion of seismic refraction data and applications to young Pacific crust. *Geophysical Journal of the Royal Astronomical Society*. <https://doi.org/10.1111/j.1365-246X.1985.tb05143.x>
- Sigloch, K., McQuarrie, N., & Nolet, G. (2008). Two-stage subduction history under North America inferred from multiple-frequency tomography. *Nature Geoscience*, *1*(7), 458–462. <https://doi.org/10.1038/ngeo231>
- Small, C., & Danyushevsky, L. V. (2003). Plate-kinematic explanation for mid-oceanic-ridge depth discontinuities. *Geology*. [https://doi.org/10.1130/0091-7613\(2003\)031<0399:PEFMDD>2.0.CO;2](https://doi.org/10.1130/0091-7613(2003)031<0399:PEFMDD>2.0.CO;2)
- Stern, R. J. (2002). Subduction zones. *Encyclopedia of Earth Sciences Series*. https://doi.org/10.1007/978-90-481-8702-7_149
- Stock, J. M., & Lee, J. (1994). Leave a Geological Record? *America*, *13*(6), 1472–1487.
- Tarantola, A., & Valette, B. (1982). Generalized nonlinear inverse problems solved using the least squares criterion. *Reviews of Geophysics*, *20*(2), 219. <https://doi.org/10.1029/RG020i002p00219>
- Toomey, D., Allen, R., Barclay, A., Bell, S., Bromirski, P., Carlson, R., et al. (2014). The Cascadia Initiative: A sea change in seismological studies of subduction zones. *Oceanography*, *27*(2), 138–150. <https://doi.org/10.5670/oceanog.2014.49>
- Toomey, D. R., Solomon, S. C., & Purdy, G. M. (1994). Tomographic imaging of the shallow crustal structure of the East Pacific Rise at 9°30'N. *Journal of Geophysical Research*, *99*(B12), 24135–24157. <https://doi.org/10.1029/94JB01942>
- Trehu, a M., Asudeh, I., Brocher, T. M., Luetgert, J. H., Mooney, W. D., Nabelek, J. L., & Nakamura, Y. (1994). Crustal architecture of the cascadia forearc. *Science*, *266*(5183), 237–243. <https://doi.org/10.1126/science.266.5183.237>
- VanDecar, J. C., & Crosson, R. S. (1990). Determination of teleseismic relative phase arrival times using multi-channel cross-correlation and least squares. *Bulletin of the Seismological Society of America*, *80*(1), 150–169. Retrieved from <http://www.bssaonline.org/content/80/1/150.short>
- Wada, I., Mazzotti, S., & Wang, K. (2010). Intraslab stresses in the cascadia subduction zone from inversion of earthquake focal mechanisms. *Bulletin of the Seismological Society of America*. <https://doi.org/10.1785/0120090349>
- Waldhauser, F., Lippitsch, R., Kissling, E., & Ansorge, J. (2002). High-resolution teleseismic tomography of upper-mantle structure using an a priori three-dimensional crustal model. *Geophysical Journal International*, *150*(2), 403–414. <https://doi.org/10.1046/j.1365-246X.2002.01690.x>

- Wells, R. E., Engebretson, D. C., Snively, P. D., & Coe, R. S. (1984). Cenozoic plate motions and the volcano-tectonic evolution of western Oregon and Washington. *Tectonics*. <https://doi.org/10.1029/TC003i002p00275>
- Wells, Ray E, Blakely, R. J., Wech, A. G., McCrory, P. A., & Michael, A. (2017). Cascadia subduction tremor muted by crustal faults. *Geology*, *45*(6), 515–518. <https://doi.org/10.1130/G38835.1>
- Wilson, D. S. (1989). Deformation of the so-called Gorda plate. *Journal of Geophysical Research*. <https://doi.org/10.1029/JB094iB03p03065>
- Wilson, Douglas S. (1986). A kinematic model for the Gorda Deformation Zone as a diffuse southern boundary of the Juan de Fuca Plate. *Journal of Geophysical Research*, *91*(B10), 10259. <https://doi.org/10.1029/JB091iB10p10259>